This is to certify that the

dissertation entitled

USE OF ND:YAG LASER FOR PROCESSING HIGH TEMPERATURE SUPERCONDUCTORS

presented by

Chung-Wen Chen

has been accepted towards fulfillment
of the requirements for

Ph. D. degree in Materials Science

Kali Mukherjee
Major professor

Date 11/20/93

USE OF ND:YAG LASER FOR PROCESSING HIGH TEMPERATURE SUPERCONDUCTORS

By

Chung-Wen Chen

A DISSERTATION

Submitted to
Michigan State University
in partial fulfillment of the requirements
for the degree of

DOCTOR OF PHILOSOPHY

Department of Materials Science and Mechanics

1993

ABSTRACT

USE OF ND:YAG LASER FOR PROCESSING HIGH TEMPERATURE SUPERCONDUCTORS

By

Chung-Wen Chen

The problem associated with sluggish kinetics of formation of 2223 high T_c phase in Pb-doped Bi-Sr-Ca-Cu-O system was investigated. A laser calcination process for Pb-doped Bi-Sr-Ca-Cu-O (BSCCO) material was established with the consideration that localized temperature surge, above the melting temperature, might enhance the formation of the 110 K 2223 phase. The total processing time, to obtain a near single high T_c phase, was reduced to half that for conventional processing (about 100 hours). High T_c phase was formed via a different kinetic path in laser calcined sample compared with the conventionally processed sample.

An ion beam assisted millisecond pulsed laser vapor deposition (IBPLD) process was developed to fabricate $YBa_2Cu_3O_x$ (YBCO) high T_c superconductor thin films. Target overheating problem was greatly reduced by using a zigzag scanning pattern of the target with an x-y target manipulator. High energy oxygen ion beam was used to replenish oxygen and to blow vapor species onto the substrate. More than 25 mm diameter, uniform coating of YBCO was successfully deposited. As-deposited films are composed of various compounds of Y_2O_3, BaO and CuO as well as Y_2BaCuO_5. Due to microscopic chemical homogeneity of films, films with majority 1-2-3 phase are formed by just half an hour of post annealing at 850 °C. Silver buffer layer is found to effectively minimize degradation caused by film/substrate reaction of (001)YSZ substrate during post annealing.

A new process combining millisecond pulsed laser deposition (ms-PLD) and vacuum thermal evaporation (VTE) techniques was developed to produce multi-layer Ag doped YBCO/Ag thick film. Flexible multi-layer thick films, with thickness about a few tens to a few hundreds of microns, were made. This process starts with about 5 to 50 μm layer of silver deposited by VTE on a fused silicate substrate at room temperature, then followed by a 5 to 50 μm layer of Ag doped YBCO using ms-PLD. This process is repeated several times to achieve desired multi-layer number and thickness. When the desired thickness is obtained, another layer of silver is thermally deposited above the Ag doped YBCO before the multi-layer composite thick film is peeled from the substrate. Post annealing is followed to recover superconductivity.

To my Parents
and
my wife Lina

ACKNOWLEDGMENTS

I wish to express my sincere gratitude to my advisor, Professor Kalinath Mukherjee, for his valuable guidance and constant support throughout this study. My appreciation is extended to the committee members, Professor Eldon Case, Professor Carl Foiles and Professor K. N. Subramanian, for their helpful comments and suggestions.

Special thanks are due to Dr. P. A. A. Khan for many years of kind advise and assistance. I also would like to thank all faculty and staff in the Department of Materials Science and Mechanics for their helpful support during the years.

Last but not least, I wish to express my sincere gratefulness to my family in Taiwan and my wife Lina for their continuous support and encouragement.

TABLE OF CONTENTS

LIST OF TABLES

LIST OF FIGURES

I. INTRODUCTION

Three most important high-T_C (high critical temperature) oxide superconductor systems are Y-Ba-Cu-O (yttrium-barium cuprates or rare earth-barium cuprates), Bi-(Pb)-Sr-Ca-Cu-O (bismuth-lead-strontium-calcium cuprates), and Tl-Ba-Ca-Cu-O (thallium-barium-calcium cuprates). All of these three systems have complicated crystal structures with copper-oxygen planes, which are believed to be responsible for the superconducting properties of these compounds. Among these cuprates Tl-Ba-Ca-Cu-O system has the highest T_C, about 125 K*[1,2]*, but the potential for industrial application is limited due to severe health problem associated with the toxicity of thallium compounds.

Material processing utilizing high-power lasers, especially high-energy pulsed lasers, have been widely adopted to produce high T_C superconductors. These techniques include:

1. Pulsed laser vapor deposition (PLD) or ablation*[3-23]*
2. Thin film patterning
    (a) by pulsed laser ablation*[24-26]*
    (b) by direct laser writing of precursor films*[27]*
    (c) by laser assisted etching*[28]*
3. Laser calcining of high T_C superconducting powder*[29,30]*
4. Laser re-melting/texturing*[31]*.
5. Laser annealing of superconducting thin films*[32]*.

$Bi_{2-X}Pb_XSr_2Ca_2Cu_3O_Y$ (2223 phase) of the Bi-(Pb)-Sr-Ca-Cu-O (BSCCO) system, with T_C about 110 K, is a good candidate for tape application due to its thin plate shaped grains that facilitate mechanical alignment of the grains to obtain higher critical current density*[33-34]*. However, the BSCCO superconductor system has a number of phases

with different critical temperatures. The three major phases are referred to by their cation ratios as 2201 (T_c below 77 K), 2212 (T_c ~ 85 K), and 2223 (T_c ~110 K)*[35]*.

Since the discovery of superconductivity in this system*[36]*, many efforts have been made to maximize the amount of high T_c-2223 (110 K) phase. A major enhancement in the formation of high T_c-2223 phase was made by doping Bi-Sr-Ca-Cu-O compound with Pb*[37-41]*. However, With Pb doping, about 200 hours of total processing time is required to obtain a single or nearly a single high T_c phase. In this study, a new laser processing technique was developed with an objective to enhance the kinetics of formation of the high T_c phase of a Pb-doped BSCCO superconductor. With laser calcination process, near single-phase high T_c phase samples were obtained in about 100 hours. The onset critical temperature of the laser calcined sample was found to be about 110 K. However, the zero resistance temperature was about 98 K.

The discovery of oxide high temperature superconductors opens numerous opportunities for applications that are previously impossible. At the present time, potential applications of bulk oxide superconductors are very restricted because of their poor mechanical properties and low critical current densities.

Enormous effort has been made to produce thin films with correct stoichiometry, high transition temperature and high critical current density. $YBa_2Cu_3O_x$ (YBCO), with T_c around 95 K, is considered to be the most favorable oxide superconductor for thin film applications, because compared with other systems, it has less complicated chemistry and structure, good phase stability, and high critical current density*[3]*.

Among the techniques adapted to grow high T_c superconductor thin films, pulsed laser vapor deposition is the most widely studied and a most successful one*[3-6,9,10,19]*. The key reasons for the success of the PLD process are its stoichiometry conservation property, and the production of excited high energy vapor species*[42-46]*.

It is well known that high quality YBCO thin films can be obtained by using an excimer laser with a 193, 248, or 308 nm wavelength, nanosecond pulse width and a

few J/cm^2 pulse energy density. However, the deposition rate is very low, typically a few tenth of nm per second. Moreover, the deposited area coverage is very small, only a few millimeters in width, due to the narrow angular distributions of the vapor, as sharp as $\cos^8\theta$ to $\cos^{12}\theta$*[15,16,42]*. On the other hand, high deposition rates up to 100 nm/s*[15]* and a large uniform deposition coverage, due to a broader ($\cos\theta$) angular distribution of the evaporated species can be obtained by using millisecond pulsed lasers. These enhanced deposition rates make millisecond-PLD (ms-PLD) a practical process to produce continuous coating of large substrates.

A detailed study of the ms-PLD process was carried out using a millisecond pulsed neodymium: yttrium aluminum garnet (Nd:YAG) laser with 1064 nm wavelength. Due to several orders of magnitude longer pulse-width compared with excimer lasers, several hundred Joule/cm^2 pulse energy density is required to achieve a peak power density close to Mega Watt/cm^2, which is still much lower than the peak power density achieved by a nanosecond laser pulse at typically a few Joule/cm^2 energy density.

Overheating and severe local melting, which resulted in roughening of the target and thereby misdirecting the vapor plume, are major problems associated with ms-PLD process. This problem is reduced by using a zigzag scanning pattern of the target with an x-y target manipulator. However, for prolonged deposition without frequent re-surfacing, the pulse energy density is restricted to about 60 J/cm^2 that also limits the deposition rate below 10 nm/s*[47]*. Because the ms-PLD process has a relatively high deposition rate and low peak power density, a penning ion gun is used to introduce high energy oxygen ions to the laser induced plume and the growing film to replenish oxygen and to boost the energy of vapor species.

Most practical engineering applications require the superconductors to be fabricated into desired shapes such as thin film, wires or tapes. However, brittle nature of the oxide ceramic superconductors prohibits the use of conventional forming techniques, and monolithic ceramic superconductor wire or tape will not have enough toughness for

normal handling. Both of these problems are expected to be reduced by forming composites of superconductors and some ductile metals. However, compatibility is the major problem in selecting a metal for this purpose*[48,49]*. Silver has been proven not only to be compatible with both YBCO and BSCCO systems, but also to improve superconducting properties of these compounds*[50-53]*. In addition, texture of the superconducting layers is expected due to geometric constraint of layered structure.

Uniform thick films can readily be obtained by vapor deposition techniques. Among these techniques, vacuum thermal evaporation is a simple yet effective way to deposit thick films with simple composition such as pure silver. Oxide superconductors, on the other hand, have a very complicated composition, so special techniques such as the ms-PLD are required to preserve the Stoichiometry of the compound. In order to further enhance the deposition rate, silver doped YBCO was studied as the target material for the ms-PLD process, with the hope that subsurface overheating problem can be significantly reduced by increase density, thermal conductivity, and mechanical strength of the target*[19]*. A new process combining the above two deposition techniques to produce a multi-layer YBCO/silver thick film was developed.

The primary objective of this research is to develop new processes of high T_c superconductors which take advantage of the unique properties of a millisecond pulsed Nd:YAG laser as the energy source.

2. LITERATURE SURVEY

2.1 Superconductors and Theories of Superconductivity*

The electrical resistivities of many materials, including elements, alloys, ceramics, and organic compounds, vanish when a specimen of these materials is cooled below some critical temperature, T_C . This phenomenon, called superconductivity, was first observed in mercury in 1911 by Heike Kammerlingh Onnes*[54]*. Subsequent researches showed that superconductivity is fairly common among non-magnetic metallic elements with the highest T_C about 9.5 K for niobium*[55,56]*. In 1933, Meissner and Ochsenfeilf discovered that a superconductor completely expels magnetic flux lines from its body when it is cooled through the critical temperature under a weak magnetic field. The Meissner effect, or perfect diamagnetism, is another essential property of superconductivity, which cannot be obtained by the characteristic of zero resistivity, or perfect conductor, alone. In a magnetic field, the Meissner effect implies the presence of surface screening current that produces a magnetic field that exactly cancels the external field. Important parameters of superconductors such as magnetic penetration depth, critical field and critical current density are related to the Meissner effect. Among superconducting elements niobium, once again, has the highest critical field H_C about 0.2 T*[55,56]*; however, it is too small for most practical applications such as high-field superconducting magnets envisioned by Onnes in his 1913 Nobel Price lecture.

2.1.1 Two-Fluid Model, London Equation and Non-local Electrodynamics

Following the discovery of Meissner effect, several important phenomenological theories were developed to understand properties of superconductors*[56]*. Among these

* The CGS-Gaussian units are used for formulas in this section.
A complete list of symbol definitions are included in the appendix.

is two-fluid model used by Gorter and Casimer (1934) to obtain a free energy expression that in turn gives expressions for electronic specific heat and fraction of superconducting electron density, $n_s/n = 1 - (T/T_C)^4$. Subsequently, the brothers F. and H. London (1935), based on the two-fluid model, formulated the London equation*[55,56,58]*

$$\nabla \times \mathbf{j} = -\frac{n_s e^2}{mC}\mathbf{B} \quad \text{or} \quad \mathbf{j} = -\frac{n_s e^2}{mC}\mathbf{A}$$

relating the supercurrent density **j** and the magnetic field strength **B** or the magnetic potential field **A**. Combining with Maxwell's equation, the magnetic field and supercurrent density have expressions in the same form*[55,56]*.

$$\nabla^2 \mathbf{B} = \mathbf{B}/\lambda_L^2 \;\; ; \;\; \nabla^2 \mathbf{j} = \mathbf{j}/\lambda_L^2$$

These equations have solutions that decay exponentailly, from the surface into a superconductor bulk, with a characteristic length λ_L called the magnetic penetration depth.

$$\lambda_L^2 \equiv mC^2/4\pi n_s e^2$$

Non-local electrodynamics was applied to explain the strong dependence of the penetration depth on alloying of elemental superconductors by Pippard (1953)*[56]*. It was thought that the local relation between **j** and **A** in the London equation must be generalized to include the effect of field throughout a volume of radius ℓ about the origin, where ℓ is the mean free path of normal state electrons dependent strongly on the alloying. The superconducting wave function should have a characteristic length, the coherence length, which plays a role similar to the electron mean free path in normal metals. The coherence length can be estimated using the Uncertainty Principle assuming that only electrons within about $k_B T_C$ of the Fermi energy (E_F) are responsible for superconductivity. Therefore, the important electrons have a momentum uncertainty

$\Delta P \approx k_B T_C / V_F$, where V_F is the velocity of electrons with the Fermi energy (E_F). A corresponding position uncertainty is $\Delta x \approx \hbar / \Delta P \approx \hbar_F / (k_B T_C)$. Thus, the coherence length can be defined as*[56]*

$$\xi_0 = \alpha \frac{\hbar V_F}{k_B T_c} \quad .$$

2.1.2 Ginzburg-Landau Theory

Ginzburg and Landau (1950) proposed a phenomenological theory of superconducting state in terms of a spatially varied order parameter $\Psi(r)$ which vanishes at a second-order phase transition temperature*[55,56,58]*. The order parameter is hypothesized to be related to local superconducting charge carrier density n_s' by

$$\Psi^*(r)\Psi(r) = |\Psi(r)|^2 = n'_s(r) \quad .$$

Many important characteristics of superconductors can be understood by adopting the particle probability amplitude or the center of mass wave function of the Cooper pairs from the BCS theory as the order parameter. Even with the development of the BCS theory, the Ginzburg-Landau theory is still of the preeminent importance especially for thin films and type II superconductors. This theory is essentially the only way to deal with spatially inhomogeneous systems.

This theory starts by formulating the Ginzburg-Landau free energy density difference between the superconducting state and normal state as*[55,56,58]*

$$F_S - F_N = -\alpha|\Psi|^2 + \frac{1}{2}\beta|\Psi|^4 + \frac{1}{2m'}\left|\left(-i\hbar\nabla - \frac{e'A}{C}\right)\Psi\right|^2 + \frac{H^2}{8\pi} \quad .$$

The first two terms alone represent the free energy density difference in the absence of magnetic field and spatial variation of the order parameter, where α and β are parameters

to be determined. The third term, arising from kinetic momentum $-i\hbar\nabla$ and field momentum -e'A/C, denotes the energy increase due to spatial variation of the order parameter Ψ, where m' and e' are mass and charge of the charge carrier, and **A** is the magnetic potential field defined by $\mathbf{B} = \nabla \times \mathbf{A}$. The $H^2/(8\pi)$ term gives the energy increase due to magnetic flux expulsion, i.e. Meissner effect.

London equation can be derived from the free energy expression. Minimizing the free energy with respect to the potential **A** yields

$$\frac{ie'\hbar}{2m'C}(\Psi^*\nabla\Psi - \Psi\nabla\Psi^*) + \frac{e'^2}{m'C^2}\Psi^*\Psi\mathbf{A} + \frac{1}{4\pi}\nabla\times\mathbf{H} = 0 \quad .$$

which is called the Ginzburg-Landau equation. The first term drops due to the London rigidity, i.e. at ground state the superconducting wave function is essentially unchanged by the application of the magnetic field. Combining with Maxwell's equation, $\mathbf{j} = [C/(4\pi)]\,\nabla \times \mathbf{H}$, yields the London equation

$$\mathbf{j} = -\frac{e'^2}{m'C}|\Psi|^2\mathbf{A} = \frac{e'^2}{m'C}\left(\frac{\alpha}{\beta}\right)\mathbf{A} \quad .$$

A penetration depth similar to the London penetration depth is defined as*[55,56]*

$$\lambda = \left(\frac{m'C^2\beta}{4\pi e'^2\alpha}\right)^{1/2} \quad .$$

Minimizing the free energy with respect to the order parameter Ψ^* yields

$$\left(-\alpha + \beta|\Psi|^2 + \frac{1}{2m'}\left|-i\hbar\nabla - \frac{e'}{C}\mathbf{A}\right|^2\right)\Psi = 0 \quad .$$

This is also called the Ginzburg-Landau equation that resembles a Schrödinger equation for Ψ*[55,56]*. Considering this equation in one-dimension and in the absence of a field, yields

$$-\frac{\hbar^2}{2m'}\frac{d^2}{dx^2}\Psi = \alpha\Psi ,$$

where the nonlinear term $\beta|\Psi|^2$ is omitted for temperatures near T_c because $|\Psi|^2$ is small. This equation has a wave-like solution $\Psi(x) = \Psi_0 \exp(-ix/\xi)$. The coherence length, $\xi \equiv \left[\hbar^2/(2m'\alpha)\right]^{1/2}$, marks the extent of coherence of the superconducting wave function into the normal region*[55,56]*. The dimensionless ratio between the two characteristic lengths λ and ξ, called Ginzburg-Landau parameter, is an important parameter in the theory of superconductivity.

$$\kappa \equiv \frac{\lambda}{\xi} = \frac{m'C}{e'\hbar}\left(\frac{\beta}{2\pi}\right)^{1/2}$$

Similar to the normal state electron mean free path, the coherence length and the penetration depth are very sensitive to purity of the material. As a result, the Ginzburg-Landau parameter κ increases rapidly as the purity of the superconductor decreases*[56]*.

2.1.3 BCS Theory

A comprehensive quantum theory of superconductivity was proposed by Bardeen, Cooper, and Schrieffer in 1957, almost half a century after the discovery of superconductivity*[57,58]*. This Nobel Prize master piece is frequently referred as the BCS theory. Main features of this theory include*[55-58]*:

2.1.3.1 Phonon-Mediated Pairing of Electrons (Cooper Pairs):

Cooper pair forms by indirect electron-phonon-electron interaction of two electrons with opposite spins near the spherical Fermi surface, and wave-vector **k** and **-k**, respectively. When one of the electrons moves through the lattice, the lattice is distorted

by means of a phonon such that the other electron adjusts itself to take advantage of the lattice distortion to lower its energy. The so-called ***weak coupling*** assumption is used in the pairing theory in which the electron-phonon interaction matrix elements U are assumed to be independent of **k** for states within the $E_F \pm \hbar\omega_D$ range, where E_F and $\hbar\omega_D$ are the Fermi energy and Debye energy, respectively. As a result, energy of the paired electrons is lower than $2E_F$ even if the wave-vector **k** and **-k** are slightly outside the ***Fermi sphere***. The binding energy of a Cooper pair may be written as*[55]*

$$\Delta = \frac{2\hbar\omega_D}{\exp\left(\frac{1}{N_F U}\right)^{-1}},$$

where N_F is the density of normal-state electrons at the Fermi energy. This pairing theory indicates instability of the electron system and leads to the construction of the BCS ground state.

2.1.3.2 BCS Ground State and Energy Gap Near the Fermi Energy

The crucial feature of the BCS ground state is the pair occupancy of the one-particle orbits (states) because the Cooper pair is formed from a pair of electrons with opposite spins and wave-vector **k** and **-k**, i.e. time reversed momentum states. Unlike electrons with half spin, a fermion obeying the Fermi-Dirac distribution of one particle per quantum state, the Cooper pairs have zero spin, hence have many attributes of bosons that follow the Bose-Einstein distribution and have no limit on the number of identical non-interacting particles per state*[59]*. However, due to interaction between the Cooper pairs, the weakly coupled Cooper pairs satisfy a mixed statistics in which the Pauli principle holds for pairs with the same k value, because there are roughly 10^6 pairs in the volume occupied by a given pair. This is also the justification to use statistical mean field approximation to solve many body problems in the BCS theory.

Unlike the ground state of Fermi gas of non-interacting electrons, the filled Fermi sea that allows arbitrarily small excitations, the BCS theory demonstrates a superconducting ground state separated by a uniform finite *energy gap* E_g of the order $k_B T_C$ from its lowest excited state. Unlike energy gaps in semiconductors, the excitation energies for quasi particles, i.e. the Cooper pairs, are positive for both above and below the Fermi momentum. The energy E_g is centered around the Fermi energy E_F, however, E_F is usually taken as the zero energy scale because typical values of E_g and E_F are a few meV and about 5 eV, respectively. The energy gap, which is closely related to the binding energy of Cooper pair, at 0 k is*[56]*

$$E_g = \frac{\hbar\omega_D}{\sinh\left[\frac{1}{N_F U}\right]} \approx 4\hbar\omega_D e^{-\left(\frac{1}{N_F U}\right)} .$$

Temperature dependencies of normalized energy gap calculated from BCS theory along with experimental data from elemental superconductors are presented in Figure 1*[56]*. The energy gap decreases as the temperature increases and disappears at T_C. Temperature dependence of the energy gap near T_C can be approximated by*[56]*

$$E_g \approx 3.06\, T_c (1 - T/T_c)^{1/2} .$$

At low temperature, $T/T_C < 10$, exponential temperature dependence of electron specific heat capacity, a typical result associated with excitation across a constant energy gap, is obtained because E_g is almost constant within this temperature range, Figure 1. Moreover, the critical field and most of the electromagnetic properties are results of the energy gap. However, in very rare cases, superconductivity is observed without an actual energy gap.

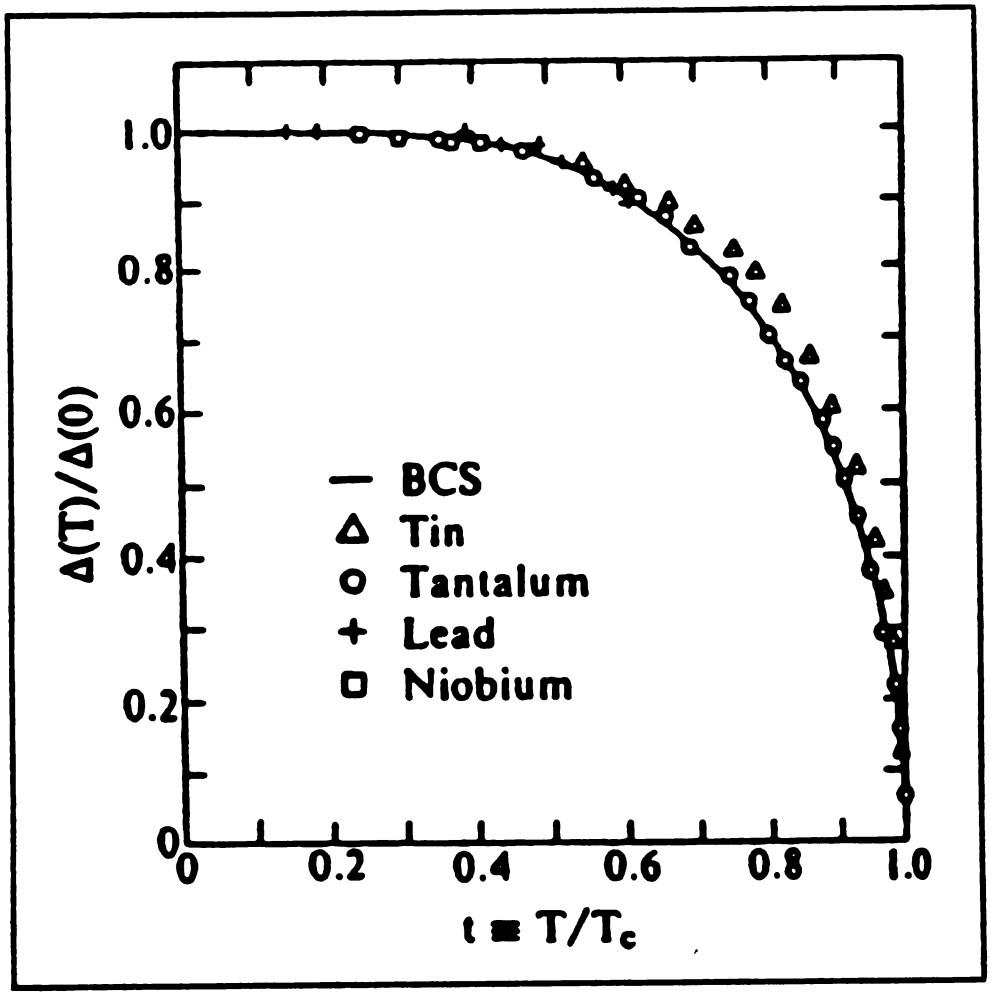

Figure 1. Temperature dependence of normalized energy gap, calculated from the BCS theory and experimental data.
G. Burns, High Temperature Superconductivity - an Introduction, Academic Press*[56]*

2.1.3.3 Critical Temperature and Isotope Effect

The BCS theory predicts a second-order phase transition to a new electron state with the critical temperature given by*[55,56]*

$$T_c = 1.14\,\theta e^{-1/(N_F U)} \quad \text{or}$$

$$K_B T_C = 1.14\,\hbar\omega_D e^{-1/(N_F U)} .$$

The ***isotope effect***, i.e. T_C proportional to inverse square root of the atomic mass of the isotope, is the direct result of atomic mass dependence of the Debye temperature θ. An interesting consequence suggested by the above equation is that a good superconductor, in the sense of high T_C, is a bad conductor at room temperature because the room temperature electrical resistivity is a measure of electron-phonon interaction and can be used to estimate the electron-phonon interaction matrix elements U. Since the expression for $k_B T_C$ is in the same form as that for the energy gap E_g, the BCS theory predicts the parameter free ratio $E_g/k_B T_C$ to be 3.52 which can be used to get an idea of the validity of weakly coupled pairing theory for a given superconductor.

2.1.3.4 Probability Amplitude of Cooper Pairs

For a boson gas with a large number of bosons in the same orbital, the probability amplitude can be treated as a classical quantity consisting of an amplitude and a phase; therefore, both the amplitude and phase are meaningful and observable. For example, the electric field intensity, with observable amplitude and phase, acts qualitatively as the probability amplitude for photons when the total number of photons is large. The particle probability amplitude $\Psi(r)$ for Cooper pairs, the center of mass wave function of

Cooper pairs or the Ginzburg-Landau order parameter, with net momentum can be expressed as*[56]*

$$\Psi = \Psi_0\psi(r) = \Psi_0 e^{i\theta(r)} = n_s'^{1/2} e^{i\theta(r)} \quad \text{and}$$

$$\Psi^* = \Psi_0\psi^*(r) = \Psi_0 e^{-i\theta(r)} = n_s'^{1/2} e^{-i\theta(r)},$$

where n_s' is the density of Cooper pairs, and $\theta(r)$ is the phase.

The London equation can be obtained using the particle probability density as follows*[55]*:

From the Hamilton equation of mechanics, the velocity of particle is

$$\mathbf{V} = \frac{1}{m}\left(\mathbf{p} - \frac{e'}{C}\mathbf{A}\right) = \frac{1}{m}\left(-i\hbar\nabla - \frac{e'}{C}\mathbf{A}\right) \quad .$$

The electric current density j of the supercurrent is given by the particle charge e' times the particle flux $\Psi^*\mathbf{v}\Psi$.

$$\mathbf{j} = e'\Psi^*\mathbf{v}\Psi = e'\frac{n_s'}{m'}\left(\hbar\nabla\theta - \frac{e'}{C}\mathbf{A}\right)$$

Taking curl of both side and using the fact that curl of a gradient of a scalar is identically zero and the relation $\mathbf{B} = \nabla \times \mathbf{A}$, the London equation is obtained.

$$\nabla\times\mathbf{j} = \frac{n_s'e'^2}{m'C}\mathbf{B}$$

This accounts for the ***Meissner effect*** and the ***penetration depth*** as described in London's theory.

The coherence length can be derived by modifying the phase part of the one-dimensional plane wave particle amplitude probability, $\psi(x) = \exp(i kx)$, to a strongly modulated wave function*[55]*

$$\varphi(x) = 2^{-1/2}\left(e^{i(k+q)x} + e^{ikx}\right).$$

Thus, the probability density, $(\Psi_0\psi^*)(\Psi_0\psi) = n_s'(1 + \cos qx)$, is modulated instead of a uniform density, $\Psi^*\Psi = n_s'$, of the plane wave. Increase of energy due to the modulation can be calculated from the kinetic energy difference, assuming $q << k$ *[55]*.

$$\int dx\varphi^*\left(-\frac{\hbar^2}{2m'}\frac{d^2}{dx^2}\right)\varphi - \int dx\psi^*\left(-\frac{\hbar^2}{2m'}\frac{d^2}{dx^2}\right)\psi$$

$$= \frac{\hbar^2}{2m'}\left\{\frac{1}{2}\left[(k+q)^2 + k^2\right] - k^2\right\} \approx \frac{\hbar^2}{2m'}kq$$

This energy increase may not exceed the energy gap E_g, otherwise the superconductivity will be destroyed. Thus, the ***intrinsic coherence length*** ξ_0, interpreted as the mean spacing between pair of electrons for a given Cooper pair, can be defined based on the critical value of the modulation q_0 *[55]*.

$$\xi_0 \equiv 1/q_0 = \frac{\hbar^2 k_F}{2m'E_g} = \frac{\hbar v_F}{2E_g}$$

where k_F is the highest possible k value, and the corresponding v_F is the electron velocity at the Fermi surface. A more precise result given by the BCS theory is*[55]*

$$\xi_0 = 2\hbar v_F / \pi E_g .$$

Flux quantization is an important characteristic of superconductivity that restricts the magnetic flux through a hole or non-superconducting region in a superconductor disk to integral multiples of a quantity Φ_0 called fluxoid or flux quantum. This result can be derived from the expression for supercurrent density j in this section. If j is integrated along a closed path C, deep in a superconductor ring, the result is zero because there is no supercurrent in the interior of a superconductor, i.e.*[55,56]*

$$\oint_c \mathbf{j}\cdot d\mathbf{l} = \frac{e'}{m'}|\Psi|^2 \oint_c \left(\hbar\nabla\theta - \frac{e'}{C}\mathbf{A}\right)\cdot d\mathbf{l} = 0$$

$$\text{or} \quad \hbar\oint_c \nabla\theta \cdot d\mathbf{l} = \frac{e'}{C}\oint_c \mathbf{A}\cdot d\mathbf{l} \ .$$

Integration of $\nabla\theta$ along a path gives the phase change $\Delta\theta$ from starting point to end point which has to be integral multiple of 2π, i.e. $2\pi n$, for a closed path. Applying Stock's theorem to convert the integral of **A** into a surface integration over area S bounded by C, yields*[55,56]*:

$$\hbar\oint_c \nabla\theta\cdot d\mathbf{l} = 2\pi n\hbar = \frac{e'}{C}\oint_c \mathbf{A}\cdot d\mathbf{l} = \frac{e'}{C}\int_s \nabla\times\mathbf{A}\cdot d\mathbf{s} = \frac{e'}{C}\int_s \mathbf{B}\cdot d\mathbf{s} = \frac{e'}{C}\Phi \ .$$

Define the ***fluxoid*** $\Phi_0 \equiv 2\pi\hbar C / e'$. The total flux Φ through the superconductor ring becomes

$$\Phi = n\left(\frac{2\pi\hbar C}{e'}\right) = n\Phi_0 \ .$$

The value of e' was determined to be 2e by experimentally measurement of Φ. This result $\Phi_0 = 2\pi\hbar C / (2e)$ is in agreement with the electron-pairing theory. The flux quantization is a good example of long-range quantum effect that the coherence of the superconducting state extends over a ring or solenoid.

Under suitable conditions superconducting electron pairs can move from a superconductor through a thin insulator layer into another superconductor if the layer thickness is smaller than the coherence length of the superconductors. This phenomenon is called ***Josephson superconductor tunneling****[55]*. This phenomenon can be described using the phase difference, $\Delta\theta = \theta_1 - \theta_2 = \Delta\theta_0 - 2eVt/\hbar$, of the particle probability amplitudes between the two sides of the junction, where V and t are the dc voltage applied across the junction and time. The supercurrent density across the junction is*[55]*

$$j = j_0 \sin(\Delta\theta_0 - 2eVt/\hbar)$$

As a result, the ***dc Josephson effect*** refers to a dc current across the junction in the absence of any electric or magnetic field, and the ***ac Josephson effect*** refers to a rf oscillating current across the junction with an applied dc voltage. The oscillation current has a angular frequency $\omega = 2eV / \hbar$, e.g. 1 μV applied voltage produces a frequency of 483.6 MHz. This can be interpreted as that a photon of energy $\hbar\omega = 2eV$ is emitted or absorbed when an electron pair crosses the biased junction. Besides the junction with insulator middle layer, i.e. SIS junction, the dc Josephson effect is also observed on junction with normal metallic middle layer, i.e. SNS junction. Josephson junctions, which can be used as high speed switching devices, are the key element of superconducting electronic devices. This is due to the characteristic current-voltage relation with two well defined voltage states $\pm V_c$, which are related to the energy gap by $E_g = e\, V_c$, Figure 2*[55]*. A very important application of the Josephson junctions is the superconductor quantum interference devices (SQUIDS) which are used as high sensitive magnetometers. The operation of SQUIDS is based on the ***macroscopic quantum interference*** that is another example of long-range quantum effect of superconductivity. Similar to the derivation of flux quantization, the total flux Φ passes through the loop in Figure 3*[55]* is related to the phase difference going once around the loop, Δθ, by $\Delta\theta = (2e / \hbar C)\Phi$. The phase differences caused by the magnetic flux at junction a and b are $e\Phi /(\hbar C)$ and $-e\Phi /(\hbar C)$, respectively. Total current density j is*[55]*

$$j = j_a + j_b = j_0\left[\sin\left(\Delta\theta_0 + \frac{e}{\hbar C}\Phi\right) + \sin\left(\Delta\theta_0 - \frac{e}{\hbar C}\Phi\right)\right]$$

$$= 2j_0 \sin\Delta\theta_0 \cos\frac{e\Phi}{\hbar C}\,.$$

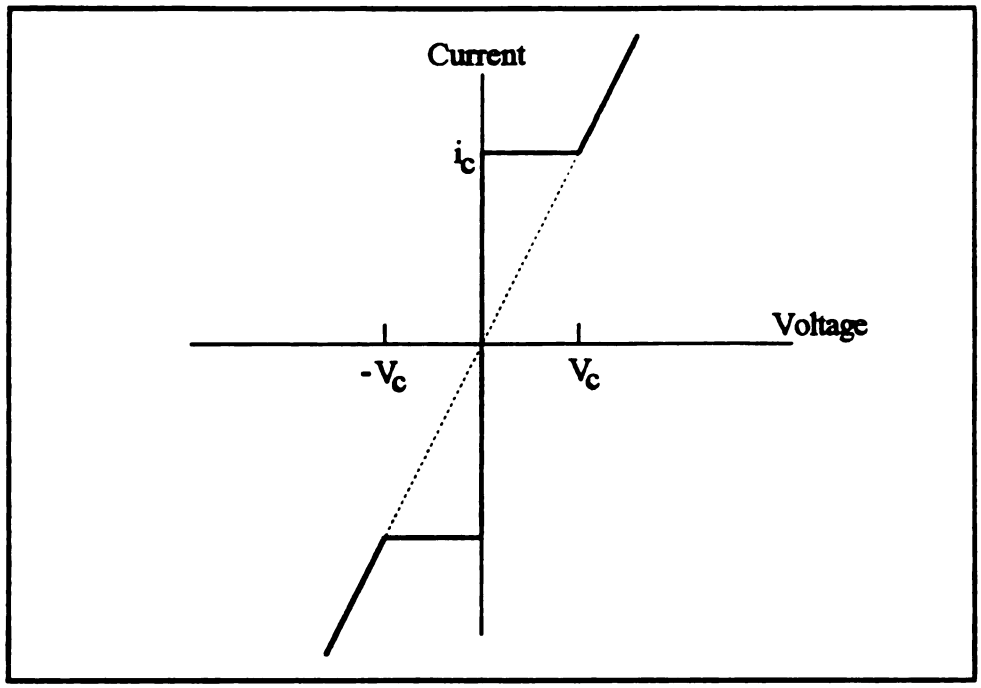

Figure 2. Current-voltage characteristic of a Josephson junction.

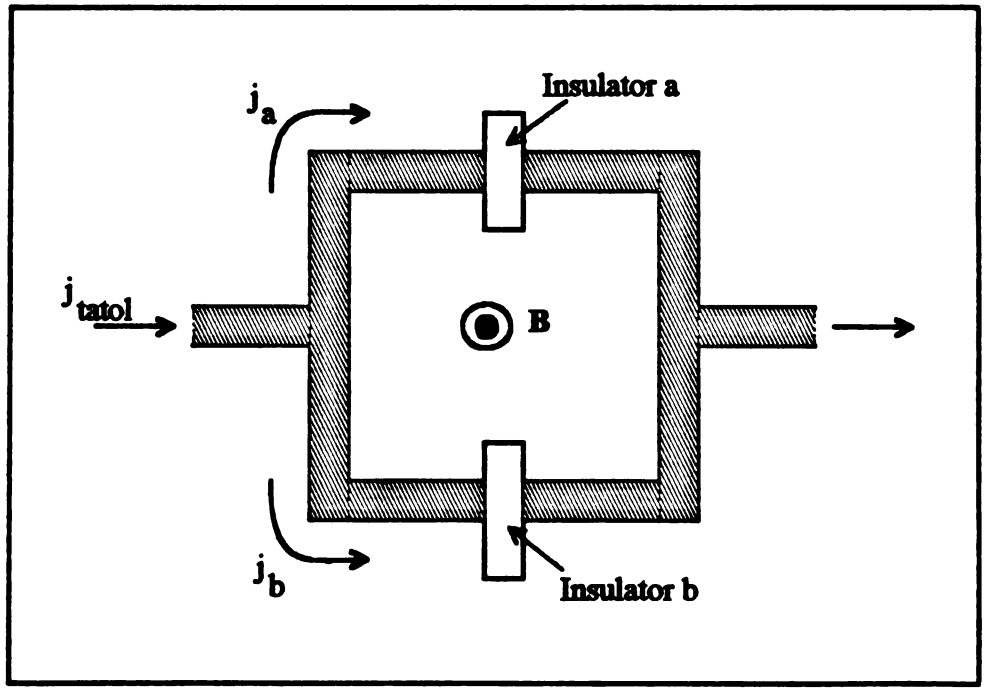

Figure 3. Microscopic quantum interference experiment setup

2.1.4 Type II Superconductors

Most pure elemental superconductors are type I superconductor that show complete Meissner effect up to the thermodynamic critical field H_C, the critical magnetic field calculated from free energy balance, and becomes normal conductor in a field larger than H_C, Figure 4(a). On the other hand, the type II superconductors, Figure 4(b), maintain complete Meissner effect up to the lower critical field H_{C1} and carries some magnetic flux between the lower and upper critical field; however, the zero resistance state is preserved up to the upper critical field H_{C2}.

Using the Ginzburg-Landau equation, the upper critical field H_{C2} is related to the thermodynamic critical field H_C by*[55]*

$$H_{c2} = \sqrt{2}\,\kappa H_c = \Phi_0 / \left(2\pi\xi^2\right),$$

where $\kappa = \lambda/\xi$ is the Ginzburg-Landau parameter. For $\kappa < 1/\sqrt{2}$, $H_{C2} < H_C$ defines the type I superconductor which shows complete Meissner effect. On the other hand, for $\kappa > 1/\sqrt{2}$, $H_{C2} > H_C$ defines the type II superconductor which shows complete Meissner effect in weak magnetic field, i.e. below H_{C1}, and allow some flux to penetrate regions in normal state surrounded by superconducting matrix in strong field, i.e. between H_{C1} and H_{C2}. The two cases for type II superconductors are called Meissner state and vortex state, respectively. The dimension of a vortex cord can be deduced from the above equation to be in the order of the coherence length because the vortices are packed as close as possible at H_{C2}.

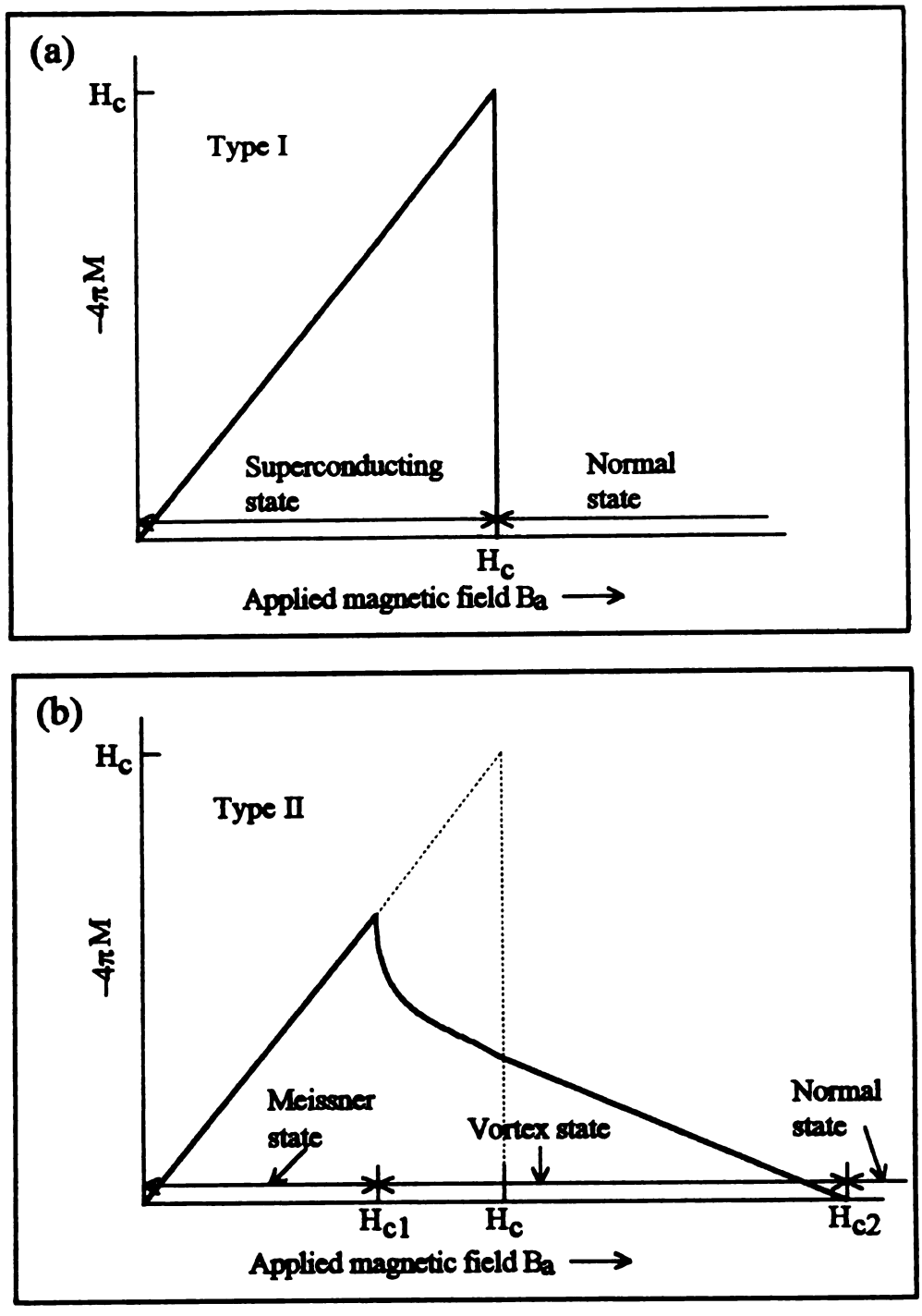

Figure 4. Magnetization verses applied magnetic field for (a) type I and (b) type II superconductors.

Lower critical field H_{c1} also can be related to the thermodynamic critical field H_c by*[55]*

$$H_{c1} = H_c / \left(\sqrt{2}\,\kappa\right) = \Phi_0 / \left(4\pi\lambda^2\right).$$

From the above two equations the thermodynamic critical field is the geometric mean of the upper and lower critical fields. For many type II superconductors, H_{c2} is much larger than H_c, i.e. $\kappa >> 1/\sqrt{2}$, so H_{c1} is very small.

The presence of vortex state can be understood in terms of interfacial energy between normal and superconducting regions. This interfacial energy is positive if κ is small and negative if κ is large. The crossover from positive to negative interfacial energy occurs at $\kappa = 1/\sqrt{2}$. The term vortex state describes the circulation of supercurrent vortices, around thin rods of non-superconducting region within the superconductor each bearing a single fluxoid. This condition can be understood by minimization of magnetic energy associated with the vortices. Assuming a single vortex with n fluxoids, i.e. $B \propto n\Phi_0$, the magnetic energy associated with this vortex is proportional to $(n\Phi_0)^2$. As a result, the magnetic energy is minimized when this vortex splits into n vortices each bearing a single fluxoid. This result agrees with experimental observations.

In the vortex state, vortices repel each other due to the Lorentz force between the circulation current of a vortex and the magnetic field of its neighbor. As a result, the repulsion energy is minimized when the vortices form a close-packed hexagonal array, referred as the ***vortex lattice or flux lattice***. However, vortex energy can be lowered by associating the vortex with some structural defects of the superconductor called the ***pinning center***. For a given structural defect to be an effective pinning center, the dimension of the defect has to be comparable to the size of vortex cord, i.e. in the order of the coherence length. For a type II superconductor with randomly distributed pinning centers, the vortices are also randomly distributed, and referred as the ***vortex glass or flux glass***.

Considering a current J flowing perpendicularly to the magnetic field H through a vortex lattice, i.e. no pinning of the vortices, the Lorentz force acting on the vortices pushes the vortices in the J×H direction. This motion of magnetic flux in turn induces an electric field that opposes the current J, resulting in energy dissipation and appearing as an electrical resistance! Thus, the dynamics of vortices is of technological importance.

Motion of the vortices can be classified into two major types, i.e. flux creep and flux flow. ***Flux creep*** refers to the case that thermal energy and Lorentz force are smaller than the average pinning energy; therefore, vortex motion and electrical resistance are tolerable for many applications. Flux creep is found immediately after the change of external field or current and decays logarithmically. It can be detected by measuring the trapped magnetic field or the electrical resistance. On the other hand, ***flux flow*** occurs when the thermal energy and Lorentz force are large enough to overcome the pinning force. Under this condition, referred as the ***vortex liquid***, the vortices move steadily, and the material is useless as a low-loss conductor. By measuring the transition temperature from vortex liquid to vortex glass T_g under different magnetic field, a phase boundary can be added to the phase diagram of a type II superconductor, Figure 5*[56]*.

For high T_C superconductors, which are type II superconductors, a unique magnetic property is that temperature dependence of the magnetic moment M becomes irreversible at some temperature, called the ***irreversible temperature*** T_{IRR}, for a given magnetic field. If a Zero field cooled sample is warmed up in some given magnetic field to a temperature above T_{IRR}, the M vs. temperature curve will not take the reverse of the original warm-up path when the sample is cooled down in the applied field, Figure 6*[56]*. Similar to the vortex liquid-glass phase boundary, an ***irreversibility line*** can be defined for a given high T_C superconductor. The vortex liquid-glass phase boundary and the irreversibility line for a given superconductor are similar because both of them are closely related to the pinning potential of the superconductor.

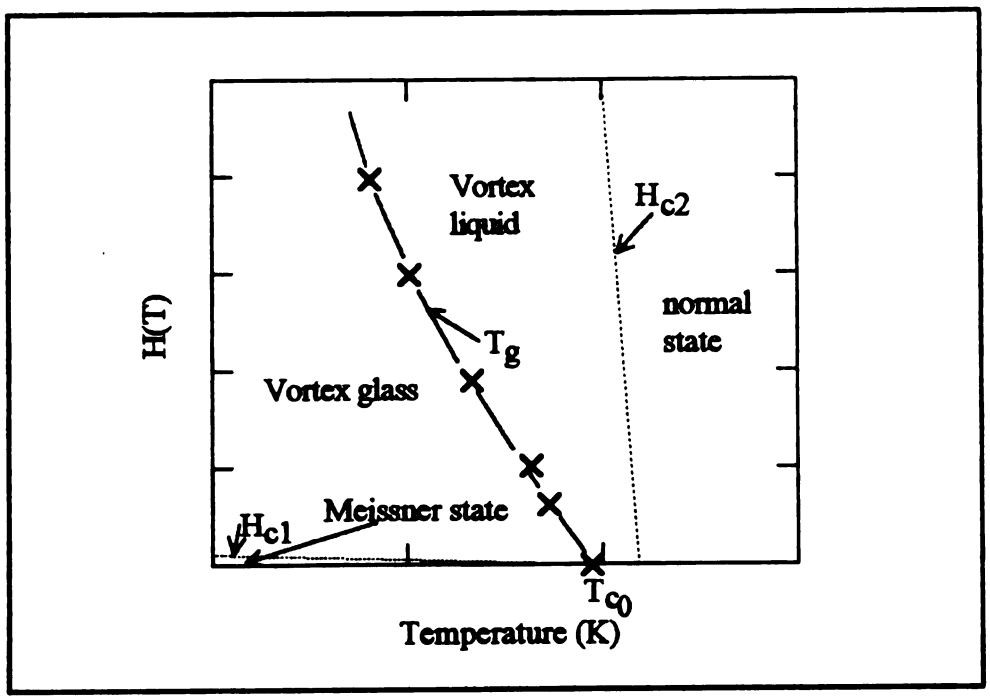

Figure 5. A sketch of magnetic phase diagram of a type II superconductors

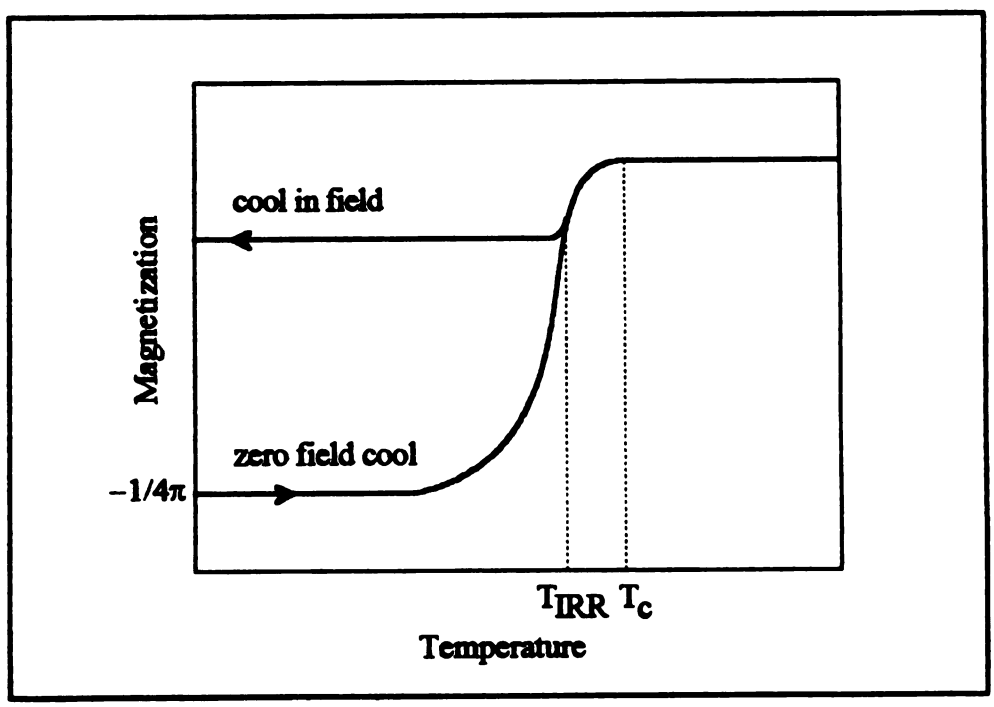

Figure 6. Temperature dependence of magnetization of a superconductor with a irreversible temperature

2.1.5 Applicability of BCS Theory to Strongly Coupled and High T_c Systems

Despite the simplifying assumptions, i.e. k independent weak coupling and spherical Fermi surface, the predication of essentially all known superconducting properties based on the BCS theory generally agree well with experimental results for most conventional low T_c superconductors. However, certain deviations are observed especially for so called "bad actors" such as lead and mercury with very strong electron-phonon coupling such that T_c becomes a reasonable fraction of the Debye temperature.

The mean field approximation used to derive the BCS results becomes less appropriate when the number of pairs, whose center of mass fall within the volume occupied by a given pair, approach the order of unity as in the strongly coupled high T_c superconductors. In contrast to conventional superconductors with coherence length between 100 nm to $1x10^3$ nm, the layered high T_c superconductor systems have coherence length about 1.5 to 3.0 nm in the a-b plane and as small as 0.3 nm in the c direction. Nevertheless, the BCS theory continues to work sufficiently well on many aspects of these strongly coupled systems.

It should be noted that the phonon-mediated pairing used in the BCS theory does not restrict the use of the basic formalism in systems with other pairing mechanism*[58]*. In fact, the basic equations for the BCS condensed state apply not only to the weakly coupled Cooper pairs but also to strongly coupled electron pairs and other fermion pairs that resulted in boson-like condensation. A typical example is the super-fluid transition in He^{III}, a fermion with a half nuclear spin. Below the transition temperature, liquid He^{III} atoms form BCS-like pairs with a spin of 1 per-pair and p orbital angular momentum, p-wave, instead of spin zero and s-wave for the Cooper pairs.

2.2 High T_C Oxide Superconductors

The term ***high temperature or high T_C superconductor*** is generally referred to a class of complex metal cuprates that have a defective perovskite structure with one or more Cu-O plane. The Cu-O plane is the essential feature of this class of materials because it is believed that the Cu-O plane is responsible for the superconducting properties. $(La_{2-X}Sr_X)CuO_4$*[60]*, discovered in 1986, with T_C about 38 K is the first compound in this class, but it is not the first oxide superconductor. Oxygen-deficient $SrTiO_{3-X}$, found in 1965, is the first oxide superconductor, while the highest T_C among oxide superconductors without the Cu-O plane is about 13 K for $Ba(Pb_{1-X}Bi_X)O_3$*[61]* or about 30 K for $(K_{0.4}Ba_{0.6})BiO_3$*[62,63]*, before or after 1986. Although all these oxides mentioned are related to the perovskite structure, it is not clear that superconductivity in these oxides are related to the high T_C superconducting cuprates.

Three most important high-T_C (high critical temperature) oxide superconductor systems are Y-Ba-Cu-O (yttrium-barium cuprates or rare earth-barium cuprates), Bi-(Pb)-Sr-Ca-Cu-O (bismuth-lead-strontium-calcium cuprates), and Tl-Ba-Ca-Cu-O (thallium-barium-calcium cuprates). These systems are often referred as YBCO, BSCCO and TBCCO systems. All these three systems have complicated crystal structures with copper-oxygen planes, which are believed to be responsible for the superconducting properties of these compounds. Among these cuprates Tl-Ba-Ca-Cu-O system has the highest T_C, about 125 K*[1,2]*.

$YBa_2Cu_3O_X$ (1-2-3 compound), with T_C around 95 K, is considered to be the most favorable oxide superconductor for thin film applications because, in comparison with other systems, it has a less complicated chemistry and structure, good phase stability and a high critical current density*[3]*. On the other hand, $Bi_{2-X}Pb_XSr_2Ca_2Cu_3O_Y$ (2-2-2-3 compound) of the Bi-(Pb)-Sr-Ca-Cu-O system, with T_C about 110 K, is a good candidate

for tape application due to its thin plate shaped grains that facilitate mechanical alignment of the grains to obtain higher transport critical current density*[33-34]*.

2.3 Crystal Structures of High T_c Superconductors

All three important high T_c systems can be visualized as stacking of various perovskite cells with some defects in the cells or in stacking. Figure 7 shows two different ways of drawing a perovskite unit cell that has a ABO_3 formula. Many perovskite metal oxides, e.g. $BaTiO_3$, are well known for their ferroelectricity. Two distinct cation sites exist in the structure. A cation occupies the larger site with coordination number of twelve, on the other hand, the smaller B cation sits in the oxygen octahedron. In high T_c superconducting cuprates, copper ions occupy the B cation sites while other larger cations occupy the A cation sites. Due to oxygen deficiency or other variation from the standard perovskite structure, the nearest oxygen ions of the copper cation is often less than six. In fact, copper-oxygen plans with four oxygen ions per copper cation are the key feature of high T_c oxide superconductors.

There is an important relation between T_c and structure of these superconducting cuprates, that T_c increases as the number of adjacent Cu-O planes (n) increases, at least up to n = 3. These adjacent planes , that sandwich sparsely occupied Y-atom or Ca-atom plane, are separated by a distance of about 3.2 Å. This distance is approximately the same for all high T_c cuprates and is smaller than the standard perovskite cell size or lattice parameters a or b of the high T_c cuprates. T_c of superconducting cuprates is less than 77 K for n = 1, about 85 to 95 K for n = 2, and more than 100 K for n = 3.

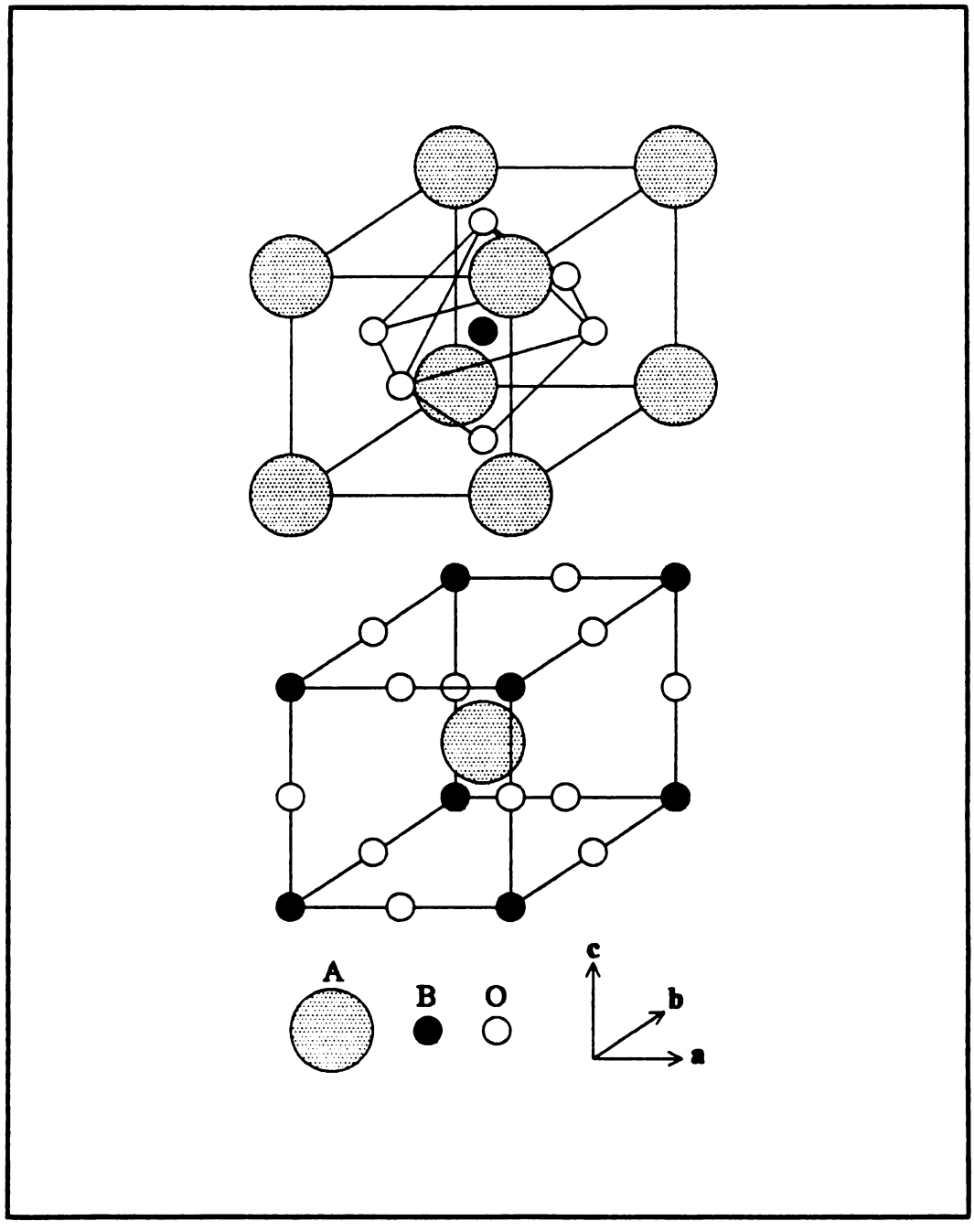

Figure 7. Two different ways of drawing a ABO_3 perovskite unit cell

2.3.1 $YBa_2Cu_3O_{7-\delta}$ (YBCO)

An YBCO unit cell consists of three oxygen deficient perovskite cells. Figure 8 shows the unit cell of an orthorhombic YBCO with seven oxygen ions per unit cell, i.e. $\delta = 0$, where the top and bottom Cu-O plans have no oxygen ions in "a" direction, and the middle cell has no oxygen ions on the side edges. Two types of copper ions exist. Copper ions in the middle of the unit cell form Cu-O plans, with four planar nearest oxygen ions, while the copper ions at the top and bottom of the unit cell (also having four planar nearest oxygen ions) form one-dimensional chains in the "b" direction. The two adjacent Cu-O planes are separated by a sparsely occupied Y-atom plane. The distance between these adjacent Cu-O planes is about 3.2 Å while the separation between two sets of these adjacent planes is > 8.2 Å.

At high temperatures, $YBa_2Cu_3O_{7-\delta}$ loses additional oxygen ($\delta > 0$) from the top and bottom Cu-O planes, accompanied by a decrease of the oxygen ordering in these planes. The structure of YBCO becomes tetragonal when $\delta \gtrsim 0.7$. The change in oxygen content, and the orthorhombic-tetragonal phase transition are reversible with transition temperature around 700 °C*[64-70]*. The tetragonal phase is semiconducting, and the fully oxygenated orthorhombic phase is metallic and superconducting above and below T_c, respectively. The oxygen content in the orthorhombic phase is important because T_c increases with increasing oxygen content and reaches the maximum with $\delta \lesssim 0.1$.

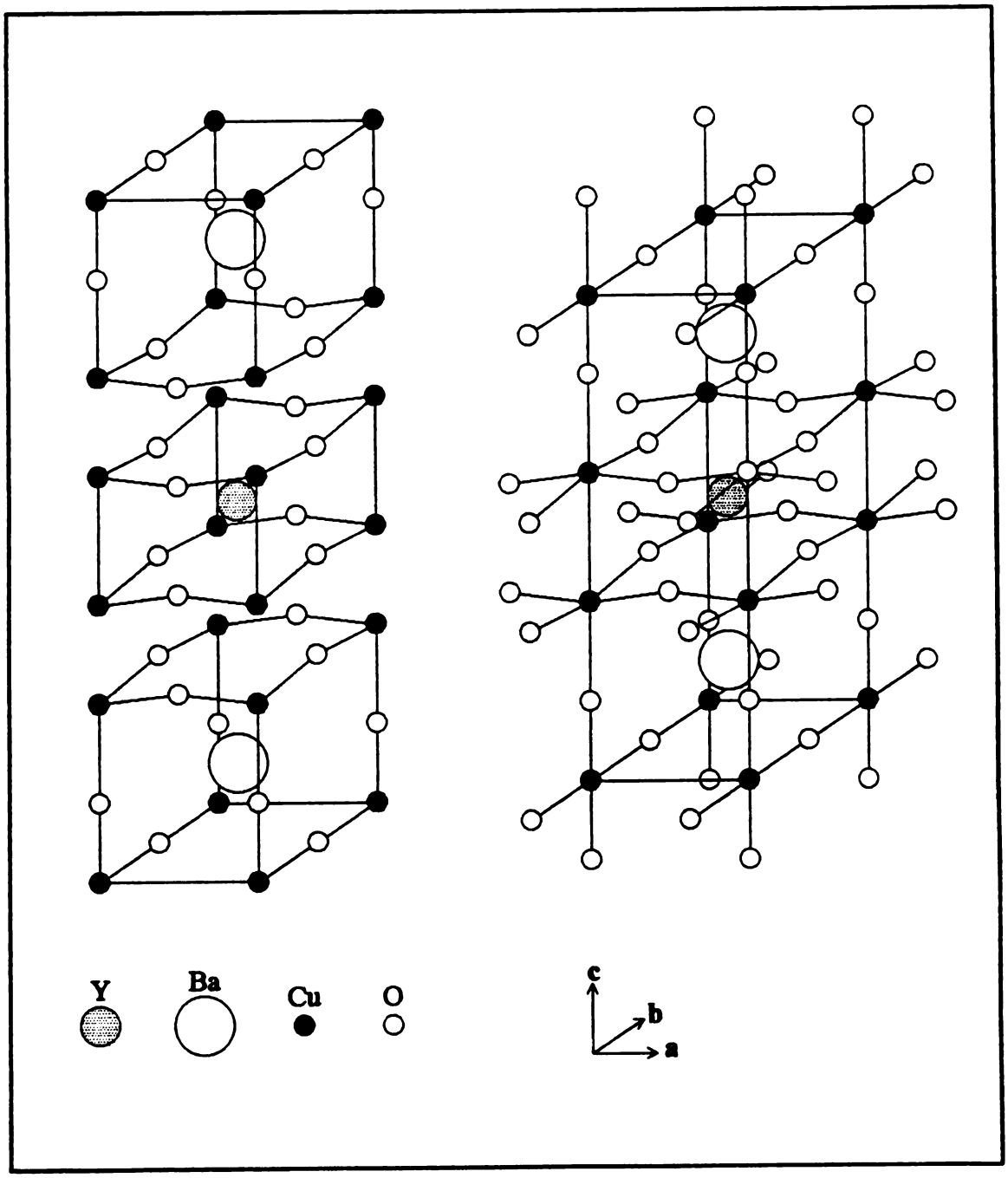

Figure 8. YBCO unit cell

2.3.2 BSCCO System

The high T_c Bi-Sr-Ca-Cu-O superconducting system has a number of phases with different critical temperatures (T_c). The three major phases are referred to by their cation ratios as 2201 (T_c below 77 K), 2212 (T_c ~ 85 K), and 2223 (T_c ~ 110 K) phases*[35]*. The structures of these phases are very similar to the structure of $(La_{2-x}Sr_x)CuO_4$. For simplicity the following discussion is based on the un-doped La_2CuO_4 (La-Cu-O). Conventional unit cell of La-Cu-O contains two chemical formula units, i.e. $2(La_2CuO_4)$. Similar to the YBCO unit cell, this cell is also composed of three perovskite cells; however the top and bottom cells are displaced as shown in Figure 9. Similarity between the BSCCO phases and La-Cu-O can be seen in Figure 10.

The structure of 2201 phase can be obtained by inserting two pairs of Bi-O planes into the La-Cu-O structure and replacing the La atoms with the Sr atoms, Figure 11. The La-Cu-O and 2201 phase have n = 1 and low critical temperatures.

The 2212 structure is obtained by splitting the copper-oxygen octahedrons and inserting a Ca-atom plane in between, Figure 12. It is clear that n = 2 for this structure. Similarly, the 2223 phase can be derived from the 2212 phase by inserting an additional Cu-O plane and a Ca-atom plane as shown in Figure 13. As a result the 2223 structure has n = 3 and $T_c > 100$ K.

Tl-Ba-Ca-Cu-O system also has 2201,2212 and 2223 phases that have exactly the same structures as the corresponding BSCCO phase with Tl replacing Bi and Ba replacing Sr.

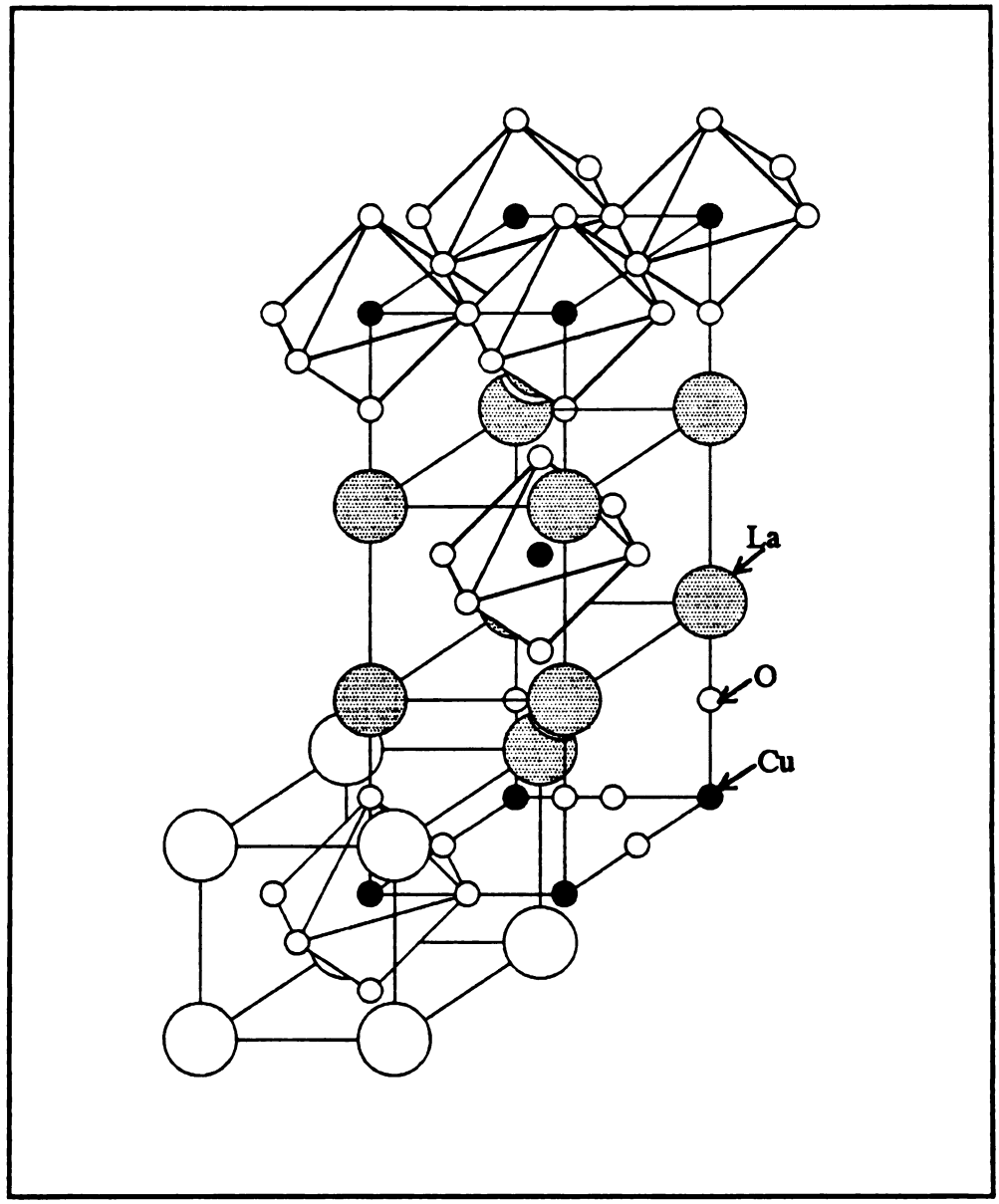

Figure 9. 2 (La_2CuO_4) unit cell

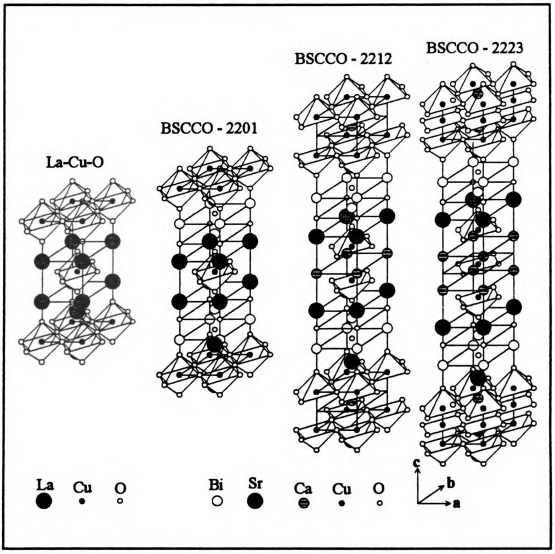

Figure 10. Unit cells of $2(La_2CuO_4)$ and BSCCO phases

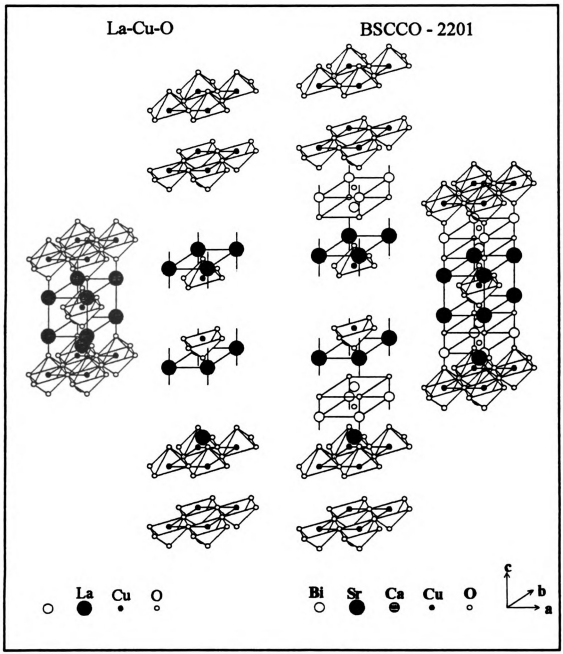

Figure 11. Relation between crystal structures of La_2CuO_4 and BSCCO - 2201

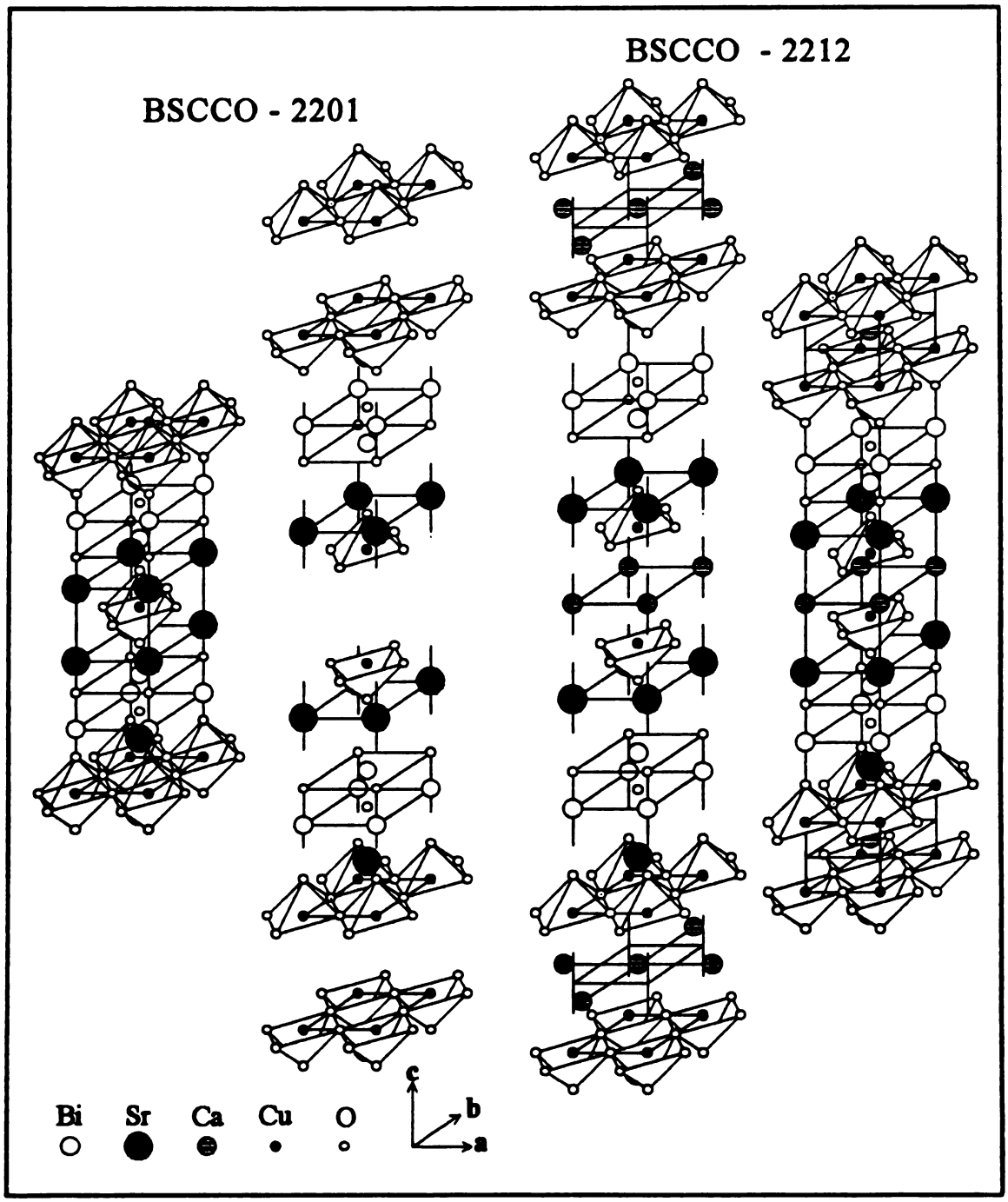

Figure 12. Relation between crystal structures of BSCCO - 2201 and -2212

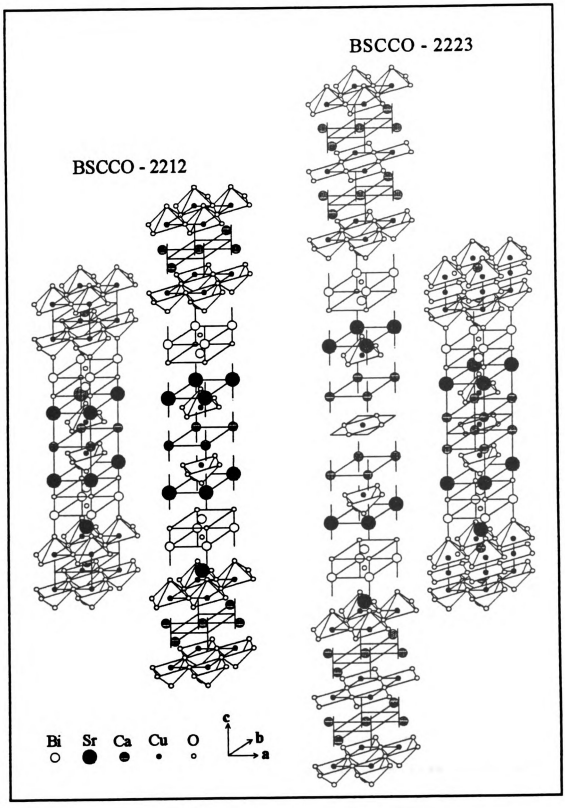

Figure 13. Relation between crystal structures of BSCCO - 2212 and - 2223

2.4 High Tc Superconductor Thin Film Deposition Techniques

Since the discovery of high Tc superconductors, many techniques, most of them from semiconductor processing, have been adapted to fabricate superconductor thin and thick films. Almost all high T_C superconductor thin film deposition techniques can be categorized as physical or chemical vapor depositions. Examples of physical vapor depositions are laser evaporation or ablation*[3,5-23]*, plasma or ion beam sputtering*[71-74]*, electron beam or molecular beam epitaxy*[75-77]*, and thermal evaporation*[78-80]*. Examples of chemical vapor depositions is organometallic chemical vapor deposition*[81]*. All vapor deposition processes involve three major steps which are*[82]*:

1. Creation of vapor phase species by thermal energy, photon energy or kinetic energy
2. Transport of the vapor species from source to substrate: Dependent on the deposition technique used, this transport can occur without much collisions between atoms and molecules, i.e. under molecular-flow condition, or with many collisions in the vapor phase species, i.e. higher partial pressure of the vapor and/or gas species or some ionized species.
3. Film growth on the substrate: Dependent on deposition rate and mobility of atoms especially in the surface and near-surface, the as deposited film can be amorphous or crystalline. Increasing energy of the vapor species (e.g. producing species in excited state or increasing velocity of vapor species), increasing substrate temperature and/or bombardment of the growing film by ions in the vapor species will increase the mobility of atoms on the growing film; thus, promote nucleation and growth of crystalline films.

Deposition rate, stoichiometry and crystalline quality are the most important parameters in depositing high quality superconductor thin films. The first parameter mainly depends on the first two steps of the vapor deposition process; while the crystalline quality depends primarily on the film growth step of the above model. Therefore, it will be much easier to optimize these three parameters if three major steps in the vapor deposition process can be independently controlled. For all physical vapor deposition techniques mentioned above, these three deposition steps can, more or less, be independently controlled. On the other hand, in the chemical vapor deposition technique, it is difficult to separate these three steps because the deposition species are created right on the surface of the hot substrate, i.e. all three major steps of vapor deposition occurred simultaneously. Nevertheless, if complicated substrate geometry is necessary, chemical vapor deposition is the only non line-of-sight deposition method among all techniques mentioned.

2.4.1 Pulsed Laser Deposition (PLD) of Superconductor Thin Films:

Among the techniques which have been adapted to grow high Tc superconductor thin films, pulsed laser ablation or pulsed laser deposition is the most widely studied and most successful one. The key reasons for the success of the PLD process are its stoichiometry conservation property, and excited high energy vapor species, i.e. excited and ionized species, it produced*[42-46]*. Because of these two properties, high quality epitaxial film of complicated composition, such as YBCO superconductor, can be made in situ at low temperature (400 - 650 °C) with a relatively large degree of freedom in processing parameters*[4,12,14]*. A collection of various PLD processing parameters, and properties of resulting films (since the first reported successful PLD deposition of high T_C superconducting thin films*[4]*) is shown on next page, Table 1.

Table 1. Various PLD processing parameters and properties of 1-2-3 films associated with these processing parameters

wave-length nm	pulse-energy density J/cm^2	peak-power density MW/cm^2	SUBSTRATE	substrate temperate °C	P_{O2} mTorr	in-situ superconducting	T_{co} K	J_C @ 0T MA/cm^2	note [reference]
193	3	–	(100)SRTIO3	400	0.1	YES	85	.10@80K	plasma assisted PLA with +300V dc ring electrode between substrate (floating) and target(-) [10]
193	3.5	117	SRTIO3	730	200	YES	89	1.4@77K	[16]
193	–	–	YSZ/Ni-alloy	700	–	YES	-	.25@77K	[20]
248	3.5	117	SRTIO3	730	200	YES	90	2.5@77K	[16]
248	–	–	MGO	670	400	YES		4-6@77K	substrate annealed at 1100-1200°C for 12-24h to create high density of atomic steps [19]
248	–	–	YSZ	650	200	YES	90	1.0@77K	[19]
248	–	–	YSZ	650	200	YES	90	1.8@77K	1-2-3 / 30% silver target [19]
248	–	–	LaAlO3	650	200	YES	90	6.5@77K	1-2-3 / 30% silver target [19]
248	1.5	–	(100)YSZ	710	200	YES	90	5.0@77K	[22]
248	1.5	–	(100)YSZ	765	200	YES	90	.50@77K	[22]
308	4-5	67-83	(100)SRTIO3	720-780	100-300	YES	91	2.2@77K	1.5@77K with 2T field [12]
308	3.0	67	SRTIO3	650	200	YES	88	5.0@77K	[14]
308	3.0	67	YSZ	650	200	YES	89	1.0@77K	[14]
308	3.0	67	YSZ	550	200	YES	88	—	with +300V dc bias-ring between substrate (floating) and target (ground) [14]
308	3.0	67	YSZ	550	200	YES	80	—	[14]
355	3.2	400	SRTIO3	600	200	NO	–	—	[13]
355	3.2	400	SRTIO3	600	200 N_2O	YES	65	—	[13]
355	3.2	400	SRTIO3	600	200 N_2O	YES	84	.35@54K	with a second ArF excimer laser to produce atomic oxygen $O(^1D)$ near the substrate surface [13]
355	3.2	400	SRTIO3	700	200	YES	93	1.3@88K	[13]
532	3.2	400	SRTIO3	725	200	YES	93	lower than above	lower Jc and more rough surface than 3rd harmonic (355nm) deposited film [13]
532 150ns	.5	3.3	YSZ	450	.1	NO	80	—	[8]
1061 1ms	1,000	1	SRTIO3	540	10^{-4}	NO	61	—	excited oxygen by a 300W rf dosor [15]
1,064	.8	53	MGO	500	10^{-3}	NO	79		non-stoichiometric target [9]
1,064	3.5	388	SRTIO3	730	200	YES	–	.25@77K	[16]
10.6mm 150ns	22.5	150	(100)SRTIO3	400	.3	NO	86	.03@77K	non-stoichiometric target [7]
1064 .5-2.5ms	40-300	.05-1	AG & AG/YSZ	200-750	100	NO	~77	—	this study

A typical setup for pulsed laser deposition, Figure 14, consists of a pulsed laser source, a vacuum chamber with optical windows, a rotating target holder, a heated substrate holder, and a source for oxygen gas or activated oxygen atoms/ions. Due to the fact that laser induced plume, i.e. the vapor species, ejected from the target surface moves in a direction normal to the target surface, the substrate holder is positioned parallel to the target and centered to the laser-target interaction spot.

Substrate distance from the target, typically a few centimeters, is critical because of the non-uniform spatial distribution of the vapor species and declining energy of vapor species as they move away from target. For a given deposition condition, the substrate distance also controls the area coverage of deposited film on the substrate. Because stoichiometry is usually preserved during pulsed laser ablation process, a single stoichiometry bulk target is normally used. The target is usually rotating at a low speed to expose different parts of the target to the laser pulse in order to prevent local overheating and erosion of the target. This is because overheating will result in compositional variation of the target by segregation and evaporation, and non-planar target surface will direct the plume away from the substrate.

2.4.1.1 Effect of Pulse-Width and Wavelength of the Laser

Laser pulses used for PLD process typically have a pulse-width of about ten to a few tens of nanoseconds, focused to a few millimeters spot size on the target, and a pulse-energy density of a few J/cm^2 that produces a peak power density in the order of tens to hundreds of million Watts per cm^2. Due to extremely high peak power density and extremely short duration, the laser pulses only affect a very thin surface layer of the target and spontaneously convert it into a vapor or fragments without compositional variation or segregation. Such variation might be expected from excessive melting of the High T_c superconducting materials*[4,83]*.

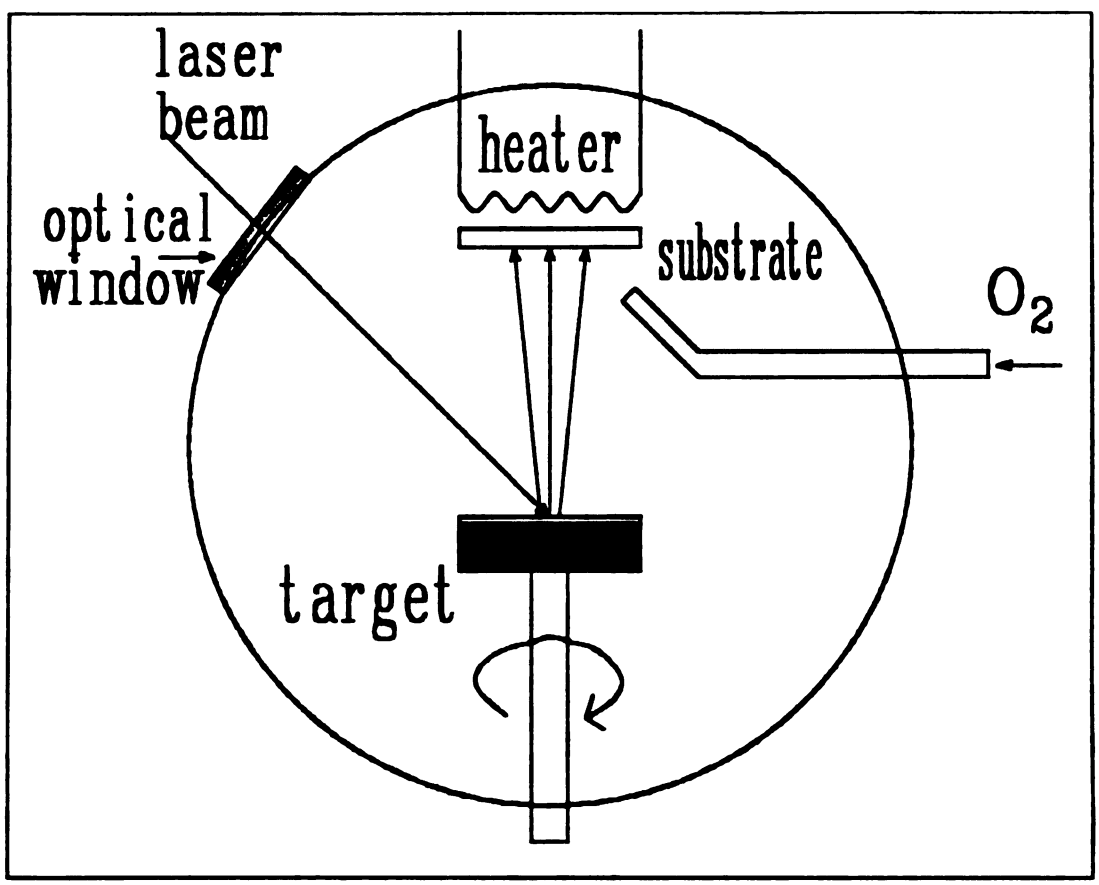

Figure 14. Typical pulsed laser vapor deposition setup

Although superconducting thin films have been successfully deposited with a wide range of wavelengths, i.e. from infrared CO_2 and Nd:YAG laser to ultraviolet excimer laser, highest quality in situ epitaxial films are produced by UV lasers. This is because shorter wavelength lasers have higher photon energy and greater absorption by the plasma plume resulting in a higher degree of decomposition, excitation and ionization of the vapor species by photoionization and other related processes*[16,43]*; thus, the quality of deposited film is enhanced by increased mobility of atoms near the surface of the growing film, Figure 15. Deposition using infrared lasers will result in higher absorption depth and higher deposition rate, but the quality of deposited films are lower than films deposited with UV lasers*[9,16,84]*.

2.4.1.2 Nature of the Laser Induced Plume

Once vapor species formed by initial part of a laser pulse, they are further decomposed, ionized and heated by interacting with the remaining laser pulse. Due to rapid heating and expanding of the laser induced plasma, an intense plume consists of high energy vapor species ejected from the target with very high velocities toward the substrate*[42-46]*.

Important information about laser induced plume, such as vapor species, principle luminescent species, expansion velocities, and extent of ionization, have been determined by many groups using emission spectroscopy*[43,45,46]*, mass spectrometry*[44]*, and ion probe*[43]*. These parameters are very important in terms of understanding the PLD process and improving properties of laser deposited films.

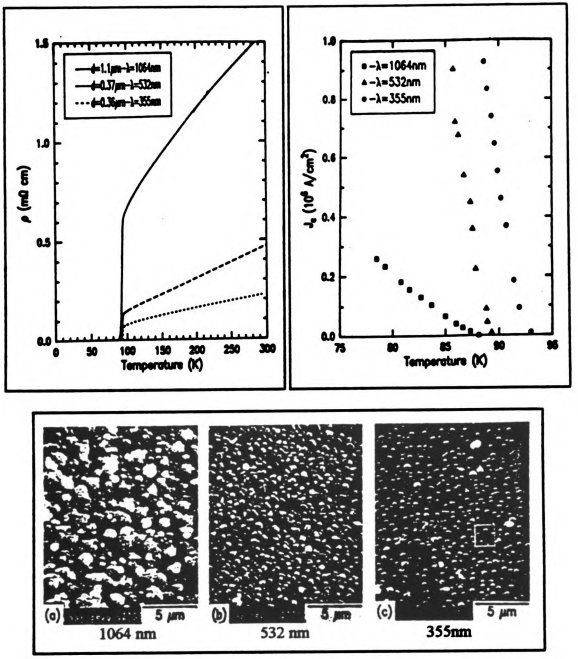

Figure 15. PLD of YBCO on $SrTiO_3$ substrate using fundamental (1064 nm), 2nd harmonic (532 nm) and 3rd harmonic (355 nm) of Nd:YAG laser with 3.5 J/cm^2 power density, 200 mTorr oxygen and 730 °C substrate temperature.
G. Koren et al., Laser Wavelength Dependent Properties of YBCO Thin Films Deposited by Laser Ablation*[16]*

Following characteristics of laser induced plume from high T_c superconductor target have been reported by several groups under typical deposition conditions, i.e. several Joule/cm^2 energy density and a few tens of nanoseconds pulse-width.

1. Angular distribution of vapor species consisted of two distinct components. One of the components is non-stoichiometric and has a cos θ angular distribution which is characteristic of evaporation; the other forward direction component is stoichiometric and has a $\cos^8\theta$ to $\cos^{12}\theta$ distribution*[15,16,42]*. The forward component increases with respect to the evaporation component as laser energy density increases*[42]*.
2. The major luminescent species in the plume are neutral and positively ionized atoms and dimers*[43]*.
3. By observing the change in the emission intensity of laser induced plume, the plume initially undergoes a one-dimensional expansion for about one spot diameter and then a three-dimensional expansion, in which the vapor density rapidly falling off and the excitation diminishing*[3,43]*.
4. The expansion velocities of the vapor species are about 10^4 m/s, and the corresponding particle energies are in the 25-50 eV range. Relative velocities for Cu and Y are found to confirm the $M^{-1/2}$ dependence predicted by vacuum free expansion model*[13,43,45,46]*.
5. Degree of ionization of the plume is estimated to be 1.4 - 4 % of ionized species from integrated ion signal and mass removal per pulse, assuming atomic species only and a cos θ angular distribution of the species respected to the target normal*[43]*. This 1.4 - 4 % ionization estimation is likely to be much underestimated because the sharp $\cos^8\theta$ to $\cos^{12}\theta$ distribution of the forward vapor component.
6. Plasma temperature is estimated, from expansion velocity and local thermodynamic equilibrium, to be in the range of 6400-13000 K*[43]*.

2.4.1.3 Problem with High-temperature Post-Annealing

Correct crystallinity and oxygen content is essential for good superconducting properties of the high T_c oxide superconductors. Low deposition rate in the order of angstrom per laser pulse, adequate substrate temperature about 600 to 750 °C, and sufficient oxygen partial pressure of a few hundred millitorrs are important criteria for obtaining in situ high T_c superconducting films. If these criteria are not satisfied, the as-deposited film will not be superconducting or will not have high T_c and high J_c (critical current density). Therefore, a high temperature, above 850 °C, post-annealing is necessary to restore the superconductivity. Care has to be taken to minimize the following undesirable properties associated with high temperature post-annealing process.

1. Chemical reaction with the substrate resulting in the formation of a non-superconducting interface layer*[5,85-87]*.
2. Loss of film stoichiometry after annealing due to surface evaporation and film-substrate interaction*[4,87,88]*. Barium and/or copper deficiency has been observed after post-annealing process in YBCO films.
3. Crack and/or roughing during thermal cycling resulting in low critical current densities*[6]*.

2.4.1.4 Methods to Improve Quality of Low-Temperature Grown Films

Lowering substrate temperature, yet preserving the superconducting properties, is the key in growing multi-layer component with different materials or to integrate high T_c superconducting thin film process into existing semiconductor processes. Several variations of the basic PLD process, i.e. plasma assisted PLD*[10,46]*, dc-biased PLD*[14]*, and atomic oxygen assisted PLD*[13]*, have been successfully able to lower the in situ

deposition temperature to as low as 400 °C*[10]*, Figure 16. Reduction of the deposition temperature is made possible by creating reactive oxygen species such as atomic oxygen, oxygen ion beam, or oxygen plasma and/or by enhancing mobility of surface atoms with dc-bias or ion bombardment.

2.4.1.5 Problem with Surface Particles

One unique feature of PLD deposited film is the presence of surface particles on otherwise smooth film surface. The formation of these surface particles has been attributed to sub-surface micro explosion caused by overheating of the sub-surface layer during laser-target interaction*[3,89,90]*. Koren et al. found that particles are fewer and smaller as the wavelength of the laser decrease due to higher absorption of laser energy by the plasma plume and higher degree of fragmentation in the vapor phase*[16]*, Figure 15.

For a given laser wavelength, the surface particle problem can be minimized by increasing the absorption coefficient and thermal conductivity of the target, which reduce the sub-surface overheating, and by improving the strength of the target, which increases the resistance to explosion*[91]*. Increased density of the bulk target by silver addition, laser surface melting, melt process, or hot isostatic pressing (HIP) is expected to reduce the surface particle formation. Recently, Eidelloth et al. reported a method to remove surface particles by chemical polishing with diluted HF solution without degrading the superconducting properties of the films*[92]*.

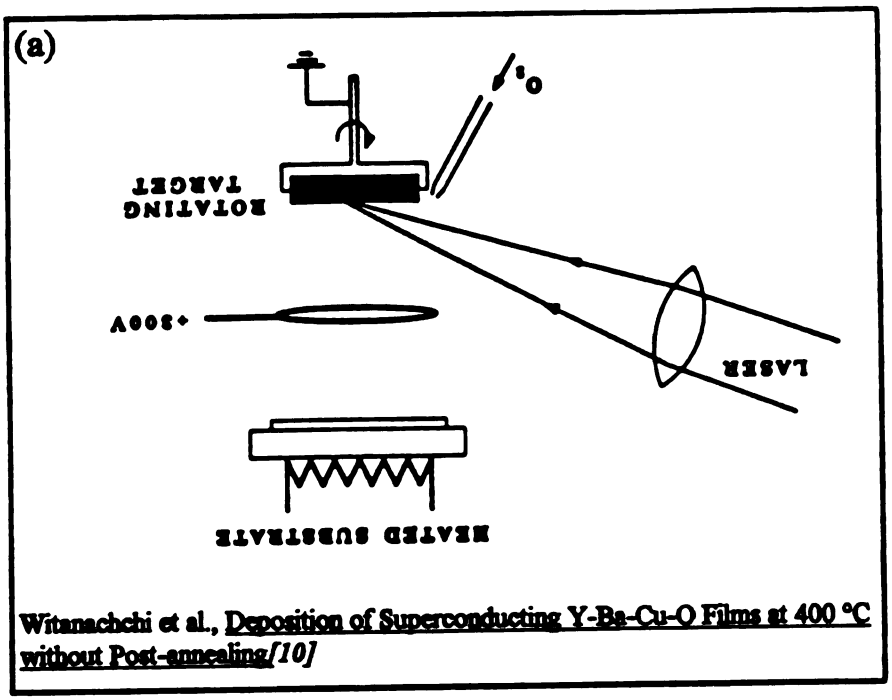

Witanachchi et al., Deposition of Superconducting Y-Ba-Cu-O Films at 400 °C without Post-annealing*[10]*

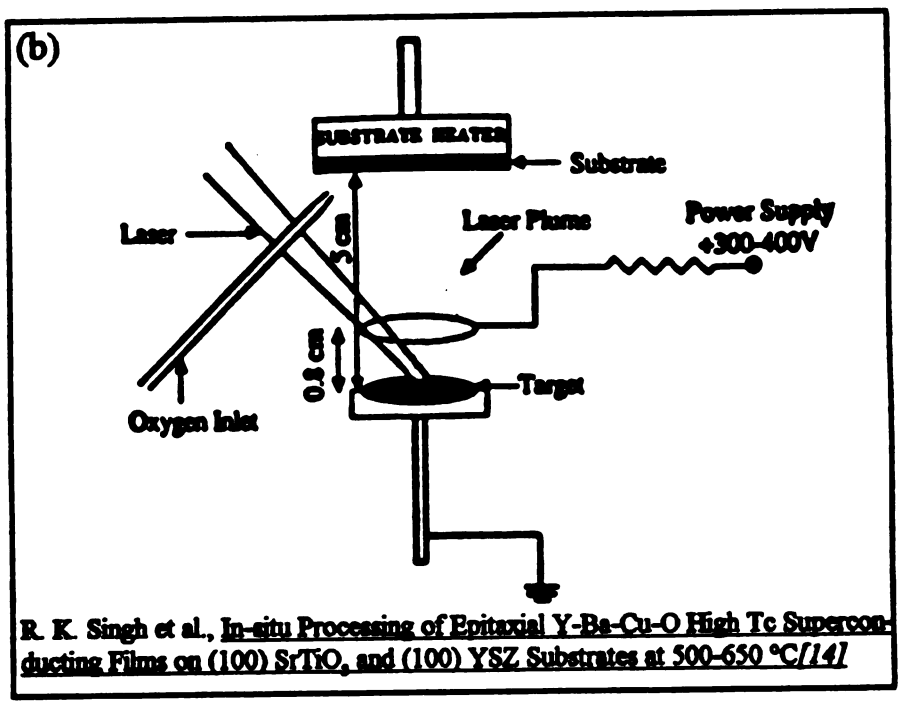

R. K. Singh et al., In-situ Processing of Epitaxial Y-Ba-Cu-O High Tc Superconducting Films on (100) $SrTiO_3$ and (100) YSZ Substrates at 500-650 °C*[14]*

Figure 16. (a) Plasma-assisted PLD setup with 10^{-4} Torr oxygen pressure during deposition, and (b) Dc-biased PLD setup with 200 mTorr oxygen pressure during deposition

2.4.2 Pulsed Laser Ablation Using Millisecond Nd:YAG Laser (ms-PLD)

Although high quality YBCO thin films can be obtained by using nanosecond UV lasers, the deposition rate is very low, typically a few angstroms per laser pulse, and the deposited area coverage is very small, a few mm in width, due to the narrow angular distributions as sharp as $\cos^8\theta$ to $\cos^{12}\theta$*[15,16,42]*. On the other hand, high deposition rates up to 100 nm/s*[15]* and a large uniform deposition coverage, due to a broader $\cos\theta$ angular distribution of the evaporated species can be obtained by using millisecond pulsed lasers. These unique properties make millisecond PLD a practical process to be used to produce continuous coating of tapes.

2.4.3 Nd:YAG Solid State Laser vs. Excimer Gas Laser

Laser stands for ***light amplification by stimulated emission of radiation*** that is produced by placing a fluorescing material in a optical cavity typically consisted of two parallel mirrors facing each other*[93]*, Figure 17. Usually both mirrors are coated to increase reflectance for the wave-length of the laser. The rear mirror is almost 100% reflecting and the front mirror, i.e. the output mirror, is partially transmitting with reflectance $R < 1$ to extract laser output.

Usually, the fluorescing medium is excited to higher energy state by optical pumping for solid state laser or by electric arc discharge, electric glow discharge, or microwave excitation for gas lasers.

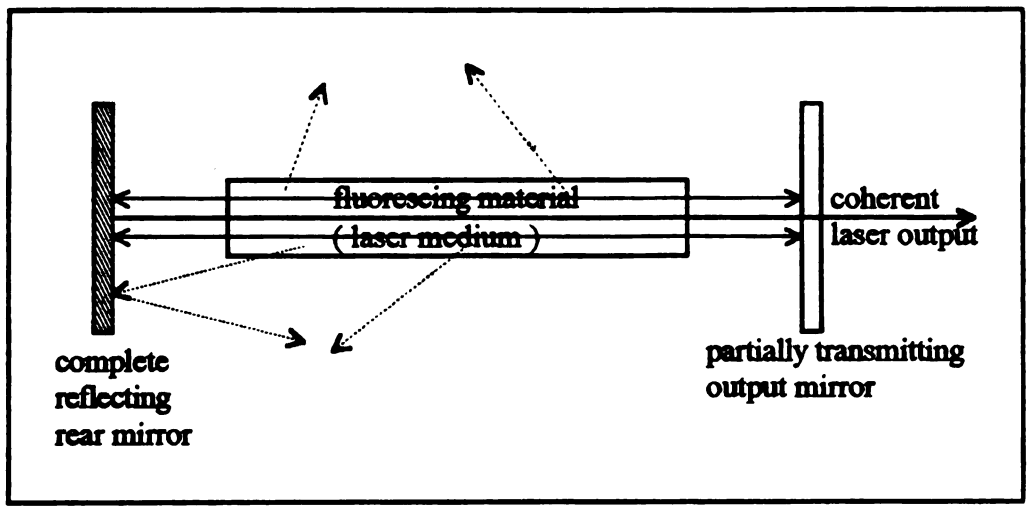

Figure 17. Basic laser cavity

There are basically two ways by which atoms at excited states can radiate energy*[94]*. One is the spontaneous emission process in which excited atoms change to lower energy state randomly. Fluorescent light produced this way is not directional nor coherent, i.e. consists of various frequencies and phases. The other process involves stimulating the excited atoms by an external electromagnetic field or light (in the case of laser) of the proper frequency. This is called ***stimulated emission***. This process produces coherent light, of the same frequency and direction of propagation as the stimulating source. Since the stimulated emission induces more emission, the result is ***amplification*** of the original light signal.

Figure 18 (a) shows the energy diagram of a three-level optically pumped laser medium, e.g. triply ionized chromium in a ruby laser. The actual laser action involves transitions from level 2 to level 1 that produce photons of energy $h\nu$. The atoms of the medium strongly absorb photon energy, $h\nu_p$, of the pump light and excite to the energy band at third level. However, this level is never populated, i.e. the fraction of atoms in level 3 (n_3) is approximately zero, due to nearly instantaneous non-radiative transition from this level to level 2. The third level is required to achieve a necessary condition for amplification called ***population inversion*** that the fraction of atoms in lever 2, n_2, is

greater than the fraction of atom in level 1, n_1. Defining $n = n_2 - n_1$, at ground state $n_2 = n_3 = 0$, $n_1 = 1$ and $n = -1$; the population inversion is attained when $n > 0$.

Higher efficiency can be obtained with a four-level laser that has the ground level is far below the lower laser level or the level 1, Figure 18 (b). In this case, the lower laser level is unpopulated, i.e. $n_1 = 0$, thus, any population in level 2 gives rise to an population inversion. Therefore, it is not necessary to pump a four-level laser from $n = -1$ to $n = 0$ before achieving gain. Moreover, the four-level laser medium never exhibits absorption of the laser light itself because $n_1 = 0$.

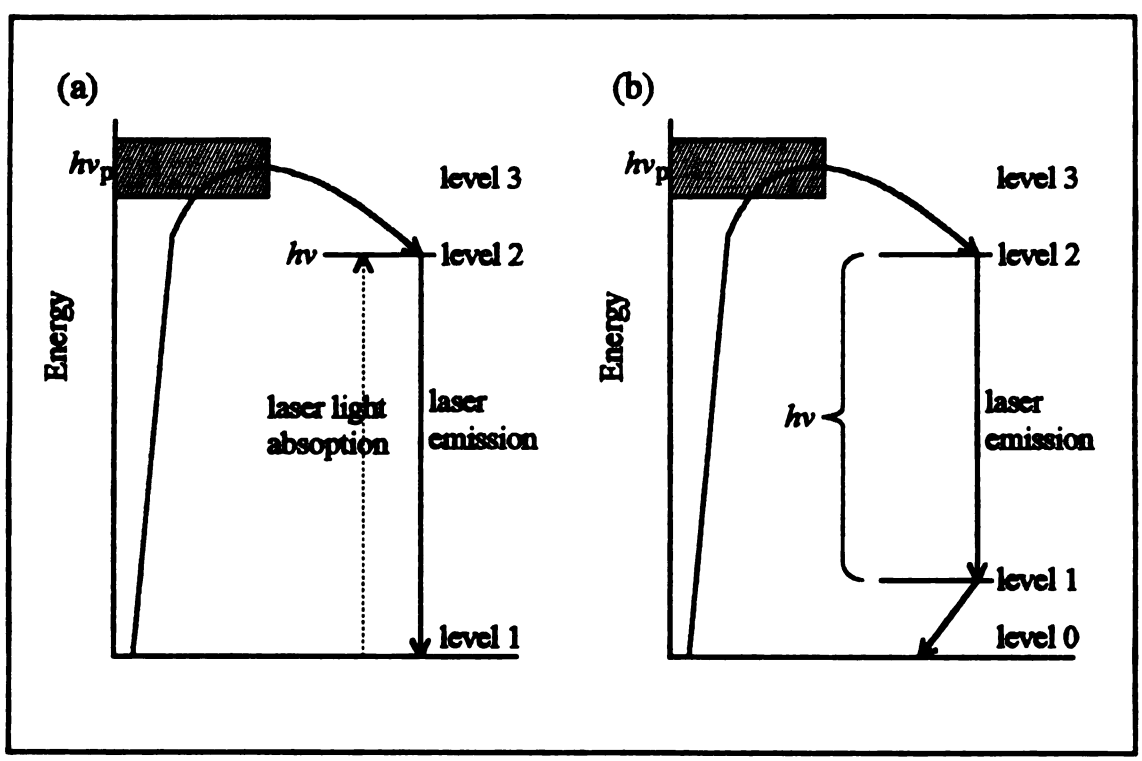

Figure 18. Energy diagrams of (a) three-level laser and (b) four-level laser

If the optical cavity is configured correctly and the fluorescent material is homogeneous, multiple reflections are possible in the direction defined by the two cavity mirrors. Light amplification occurs if the gain due to stimulated emission is greater than

the absorption loss and the output through front mirror. When this condition occurs the laser is said to ***oscillate*** or ***lase*** with highly directional and coherent light.

2.4.3.1 Nd:YAG Solid State Laser

The Nd:YAG laser was discovered in 1961, and it is now the standard industrial solid state laser. The active medium of Nd:YAG laser is triply ionized neodymium atoms, a typical four-level laser medium, which replaces some of the yttrium atoms in the host yttrium aluminum garnet, $Y_3Al_5O_{12}$ or YAG. Major components of a Nd:YAG laser head are shown in Figure 19, which consist of a dual-elliptical pump cavity, adjustable front and rear mirrors and the optional Q-switch and nonlinear-crystal harmonic generator. The laser rod and flash lamps are enclosed in fused quartz flow-tubes for direct water cooling.

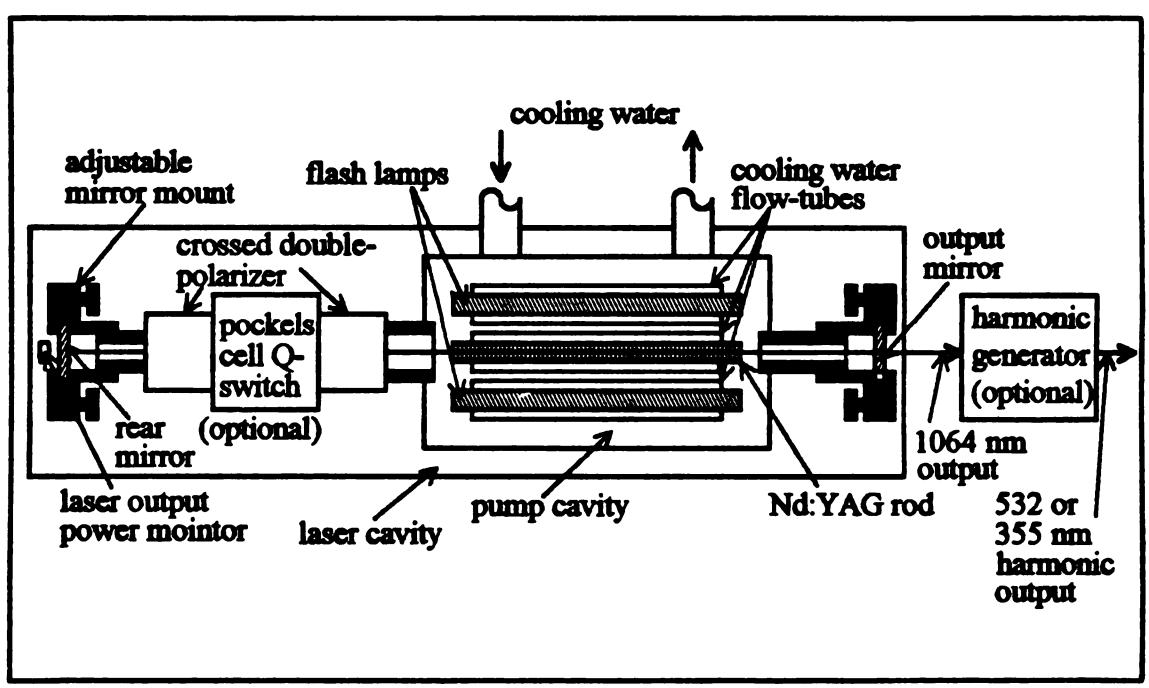

Figure 19. Typical Nd:YAG laser cavity

In the long pulse mode, i.e. without Q-switch, the pulse-width is typically a few hundred microseconds to a few milliseconds which corresponds to the fluorescent life time of the laser medium and the duration of the excitation flash-light, respectively*[95]*. On the other hand, the Q-switched pulse-width is typically ten to a few tens of nanoseconds which is closely related to the cavity life time determined by the distance between mirrors and the reflectance of the output mirror*[93]*.

2.4.3.2 Excimer Gas Laser

The term ***excimer*** stands for excited dimer, a molecule consisted of two identical atoms and exists only in an excited state, such as He_2 and Xe_2. Nowadays, excimer is used to describe any diatomic molecule that exists only in excited state, such as HgBr, ArF, KrF, XeCl and other rare-gas halide molecules. The fact that these molecules exist in excited state make them good candidates as laser media because they decomposes into unbonded atoms after transition from excited state and automatically de-populate the lower level of transition.

Excimer lasers were discovered in mid-1970s, and very soon they became commercially available because existing transversely excited atmospheric-pressure carbon dioxide laser hardware works reasonably well with the newly developed laser media. The major problem involved in this conversion is the halogen corrosion which has been solved with halogen resistant internal coating*[96]*.

The laser medium is a mixture of 90 - 99% of helium or neon buffer gas to facilitate energy transfer, 1 - 9% of Ar, Kr or Xe rare gas to form excimer molecules, and 0.1 - 0.2% of F_2, Br_2, Cl_2, HCl, HBr or HF as halogen donor. The life time, typically in the order of 10^6 shots or a few hours at 200 shots/s, of excimer gas mixture is very short. This resulted in the problems of high operation cost, approximate $50 per charge of gas mixture, and handling of hazards discharged gas*[97]*. The excimer lasers are still

relatively new, and mainly used in research laboratory. However, with the recent development of large industrial excimer lasers in kilowatt range, the operation cost per joule of laser energy is expected to be lower*[98]*.

Excimer lasers used for PLD process typically have a wave length of 193 nm (ArF), 248 nm (KrF) or 308 nm (XeCl), a pulse-width of ten to a few tens nanoseconds, a pulse-energy of a few hundreds milli-joules.

In this study, a millisecond pulsed Nd:YAG laser with 1064 nm wavelength was used. The advantages of using an Nd:YAG laser over an excimer laser are as follows: First, high power Nd:YAG lasers can be easily operated at high repetition rate with high pulse-energy; thus a larger deposition rate can be expected. Second, it has a wide range of possible output wavelength by harmonic generation, namely near-infrared 1064 nm fundamental, green visible 532 nm 2nd harmonic, and ultraviolet 355 nm 3rd harmonic. Third, there are choices of a wide range of operation modes such as high repetition rate mode, long pulse (ms) mode and Q-switched (ns) mode. Finally, due to its solid state design, it does not have complicated moving components, such as high vacuum pumps, and, there is no need for expensive and corrosive gases.

3. EX

3.1 T

leas

and

perf

was

the

due

3.1

m

ch

sc

g

3

i

s

3. EXPERIMENTAL PROCEDURE

3.1 Target and Bulk High T_c Superconductor Preparation

Both BSCCO and YBCO superconductors were prepared from high purity, at least 99.9% purity, single-metal oxides or carbonates. Initial grinding before calcination and intermediate grindings between multiple calcinations and final sintering were performed with a pestle and mortar. After initial crushing of large particles, methanol was added to form a slurry to increase the grinding efficiency. Methanol was chosen as the grinding medium to prevent possible degradation of the superconducting compound due to moisture pickup*[99,100]*.

3.1.1 Pb-Doped BSCCO 2223 Superconductor

Starting materials of Bi_2O_3, PbO, $SrCO_3$, $CaCO_3$, and CuO were weighed and mixed to have Bi:Pb:Sr:Ca:Cu cation ratio of 1.5:0.5:2:2:3. This starting composition is chosen from the reported data for maximizing the critical temperature considering that some lead loss may occur during laser calcination*[38,40]*. This powder was thoroughly ground with a pestle and mortar to ensure through mixing.

3.1.1.1 Laser and Conventional Calcination of Pb-doped BSCCO

The mixed fine powder was placed in a specially designed slow rotating pan and irradiated with a defocused pulsed Nd:YAG laser beam at two different power levels of 50 and 90 Watts, Figure 20.

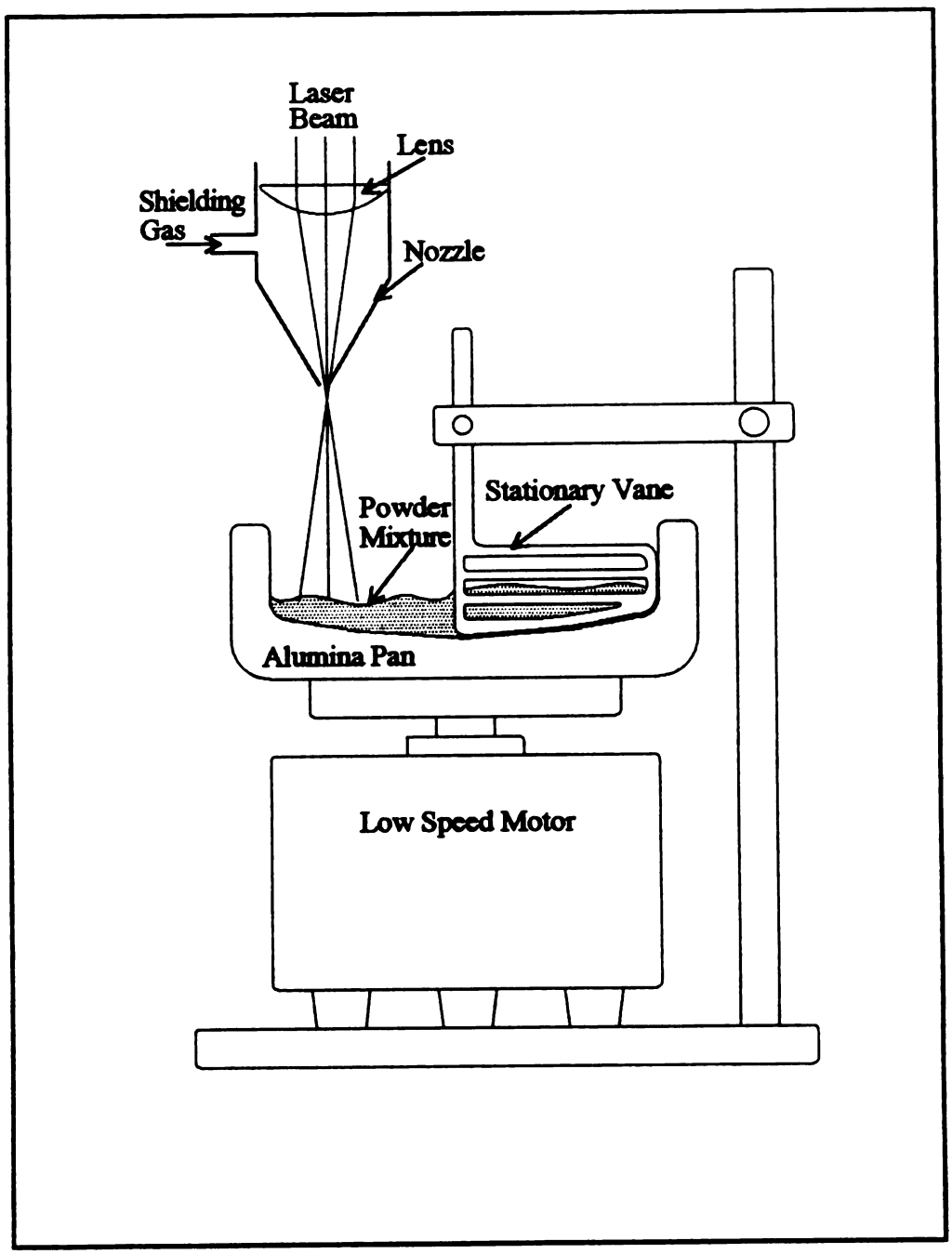

Figure 20. Laser calcination apparatus

During laser irradiation, the powder was constantly stirred by a stationary vane attached to the rotating pan. Periodically, calcining powder was reground to ensure uniform laser-powder interaction. The average linear speed of the rotating pan with respect to laser beam was about 2.5 cm/s. A 400 W Nd:YAG pulse laser with a pulse rate of 100 pulses-per-second and a pulse width of 2.2 ms was used during all the experiments. The laser beam was focused to a 4 mm diameter spot. Thus, the pulse-energy density was 1 or 1.8 J/cm^2, and the peak-power density was about 450 or 800 W/cm^2, Table 2.

For comparison, an identical batch of powder mixture was also calcined conventionally in a furnace set at 830 °C for 7 hours.

Table 2. Calcining conditions of Pb doped BSCCO

	laser power (W)	pulse-energy density (J/cm^2)	peak-power density (W/cm^2)	time (hr)
sample A	90	1.8	810	0.5
sample B	50	1	450	1.5
sample C	Conventionally calcined at 830 °C for 7 hours			

3.1.1.2 Sintering of Pb-doped BSCCO

The laser calcined and conventionally calcined powders were pelletized with a 0.5" diameter mold and a hydraulic press. One drop of amyl-acetate ($CH_3COOC_5H_{11}$) per gram of powder mixture was used as a binder for better green strength. These pellets were sintered at 865 °C in air for different durations of 15, 50, 85, 100, and 240 hours, then furnace cooled to room temperature at a rate about 100 °C/h.

3.1.2 YBCO and Ag-Doped YBCO Superconductors

YBCO targets with stoichiometric composition were prepared from high purity Y_2O_3, $BaCO_3$, and CuO using conventional solid state sintering process. Finely ground powder mixture was firmly hand packed in a alumina pan for double calcination at 930 °C for 10 hours. It is important to pack the powder firmly because the calcination and formation of YBCO will be greatly accelerated.

The double-calcined sample was carefully ground and pelletized with molds of different geometry and a hydraulic press. One drop of amyl-acetate per gram of powder mixture was used as a binder for better green strength. These pellets were sintered at 950 °C for 36 hours. Only $YBa_2Cu_3O_x$ phase was detected in final sintered YBCO target by using a x-ray diffraction method.

Silver doped YBCO targets were prepared by crushing YBCO pellets and adding 16 wt% or 24.5 wt% of 99.9% purity Ag_20. Well-mixed powder was pelletized and sintered at 850 °C for 12 hours plus 930 °C for 36 hours plus 960 °C for 48 hours. Only very small amount of impurity phase was detected with x-ray diffraction method.

3.2 Substrate Preparation and Silver Thin Film Deposition

Substrates for ion-beam assisted millisecond PLD were metallographically polished polycrystalline silver (99.9% pure), commercial grade polycrystalline alumina substrate with 5 μm silver coating, optically polished (001) yttrium stabilized zirconia (YSZ) and (001) YSZ with 0.2 μm silver buffer layer. Multi-layer Ag-doped YBCO / Ag tapes were started with a 5 to 50 μm layer of silver on commercial grade fused silica slides.

Silver buffer layers of the ceramic substrates and silver layers of the multi-layered tapes were prepared by conventional vacuum thermal evaporation (VTE). A tungsten

wire basket was used as heat source to evaporate silver chips of 99.9% purity onto room temperature substrate. The base pressure of the evaporator was $1x10^{-5}$ torr.

3.3 Millisecond Pulsed Laser Deposition

A RAYTHEON SS-500 SERIES 400 Watts pulsed Nd:YAG laser was used. This laser is operated at the fundamental line of the Nd:YAG crystal, i.e. wavelength of 1.064 μm, and has a maximum pulse-energy of 50 Joules. The pulse-rate is continuously variable from 1 to 200 pulses per second. The pulse-length, variable from 250 μs to 7.2 ms, and pulse-shape, most often square wave or triangular wave, can be selected by reconfiguration of the pulse-forming-network of the pumping flash lamp. The square wave pulses have a minimum pulse-length of 1.2 ms, while the triangular wave pulses have a maximum pulse-length of 1.2 ms.

An adjustable beam expander is used to expand the laser beam size to about 10 mm diameter. This expanded beam is bent downward in the focusing head equipped with a coaxial monocular microscope that is aligned with the laser beam and uses the laser focusing lens as objective lens. This convenient microscope can be used to aim the target and to in situ observe the laser irradiated target. 4" or 8" Plano-convex lens made of UV-grade fused silica is used to focus laser beam onto the target. Figure 21 is a sketch of the laser beam delivery system.

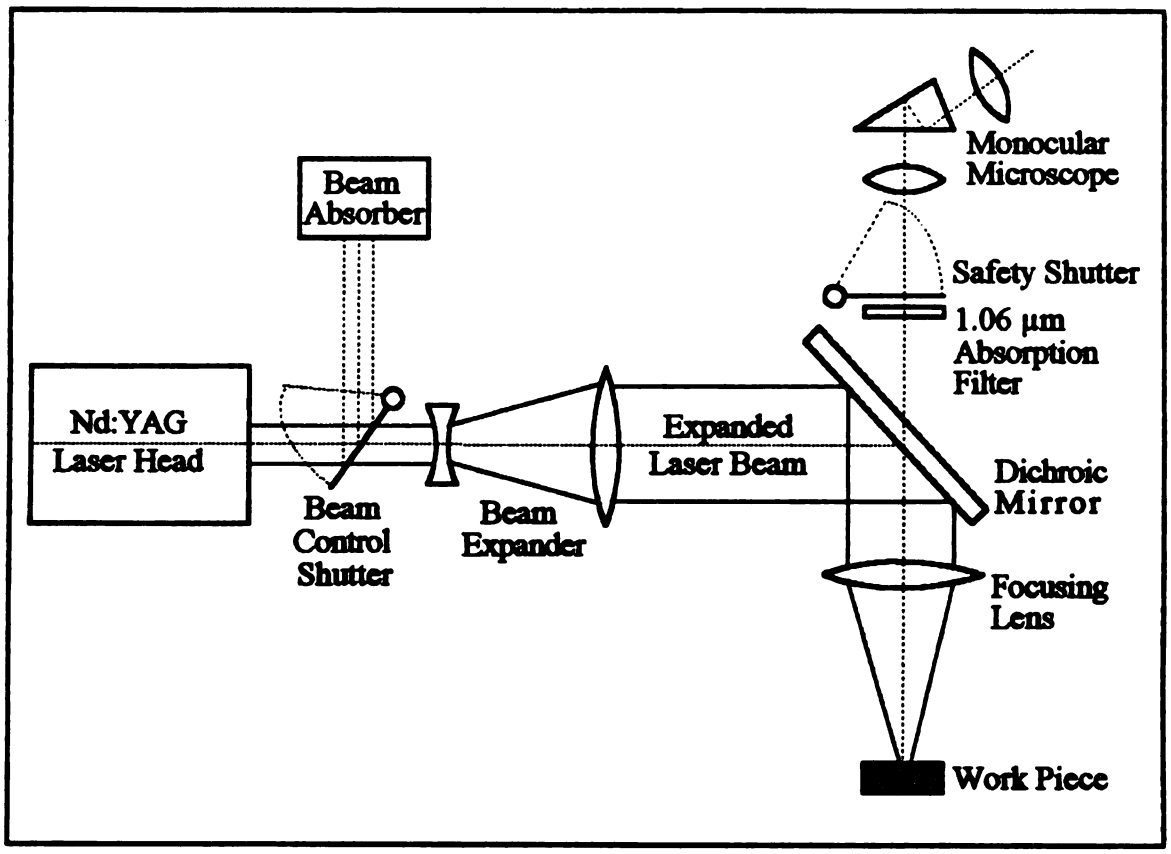

Figure 21. Laser beam delivery system

3.3.1 Plasma assisted PLD Apparatus

3.3.1.1 Plasma Assisted PLD Chamber

The design and construction of the PLD vacuum apparatus were a major undertaking of this research project. The preliminary results of this research were gathered with a vacuum chamber that is converted from a section of an old Hitachi transmission electron microscope, Figure 22.

This chamber has an internal size of 4" diameter by 4" high, one 3" diameter fused silica optical window and three 3" diameter accessory ports on the side. Normal O-rings are used through out as vacuum seals.

A half inch brass plate was machined to cover one of the accessory port to facilitate soldering or brazing of gas inlet and copper tube for electric feed-through. Oxygen is introduced into the chamber by a 1/8" copper tubing through the brass plate with a vacuum seal formed by soldering. Oxygen flow into the chamber is controlled by a needle valve and monitored with a flow meter. The electric feed-through was made by embedding six copper wires in bakelite rod with two O-ring groves.

A 3/4" aluminum plate was made to seal the bottom of the chamber and to mount PLD parts. An 1.5" diameter opening, on the top of the chamber, with an O-ring grove is adopted to an optical window to deliver high energy laser pulses.

3.3.1.2 Target and Target holder

A rotation target holder is driven directly by a dc motor inside the chamber. A specially designed four-piece mold was used to produce bulk YBCO target rings, Figure 23. Target rings instead of more conventional target disks were used to maximize target surface utilization and to prevent uneven etch of the target.

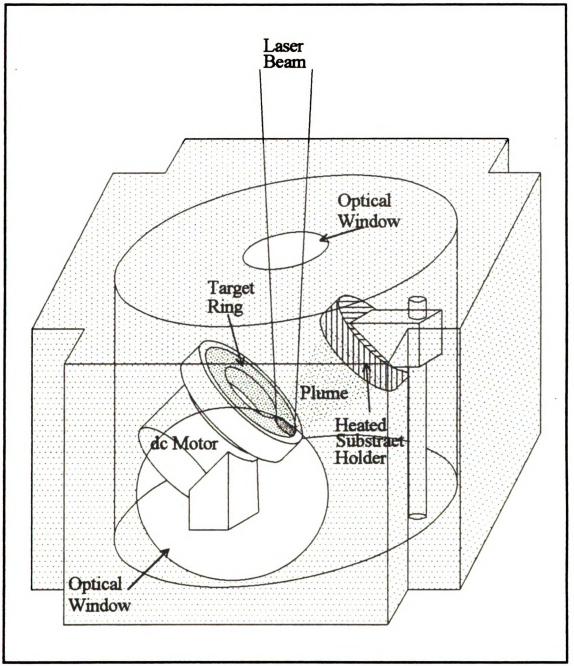

Figure 22. PLD chamber used for preliminary study

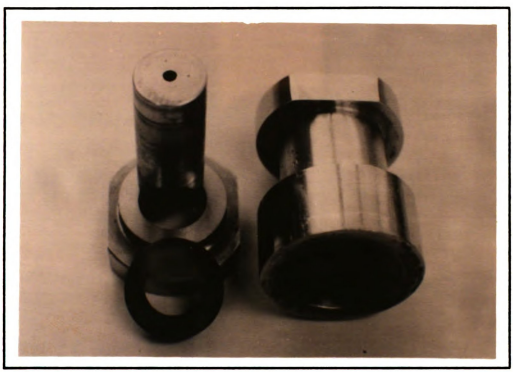

Figure 23. Specially designed mold, and YBCO target ring produced by using this mold

The uneven etching of the target will result in misdirected plume, i.e. the evaporated species, because laser induced plume always ejected perpendicularly to the target surface. This concern is especially important for millisecond-PLD process due to much higher target material removing rate compared to nanosecond-PLD.

3.3.1.3 Heated Substrate Holder

Substrate holder was made of stainless steel to hold the substrate of 20 mm x 10 mm size. The substrate heater was placed in the substrate holder directly behind the substrate. This heater was made by winding Fe-Cr-Al alloy heater wire on a grooved alumina block to get as high as 650 °C substrate temperature.

3.3.1.4 Oxygen Plasma Generation

Intense oxygen plasma was created by applying an oscillating dc high voltage to the system. The high voltage power is generated by using a step-down transformer that converts 110 V 60 Hz ac power into 6 V or 12 V output up to 10 A. This output is converted into 120 Hz oscillating dc current by a full-wave diode-bridge. A automobile ignition coil is then used to step-up the voltage to approximately 1 KV. Because this design exceeds the original design capability of the high voltage coil, it is cooled by a copper water jacket.

The initial design consisted of a silver wire-loop anode, and the cathode consisted of the target and substrate holders together, Figure 24 (a). Figure 25 shows pictures of the deposition apparatus during a deposition process.

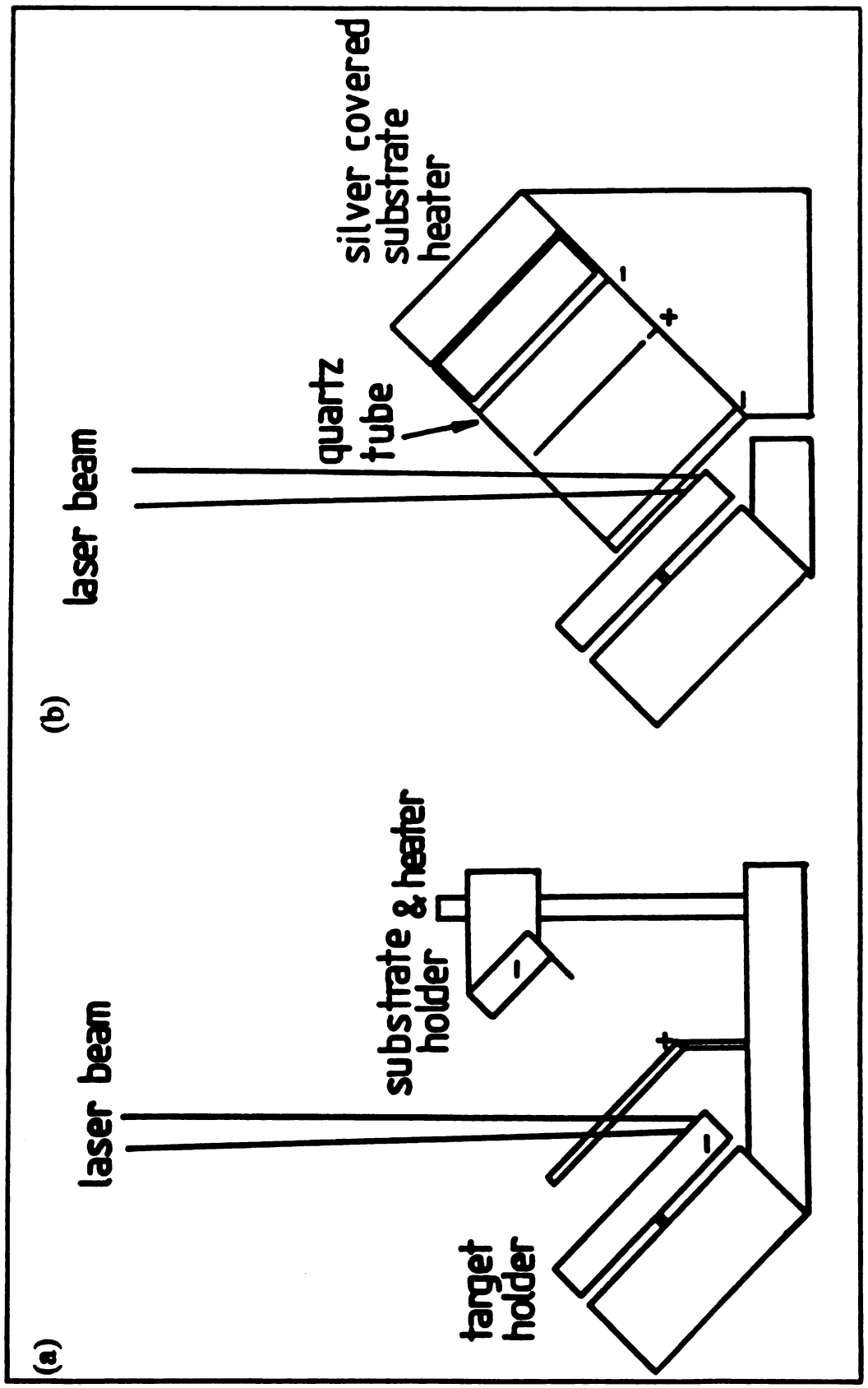

Figure 24. Plasma assisted PLD setup (a) with a plasma ring and (b) with a plasma tube

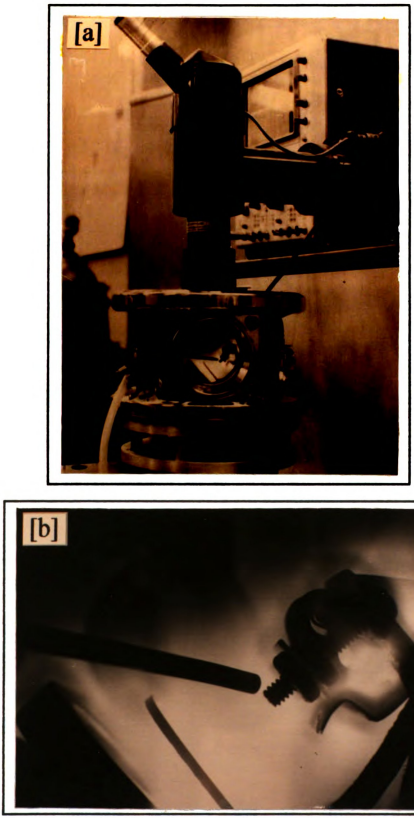

Figure 25. Plasma assisted PLD chamber (a) with the laser head and (b) close-up view

of the

plasma

to elec

3.3.2 I

two-s

for n

total

dilu

the

Later, a fused silica tube with three silver wire-loop electrodes was used instead of the original single wire-loop anode, Figure 24 (b). This is to confine the oxygen plasma to the area between the target and substrate, and to reduce the target heating due to electron bombardment.

3.3.2 Plasma Assisted Millisecond PLD Process (PPLD)

Table 3 lists the important processing parameters. The chamber is pumped with a two-stage mechanical pump to get a base of about 20 mtorr. The vacuum requirement for millisecond PLD is not as strict as for the conventional nanosecond PLD because the total processing time is much shorter due to orders of magnitude higher deposition rate.

The chamber was flushed with pure oxygen several times after initial pumping to dilute residual air. During deposition process a stream of oxygen flowed directly toward the substrate, and a 250 mtorr of oxygen pressure was maintained.

Table 3. Important Processing Parameters for plasma assisted PLD

PROCESS PARAMETERS	
Wavelength	1064 nm
Pulse Width	2.2 ms
Repetition Rate	2 pulses / s
Spot Size on Target	15 mm^2 elliptical spot
Pulse Energy Density	40 J / cm^2
Peak Power Density	18.18 KW / cm^2
Substrate Temperature	500 °C
Target to Substrate Distance	3.5 cm
Chamber Pressure	250 mtorr of oxygen
Target Material	Conventional sintered YBCO ring with near stoichiometry composition
Post-Annealing	500,600,850 and 940 °C in air or oxygen

Laser pulses used had 6 joules per pulse pulse-energy, 2.2 ms pulse-width, and the repetition rate was 2 pulses per second (pps). These laser pulses were focused to a 15 mm^2 elliptical spot on the target. This spot size was chosen to cover the entire width of the ring to prevent uneven erosion of the target, Figure 26. However, the maximum peak power density was restricted below 0.02 MW/cm^2. The resulting pulse-energy density and peak power density were 40 J/cm^2 and 18.18 KW/cm^2, respectively.

Figure 26. A YBCO target ring after deposition process

3.3.3 lo

overhe

The g

flexib

mech

mach

3.3.3

6" u

five-

redu

cus

All

on

rig

top

3.3.3 Ion-Beam Assisted PLD Apparatus

Due to the 0.02 MW/cm^2 maximum peak power limitation, and the target overheating problem, designing of a flexible material-processing chamber was initiated. The goal was to design an apparatus that could solve the present problems and was flexible enough to be adopted to solve future problems.

To minimize the cost and development time, standard high vacuum and mechanical parts were used whenever probable, and all other parts were modified or machined right in the laboratory.

3.3.3.1 Ion-Beam Assisted PLD Chamber

The chamber body is a standard stainless steel high vacuum five-way cross with 6" tube diameter and 8" standard conflat flanges*. The distance from the center of the five-way cross to each of the flange is approximately 6.5", Figure 27.

The top port and the port on the right are covered with standard 8" to 4 1/2" reducing flanges that accept standard permanently sealed optical view ports or customized adapters for standard 3" diameter and 1/8" thickness optical window blanks. All other three ports are covered with standard 8" blank flanges.

Laser beam is introduced into the chamber through the top port and a small hole on the stainless steel lining. The lining is a piece of thin sheet that covers left through right tube sections to catch debris from ms-PLD process and to limit debris entering the top, front and rear sections of the chamber.

* All high vacuum components are obtained from the Kurt J. Lesker Company, Clairton PA.

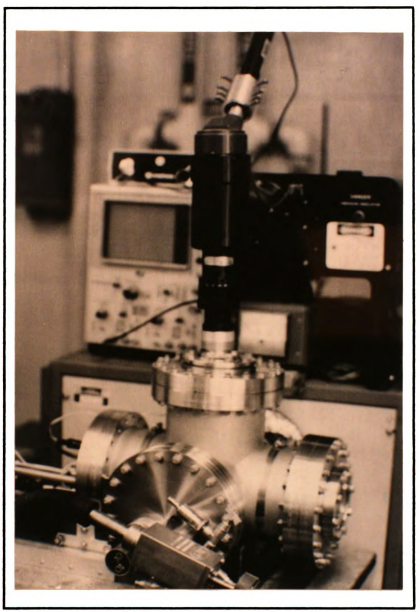

Figure 27. The ion-beam assisted PLD chamber and the laser head

conduc

bonnet

steel t

connec

connec

bargra

is a sl

substr

3.3.3.

A len

entra

on a

to ob

mov

lens

lens

slit,

thro

con

"qu

pla

an

The mechanical pump is connected to the chamber through a high gas conductance brass right-angle high vacuum shutoff valve, with 1 1/2" bore, Viton O-ring bonnet and seat seals and bellows shaft seal. A brass needle venting valve and a stainless steel thermocouple gauge tube are located close to the chamber on the 2" brass tube connecting the front port of the chamber and shutoff valve. The thermocouple gauge is connected to a JC CONTROLS model 100TC controller with one set point and a bargraph display of vacuum from 1000 to 1 mtorr.

The right port with an optical window is used for process observation. Figure 28 is a sketch of the chamber arrangement, which shows the penning ion gun, the heated substrate holder and the x-y target manipulator, viewed from the right view port.

3.3.3.2 Spatially Resolved Emission Spectrum Analyzer

Figure 29 is a sketch of the spatially resolved emission spectrum analysis setup. A lens is used to image the laser induced plume through the observation window onto the entrance slit of a optical multi-channel analyzer (OMA). This imaging lens is mounted on a standard lens holder that permits easy change of lenses with different focal lengths to obtain different field of view and spatial resolution. A precision linear slide is used to move the lens mount for fine focus. A cube beam splitter is located between the imaging lens and the OMA slit to send approximately half of the intensity upward to the single lens reflex (SLR) camera. The optical path distances from the imaging lens to the OMA slit, and the camera film plane are set to be the same; therefore the plume can be focused through the camera view finder and recorded on the film for further analysis. All optical components except the camera are made of UV grade fused silica (very often called "quartz") to preserve the ultraviolet spectrum. The emission spectrum analyzer setup is placed on a stable cart with adjustable high, and the optical components are mounted on an optical rail for precision alignment, Figure 30.

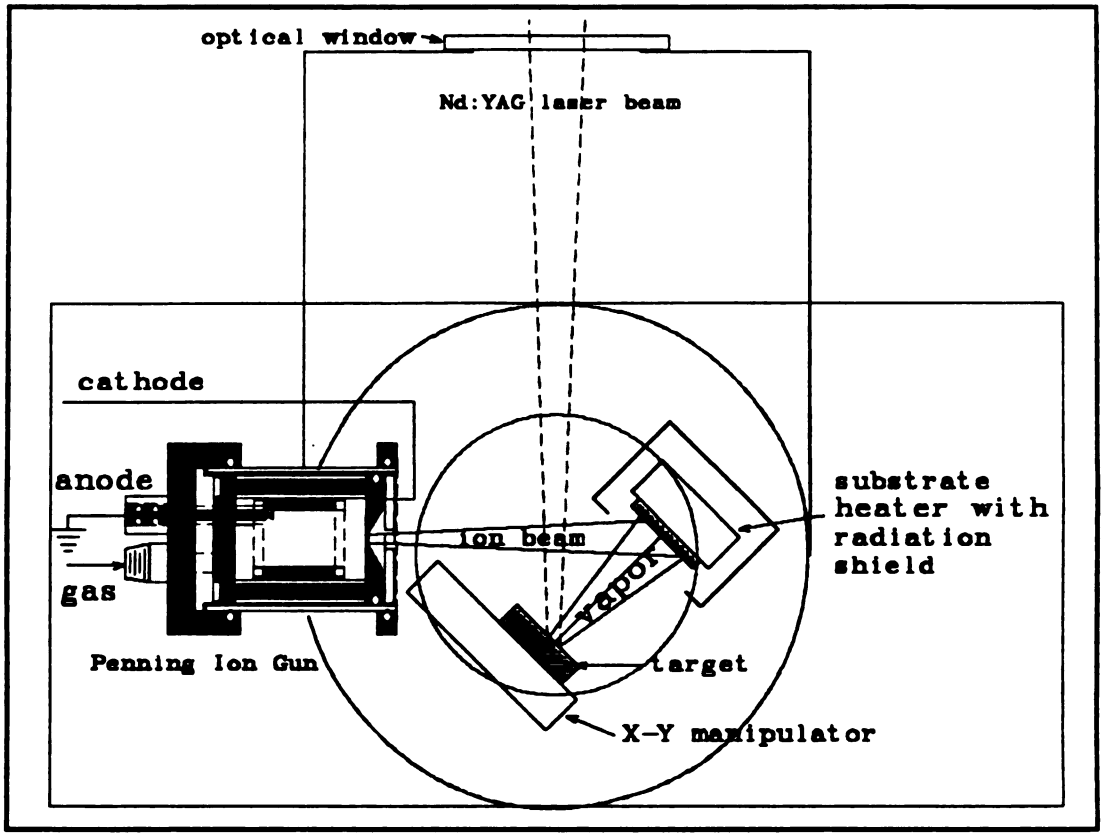

Figure 28. The ion-beam assisted PLD chamber viewed from the right view port

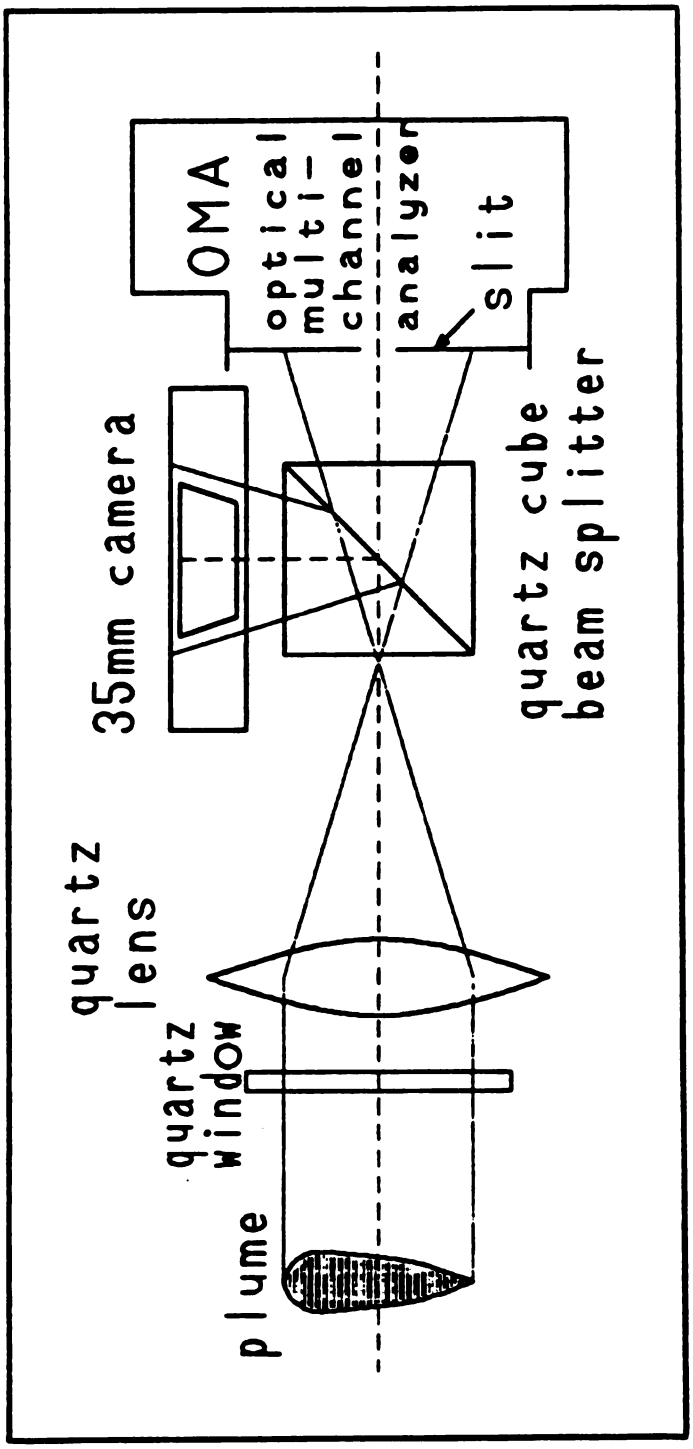

Figure 29. Spatially resolved emission spectrum analysis setup

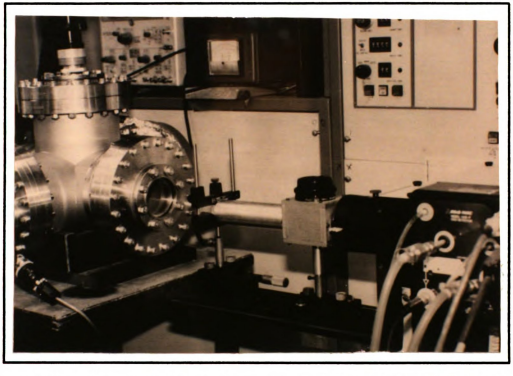

Figure 30. Spatially resolved emission spectrum analysis setup with PLD chamber

3.3.3.3 (

1.5" dia

the gun

seals a

the gun

and th

in the

and t

feed

carry

a l

need

com

3.3.3.3 Oxygen Ion Gun

A sketch of the homemade penning ion gun is shown in Figure 31. A section of a 1.5" diameter fused silica tube serves as the body of the ion gun. Major components of the gun are made of brass. Teflon and alumina are used as electrical insulators. Vacuum seals are formed using heat-resistant silicone O-rings. When high voltage is applied to the gun under proper oxygen pressure, glow discharge occurs between the cathode plates and the cylindrical anode. The oxygen ion beam is extracted from the gun through a hole in the front cathode plate, Figure 32.

The ion gun is mounted inside the front port with the high voltage feed through and the oxygen gas feed through mounted on the flange, Figure 33. The high voltage feed through with 2 3/4" conflat flange has four copper conductors that are capable of carrying 75 A at 5 KV. The oxygen gas feed through has one 1/4" stainless steel tube and a 1 1/3" conflat flange. A precision needle valve is used to control the gas flow. The needle valve and the ion gun are connected to the feed through using standard brass compression fittings.

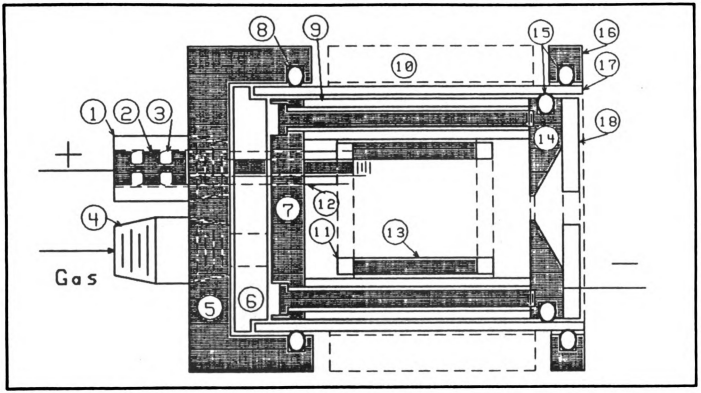

1,4 teflon tube
2 brass electric feed-through
3,8,15 O-ring
6,11,18 teflon insulator
5 brass end cap
9,12 alumina insulator
7,14 cathode
10 optional magnet
13 anode
16 brass protective ring
17 fused-silica ion gun body

Figure 31. Penning ion gun

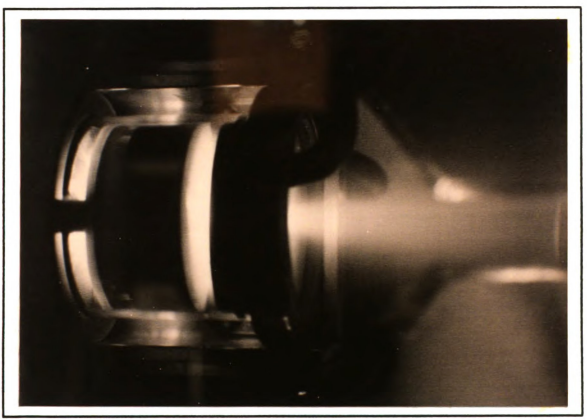

Figure 32. Penning Ion gun at work

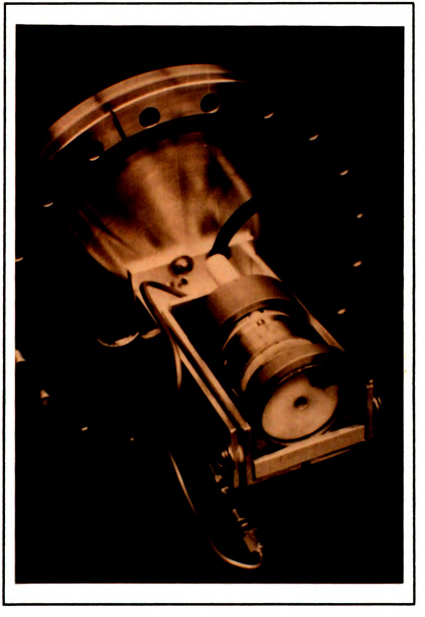

Figure 33. Penning ion gun mounted on the front port flange

3.3.3.4 High Frequency High Voltage Power Supply

A high frequency high voltage is chosen to power the oxygen ion gun to increase the safety of the operation. This is due to the reason that high frequency current is confined to a very thin surface layer of a conductor.

The high frequency high voltage power supply is based on a TCL*A* PLUS high frequency high voltage supply parts kit furnished by INFORMATION UNLIMITED*. Figure 34 is the circuit diagram of the modified high voltage power supply.

The NPN transistor Q1 is set to oscillate by the feed-back winding of the high voltage transformer, and the oscillation frequency is set to be 10 to 20 KHz. Output voltage is controlled by a variable resistor (VR1) through a control-transistor Q3 and a power transistor Q2 that limits the current through the Q1 and the primary winding of high voltage transformer. Two high power 2N3055 transistors and one TIP31 power transistor are used to replace the original power transistors Q1 and Q2, and the control-transistor Q3 to increase the reliability and output of the circuit**. Performance of the circuit is further improved by fan cooling the transistors. The modified circuit provides approximately 40 Watts to the primary winding. This gives approximately 1 KV and a few tens of mA output at the high voltage side.

To further increase the output, a separate circuit consisted of a 555 TIMER oscillator at 20 KHz, and a 120 Watts power amplifier can also be used to power the primary winding.

* Information Unlimited, Box 716, Amherst NH 03031
** Radio Shack Electronics Store

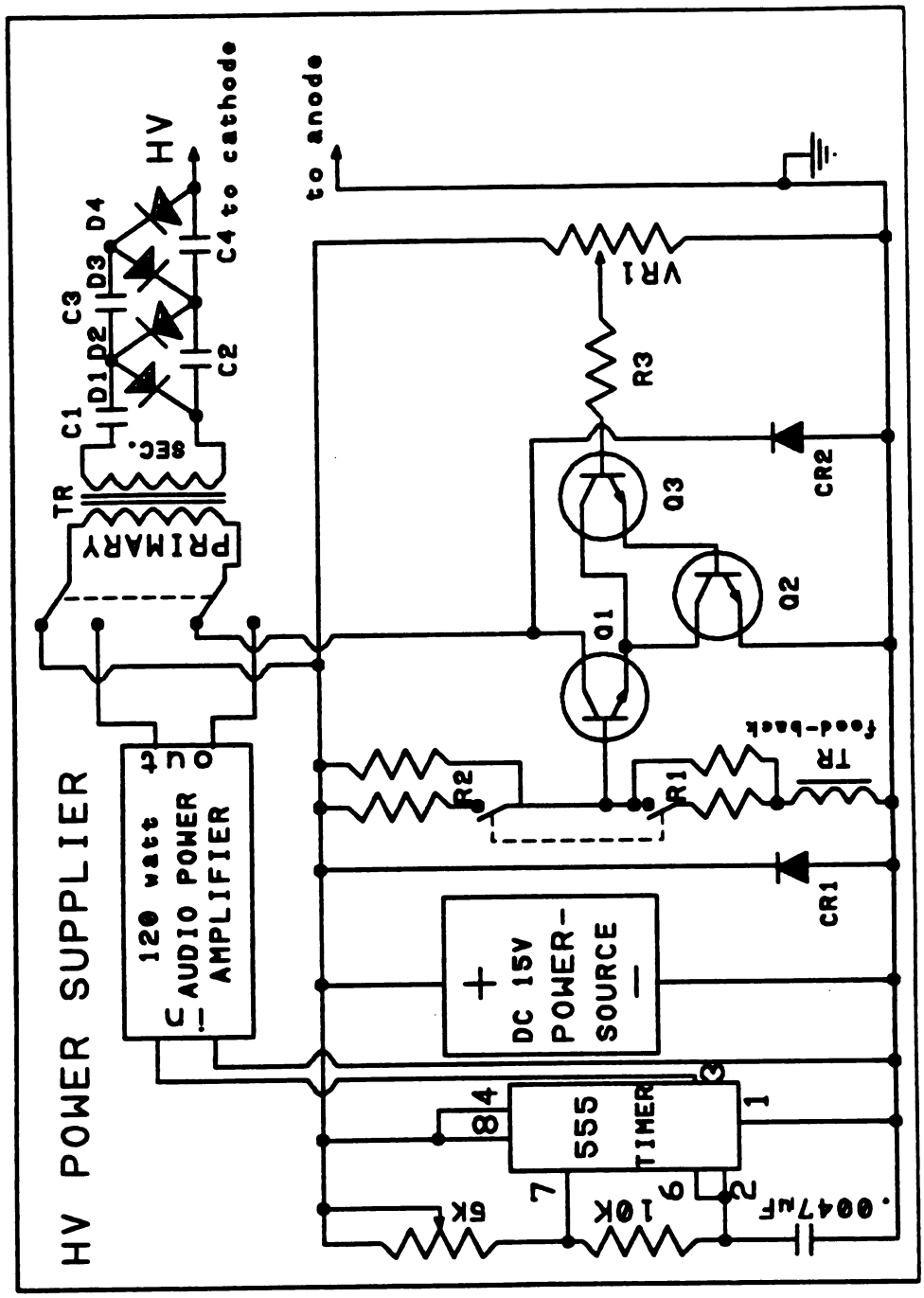

Figure 34. High frequency high voltage power supply

3.3.3.5

the hea

and al

Figure

holder

with a

resem

by a b

resolu

feed-f

CNS-

contr

using

in a

with

radia

*C a
N
H

3.3.3.5 X-Y Target Manipulator and Heated Substrate Heater

Left port of the chamber is used for specimen exchange. The specimen stage, and the heated substrate holder are mounted on a 8" flange that rides on rails for easy access and alignment. A picture of this setup, with the substrate holder removed, is shown in Figure 35 (a), and the heated substrate holder is shown in Figure 35 (b).

An x-y target manipulator is used, instead of a more common rotating target holder, to generate a zigzag area scanning that fully utilize a rectangular target surface with any beam spot size. The x-y manipulator is designed to have a low profile, and resembles a typical sample stage of a scanning electron microscope. Each axis is driven by a bellows sealed linear motion feed through.

Two stepper motors, SLO-SYN #MA61-FS-62019* with 200 steps per revolution resolution, and 60 oz-in normal holding torque, are used to drive the linear motion feed-throughs through telescopic double universal joints, NORDEX CMX-A1-1 and CNS-A1-1**, to accommodate linear motion and axial mis-alignment.

The stepper motor controller is built around two single-chip stepper motor controllers (HURST MFG. CO. NO. 220001***), and the scanning pattern is generated using a 556 DUAL-TIMER and six position switches.

Substrate heater is made of four layers of Fe-Cr-Al strip heating element enclosed in a alumina box with thin alumina sheets between the layers. This heater is covered with silver and has four stainless steel bolts to hold the substrates. A stainless steel radiation shield is used to reduce chamber heating and to increase heating efficiency.

* C and H Sales Co., 2176 E. Colorado Blvd., Pasadena CA 91107
** Nordex Co., 50 Newtown Rd., Danbury CT 06810-6216
*** Hurst MFG Co., Box 326, Princeton IN 47670

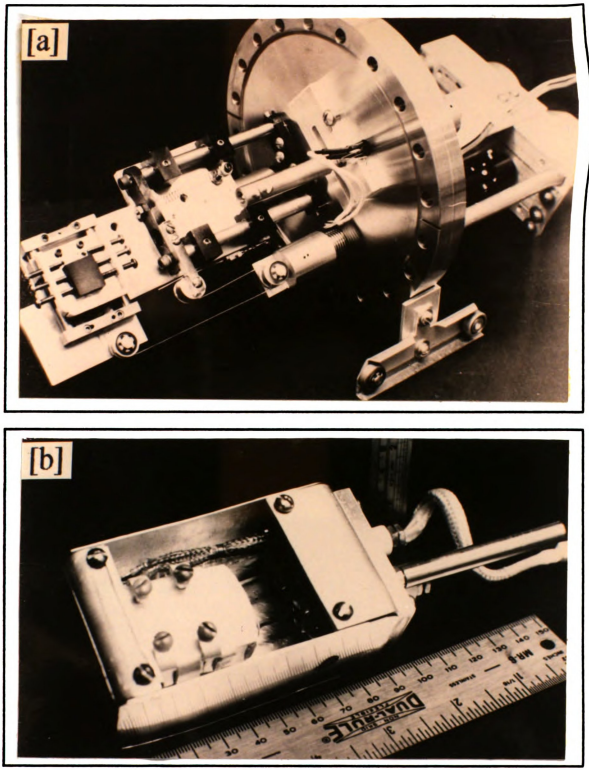

Figure 35. (a) Low profile x-y target manipulator and (b) Heated substrate holder

3.3.4. Ion-Beam Assisted Millisecond PLD Process (IBPLD)

An 8" quartz lens focuses the laser beam to an elliptical spot about 1 mm^2 in size on the target at 45° to the laser beam. Laser induced plume is ejected perpendicularly from the target toward the substrate at a distance about 3 to 3.5 cm from the target.

Substrates were held at 650 to 750 °C for IBPLD during deposition by a resistance heater. On the other hand, the deposition temperature for the multi-layer Ag/YBCO composites were 200 to 250 °C. This is to prevent peel-off of the tape from the substrate due to thermal mis-match*[101]*, and yet to provide enough temperature to achieve a good adhesion of YBCO film on the silver layer.

During deposition, the chamber was kept at 100 to 300 mtorr of oxygen after a pump down to 20 mtorr base pressure, and flushed with oxygen several times initially. For the ion-beam assisted deposition, a stream of oxygen ion, generated by the penning ion gun operated at about 1 KV, was used to supply activated oxygen to the plume and growing film. Figure 36 shows the laser induced plume and the oxygen ion beam with 40 J/cm^2 pulse energy density, 250 μs pulse-width and 300 mtorr oxygen pressure.

Important process parameter for IBPLD films and VTE / ms-PLD multi-layer tapes are listed in Table 4.

3.4 Post-annealing

Since the as-deposited PPLD and IBPLD films and the YBCO layers of the multi-layer tape were not superconducting, post-annealing was required.

The plasma assisted PLD films were annealed at 500, 600, 850 and 940 °C in air or oxygen for different times. For the IBPLD films, the post-annealing was made at 850°C for 30 to 120 minutes in air. Loss of film, especially from the corners and edges of samples, was occasionally observed. This can be prevented by covering the film with a

piece

anneal

Tab

piece of YBCO sintered bulk during annealing. YBCO/Ag multi-layer tapes were annealed in a YBCO box at 855 and/or 905 °C for 10 to 60 minutes in air.

Table 4. Important Processing Parameters for IBPLD Films and VTE / ms-PLD Tapes

PROCESS PARAMETERS	IBPLD FILMS	VTE / ms-PLD TAPES
SILVER LAYERS (VTE)		
Heat Source	——	tungsten wire basket
Evaporator Base Pressure	——	$1x10^{-5}$ Torr
YBCO LAYERS		
Wavelength	1064 nm	1064 nm
Pulse Width	0.25 - 2.2 ms	0.6 -2.5 ms
Repetition Rate	2 pulses / s	1 or 2 pulses / s
Spot Size on Target	~ 1 mm^2	~ 1, 3.5, or 7 mm^2
Pulse Energy Density	40 - 280 J / cm^2	60 - 300 J / cm^2
Peak Power Density	0.12 - 0.32 MW / cm^2	0.05 - 1 MW / cm^2
Substrate Temperature	650 - 750 °C	200 - 250 °C
Target to Substrate Distance	3.5 cm	3 cm
Chamber Pressure	100 to 300 mtorr of oxygen	100 to 300 mtorr of oxygen
Growth Rate	2.5 nm / s	2 - 50 nm / s
Target Material	Conventionally sintered YBCO with near stoichio-metry composition	conventionally sintered YBCO, 15% Ag doped YBCO, 23% Ag doped YBCO
Post-Annealing	850 °C for 30 to 120 min. in air	855 and/or 905 °C for 10 to 60 min. in a YBCO box

Figure 36. Laser induced plume and oxygen ion-beam

3.5 Sample Characterization Methods

3.5.1 Crystal structure and Phase Identification

X-ray diffraction (XRD) method was used to study the crystal structures, to identify phases and to control the post-annealing process. Cu Kα radiation, obtained by using a Ni filter or a double-crystal monochrometer, and a computer controlled diffractometer (Scintac-XDS-2000 diffractometer, Scintag Co.) were used. As sintered or as deposited surfaces were used most of the time; however, mechanically polished surfaces were also examined occasionally to isolate any possible surface effects such as surface texture and surface composition variation.

3.5.2 Microstructures and Chemical Compositions

Microstructures were studied using both optical microscope and scanning electron microscope (SEM). Samples for optical microscopy were metallographically polished following standard procedures using emery paper and alumina powder of various particle sizes. Small samples were hot mounted with bakelite before polishing. Methanol was used as the grinding medium to prevent moisture pickup and possible degradation of the superconductors.

Scanning electron microscopy was performed directly on diamond-saw cut surfaces or fracture surfaces for bulk samples, and top surface or fracture cross-section for films and tapes. Samples were ultrasonically cleaned in methanol and mounted with copper conducting tape or silver paint. A very thin conducting vacuum evaporated coating of Pt-Pd was used for microstructure observation of as deposited non-superconducting films.

A Link energy dispersive x-ray spectroscope (EDS) attached to the Hitachi S-2500C scanning electron microscope was used for chemical analysis. EDS quantitative analysis of the cations was made possible using calibration standards and the ZAF software supplied with the system. The background noise calibration and processor gain calibration were performed using Au Lα1 line at 9.711 KeV.

The standards have to cover all elements analyzed and have to be as close as possible chemically to the unknown sample. For YBCO samples, a sintered stoichiometric bulk was used as a standard due to non overlapping strong emission lines, i.e. Y L-lines, Ba K-lines and Cu K-lines.

On the other hand, four different oxides, $SrCuO_2$, Ca_2PbO_4, Bi_2CuO_4 and Ca_2CuO_3, were used as standards for the Pb doped BSCCO due to overlapped emission lines. All the standards were prepared from high purity metal oxides or carbonates by solid state sintering process similar to the preparation of bulk high T_C superconductors. All standards were calcined at 600 °C for 15 h and 750 °C for 3 h, followed by sintering at 900 °C for 48 h except for Bi_2CuO_4 which was sintered at 800 °C for 2 h. Final compositions of the standards were determined by ion coupled plasma (ICP) analysis.

3.5.3 Electrical Resistance and Magnetic Susceptibility Measurements

Resistance measurements were performed using an auto-balancing ac bridge with a lock-in amplifier (Linear Research LR-400) with a standard four-probe technique. This bridge is equipped with a mutual inductance option that allows this instrument to function as an auto-balancing mutual inductance bridge. Thus, the mutual inductance, which is proportional to the ac magnetic susceptibility of the in-phase component (χ') can be measured directly. This bridge has an adjustable excitation current from 1 μA to 3 mA and resolutions of 1 micro-ohm and 1 micro-henry for the resistance and mutual inductance modes respectively. Figure 37 is a wiring diagram for both resistance and mutual inductance measurements.

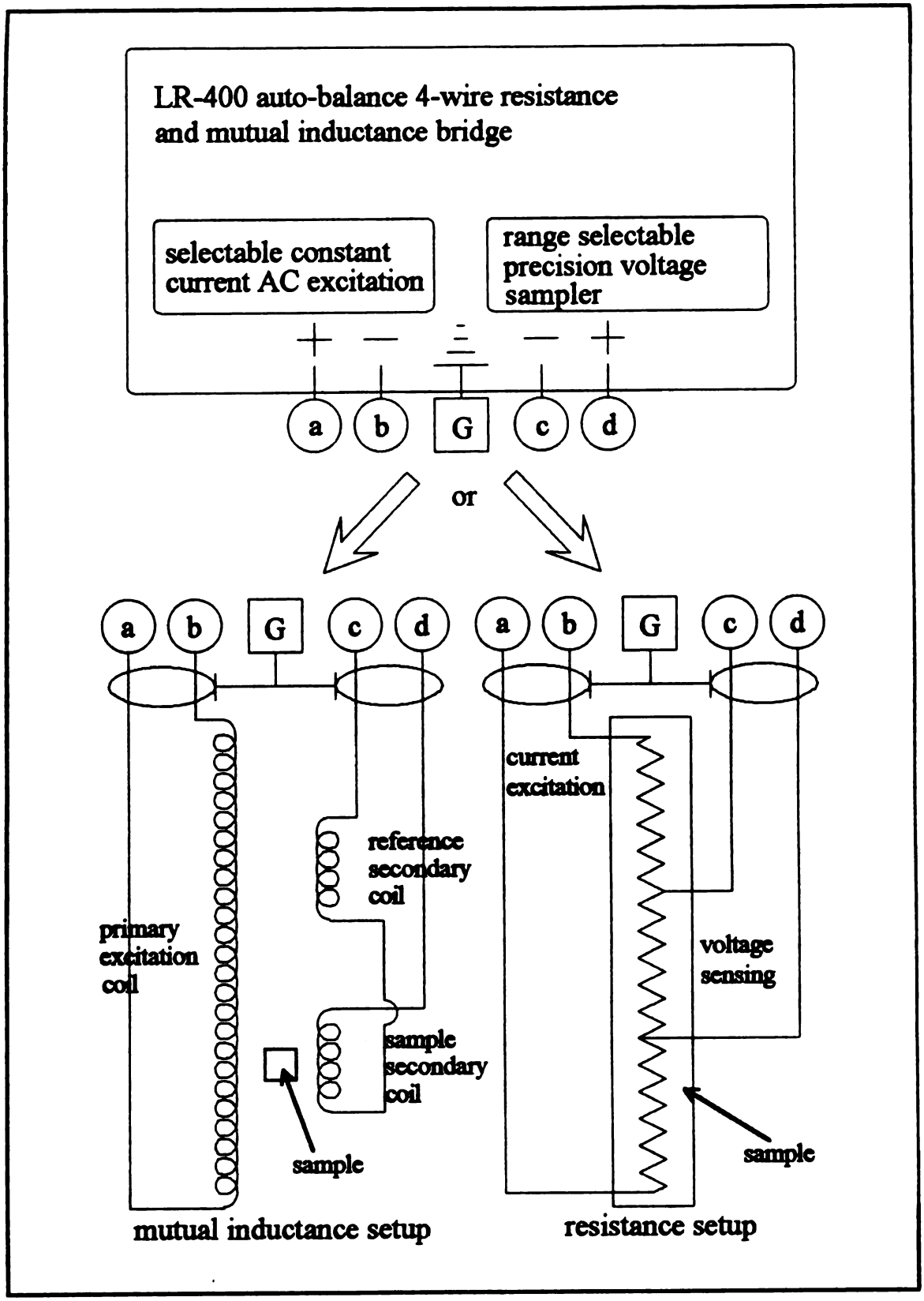

Figure 37. Wiring diagram for both resistance and mutual inductance measurements

Figure 38 is a sketch of the computerized resistance versus temperature (R-T) measurement setup. Four-point contacts are formed by sandwiching four rectangular gold-coated wire-wrap pins and the sample between two bakelite blocks and two poly-vinyl chloride (PVC) blocks. The rigid bakelite outer blocks are used to insure uniform clamping pressure on the four pins, and the deformable PVC inner blocks are used to accommodate the thermocouple and slight variation of the pins and sample thickness.

The sample is cooled by inserting the whole clamp setup into a half filled liquid nitrogen dewar, Figure 39. A very stable cooling can be achieved in the liquid nitrogen vapor to within 10 K of the liquid nitrogen boiling point. The cooling rate can be increased by decreasing the distance from the liquid nitrogen surface or by increasing the heater power to create more vapor. A manual laboratory jack or a stepper motor driven linear motion threaded rod is used to control the distance between the sample clamp and the liquid surface. For temperature close to 77 K, the sample clamp is completely submerged in liquid nitrogen, and then slowly lifted out of the liquid nitrogen.

Figure 40 is a sketch of the magnetic susceptibility measurement device that consists of induction coils, specimen holder with thermocouple, and liquid nitrogen delivery system. The circuit diagram is shown in Figure 37.

When the ac excitation current was applied to the primary coil made of 3000 turns of #32 AWG magnet wire, it produced a uniform magnetic field around the secondary coils made of 2000 turns #34 AWG magnet wire each. In the absence of a magnetic material, the ac voltage induced by the sample secondary coil exactly cancels the ac voltage induced by the reference secondary coil. However, a non-zero signal is proportional to the magnetic susceptibility of the sample if a magnetic material is present in the sampling coil.

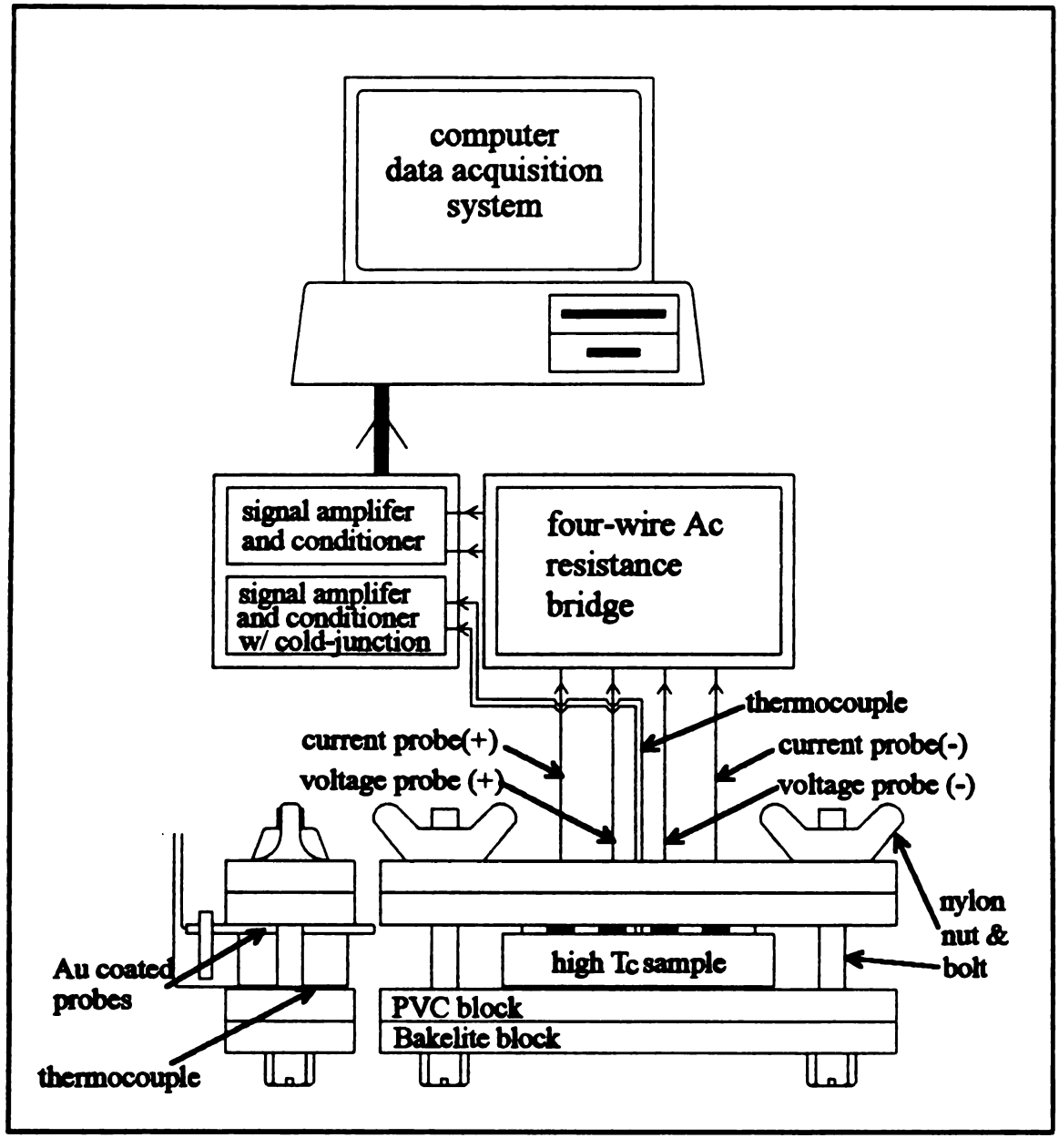

Figure 38. Computerized resistance - temperature measurement setup

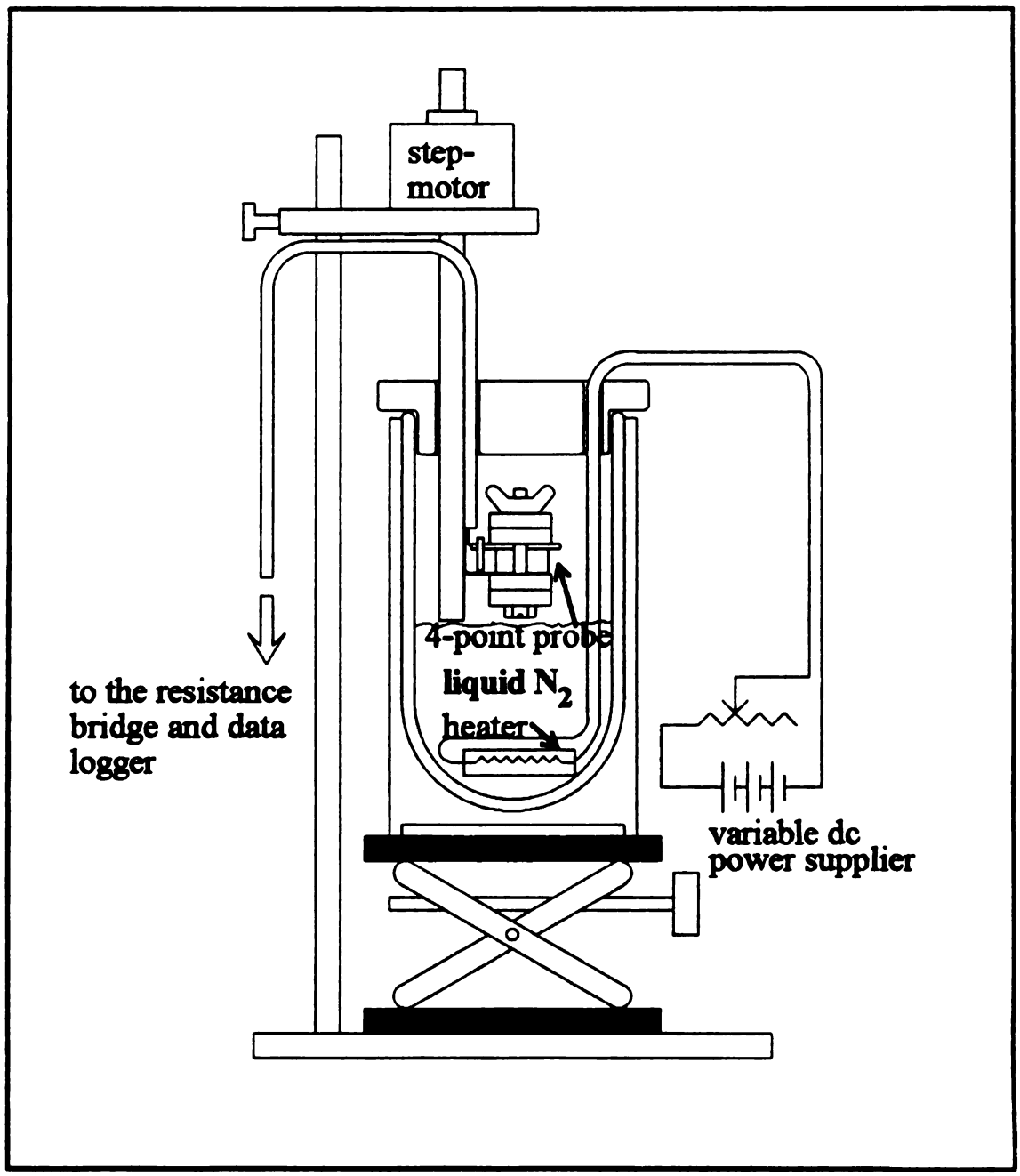

Figure 39. Cooling device for resistance - temperature measurement

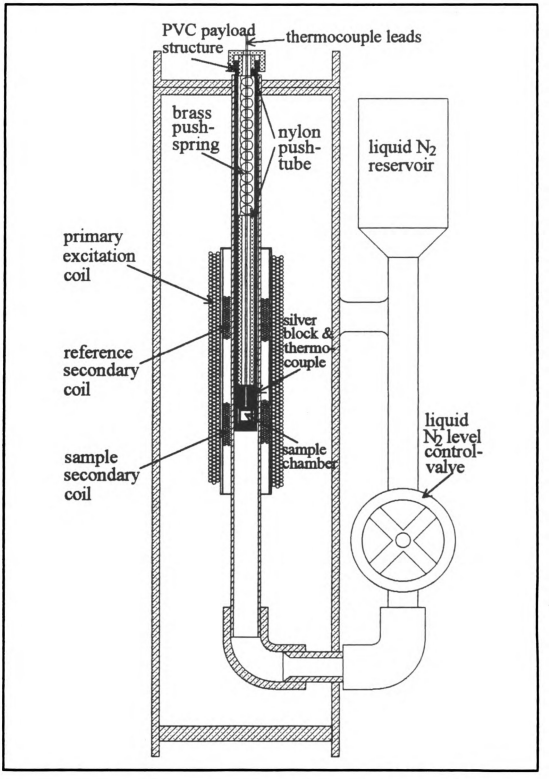

Figure 40. Magnetic susceptibility measurement apparatus

T

ooled b

ontrol-v

nductar

ample

backgro

3.5.4 Fo

using

distanc

suppo

(d) we

streng

3P(L-

testec

To obtain the temperature dependence of magnetic susceptibility, the device is cooled by liquid nitrogen. After the temperature is stabilized, the liquid nitrogen level control-valve is shut to let the temperature rise slowly. Temperature and mutual inductance are continuously recorded via a computer. A reference curve, with an empty sample holder, is collected before each sample curve as the background. The background is deducted from the sample curve to get the final result.

3.5.4 Four-Point Bending Test

The mechanical strengths of YBCO and Ag-doped YBCO targets were compared using a four-point bending test. Figure 41 shows the four-point bending device. The distance between the outer supports (L) is 20 mm, and the distance between the inner supports (a) is 10 mm. Rectangular bar specimens of 6 mm width (b) and 2.5 mm depth (d) were used. The modulus of rupture (MOR) is the flexural strength, i.e. the fracture strength of a material under bending load. For four-point bending MOR equals $3P(L-a) / 2bd^2$. Sets of five samples each from YBCO and 15% Ag-doped YBCO were tested to determine strength.

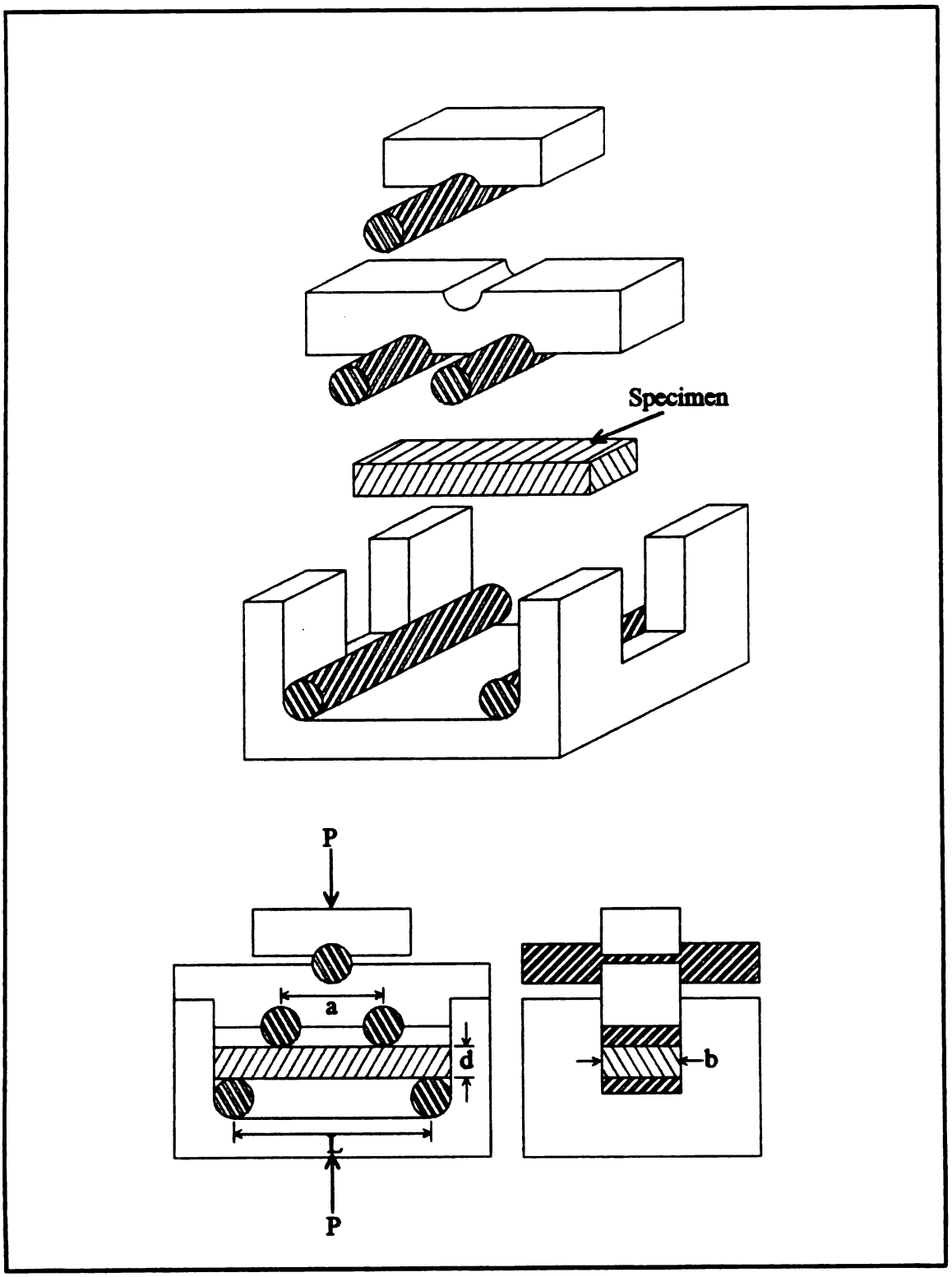

Figure 41. Four-point bending setup

4. RESULTS AND DISCUSSION

4.1 Factors Which Affect Processing of Bulk YBCO Superconductors

It was found that careful wet grinding and firm hand packing greatly accelerates the calcination, and formation of the YBCO compound. Furthermore, higher purity of starting oxides and carbonate, i.e. purity of 99.99% or better, also enhanced the formation of the YBCO compound over the 99.9% purity starting chemicals, Table 5.

It was also found that powder preparation before final sintering affects quality of the sintered superconductor. Highest green density was obtained with well crystallized YBCO powder, i.e. powder with shiny black particles.

4.2 Laser Calcination and Kinetics of Formation of BSCCO - 2223 Phase

Since the discovery of superconductivity in this compound*[31]*, many efforts have been made to maximize the amount of high T_c - 2223 (110 K) phase. A major enhancement in the formation of high T_c - 2223 phase was made by doping Bi-Sr-Ca-Cu-O compound with Pb*[32-36]*. However, with Pb doping, about 200 hours of total processing time is required to obtain a single or nearly a single high T_c phase.

4.2.1 Kinetics of Formation of BSCCO - 2223 Phase

It has been shown that addition of Pb enhances the formation of 110 K (2223) phase in Bi-Sr-Ca-Cu-O system because of kinetic reasons*[32]*. It has also been shown that formation of the high T_c phase can be enhanced by melt-quench method with Ca and Cu rich starting compositions*[37]*.

Table

Table 5. Effect of starting powder purity and powder compaction on formation of YBCO

			99.9+% starting chemicals		99.99+ starting chemicals
			loose powder	firmly hand packed power	
930 °C 7 hr X 1	color of bulk		pale green	dark green	dark green
	bonding and shrinkage		loose powder	very weakly bonded	weakly bonded
	meissner effect	bulk	no	no	no
		powder	no	partially and very weak	partially mixed of strong and weak
930 °C 7 hr X 2	color of bulk		green	very dark green	dull black
	bonding and shrinkage		loose powder	weakly bonded and no significant shrinkage but crushed powder is not fluffy easy to pack	strongly bonded, shrunk significantly and crushed powder is easy to pack
	meissner effect	bulk	no	weak	weak
		powder	no	more than half is strong	more than half is strong
930 °C 7 hr X 3	color of bulk		dark green	dull black	shiny black
	bonding and shrinkage		very weakly bonded	strongly bonded and shrunk significantly	strongly bonded and very hard to crush
	meissner effect	bulk	no	strong	strong
		powder	partially and very weak	majority strong	all strong
930 °C 7 hr X 4	color of bulk		very dark green	shiny black	—
	bonding and shrinkage		weekly bonded and no significant shrinkage	strongly bonded and well crystallized	—
	meissner effect	bulk	weak	strong	—
		powder	partially and weak	all strong	—
930 °C 7 hr X 5	color of bulk		dull black	—	—
	bonding and shrinkage		bonded and shrunk significantly	—	—
	meissner effect	bulk	fair	—	—
		powder	partially strong	—	—
930 °C 7 hr X 6	color of bulk		shiny black	—	—
	bonding and shrinkage		strongly bonded and well crystallized	—	—
	meissner effect	bulk	strong	—	—
		powder	majority strong	—	—

A similar melt-quench effect was obtained when Bi-Pb-Sr-Ca-Cu-O powder mixture was exposed to high energy and short duration laser pulses. Coarse particles were formed by localized melting. Due to a localized rapid heating and quenching, chemical homogeneity of the well mixed starting powder was preserved. Therefore, we were able to greatly increase the rate of formation, and the volume fraction of the high-T_C phase ($T_C \sim 110$ K) without using any excess Ca and Cu in the starting powder.

The mechanism of formation of high T_C phase by laser and conventional processes appear to be quite different as indicated by the XRD data. As seen in Figure 42, the conventionally processed sample initially showed a mixture of low T_C - 2212 phase and Ca_2PbO_4. As the duration of sintering increased, the amount of Ca_2PbO_4 decreased, and a phase cycling behavior was observed*[35]*. The high T_C - 2223 phase was then formed by a reaction between the low T_C phase with Ca_2PbO_4 and Ca_2CuO_3 *[102,103]*.

Different results were observed for two laser processed samples at two different laser powers, Figure 43 and 44. At an early stage of sintering, predominately a low T_C - 2212 phase was formed. After prolonged sintering, the high T_C phase, $Bi_2Sr_2Ca_2Cu_3O_X$, was formed via an unbalanced reaction of the following form*[104]*:

$$2Bi_2Sr_2CaCu_2O_X \rightarrow Bi_2Sr_2Ca_2Cu_3O_Y + Bi_2Sr_2CuO_Z$$

The initial formation of 2212 phase leaves some excess Ca and Cu ions of the starting stoichiometric 2223 composition. The 2201 ($Bi_2Sr_2CuO_Z$) phase formed, then combines with the unused Ca and Cu ions to form the low T_C - 2212 phase. Therefore, compared to the high T_C - 2223 phase, the amount of retained 2201 phase in laser calcined samples was not large.

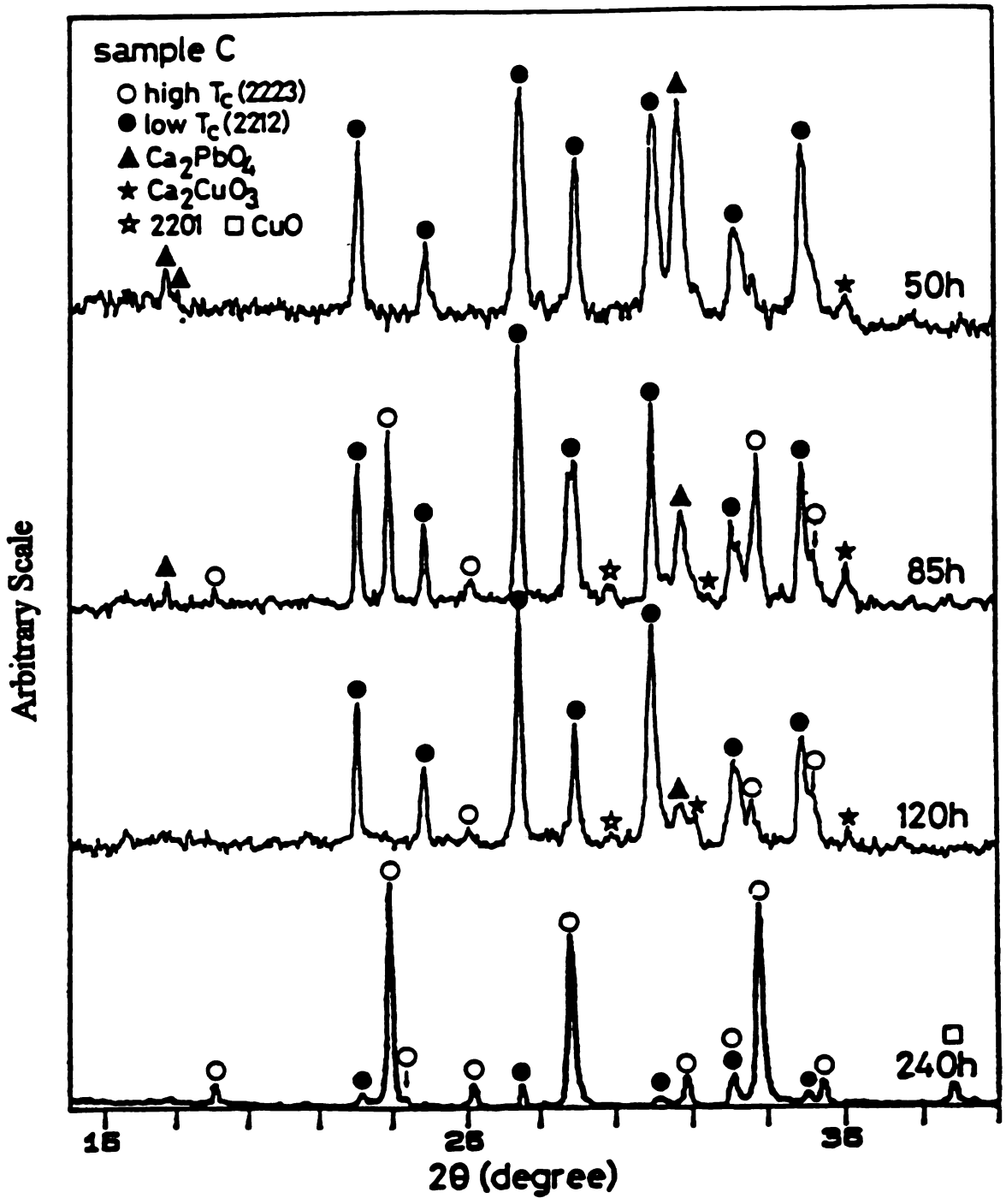

Figure 42. XRD patterns of conventionally processed Pb-doped BSCCO sample

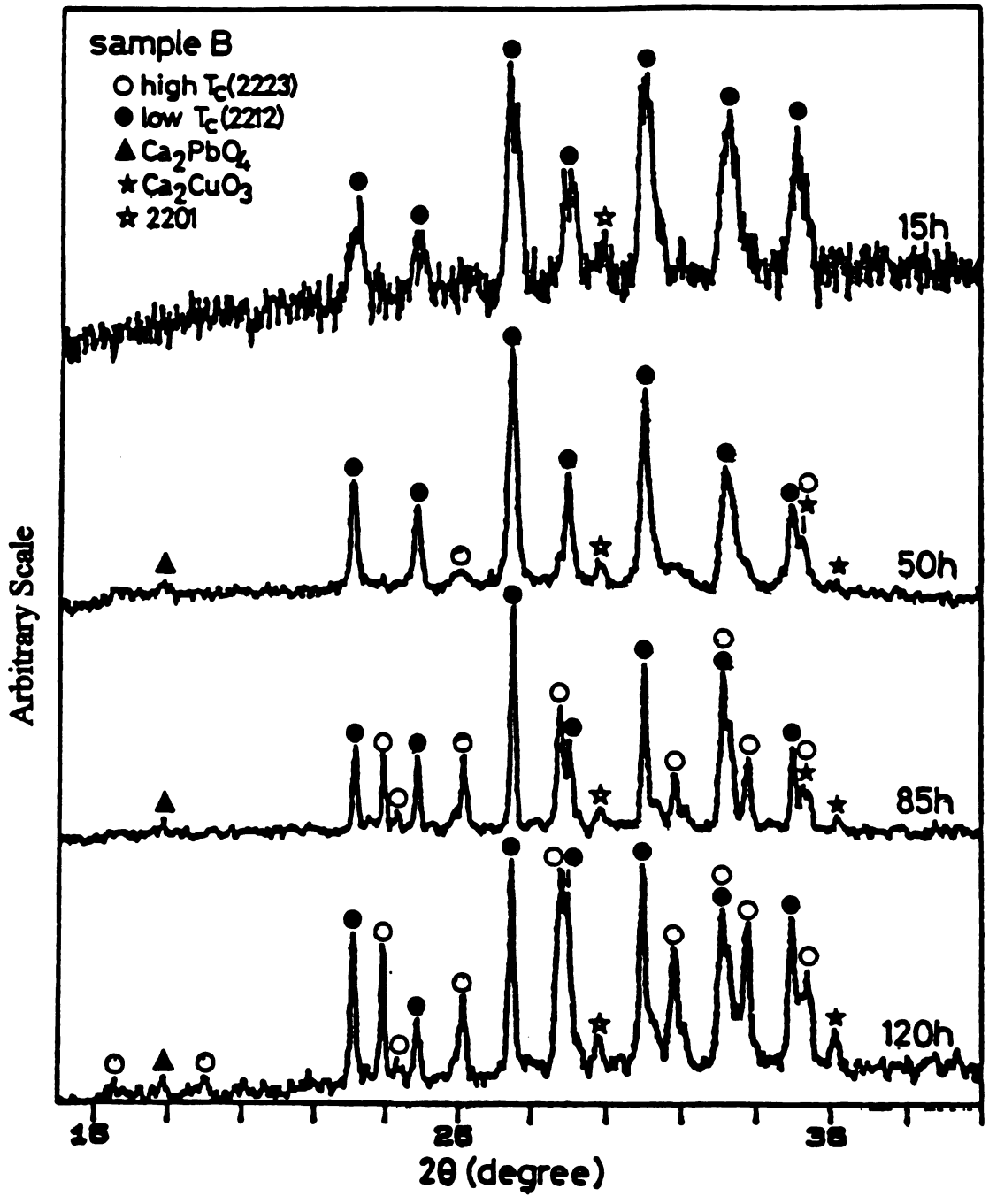

Figure 43. XRD patterns of 50 Watts laser-processed Pb-doped BSCCO sample

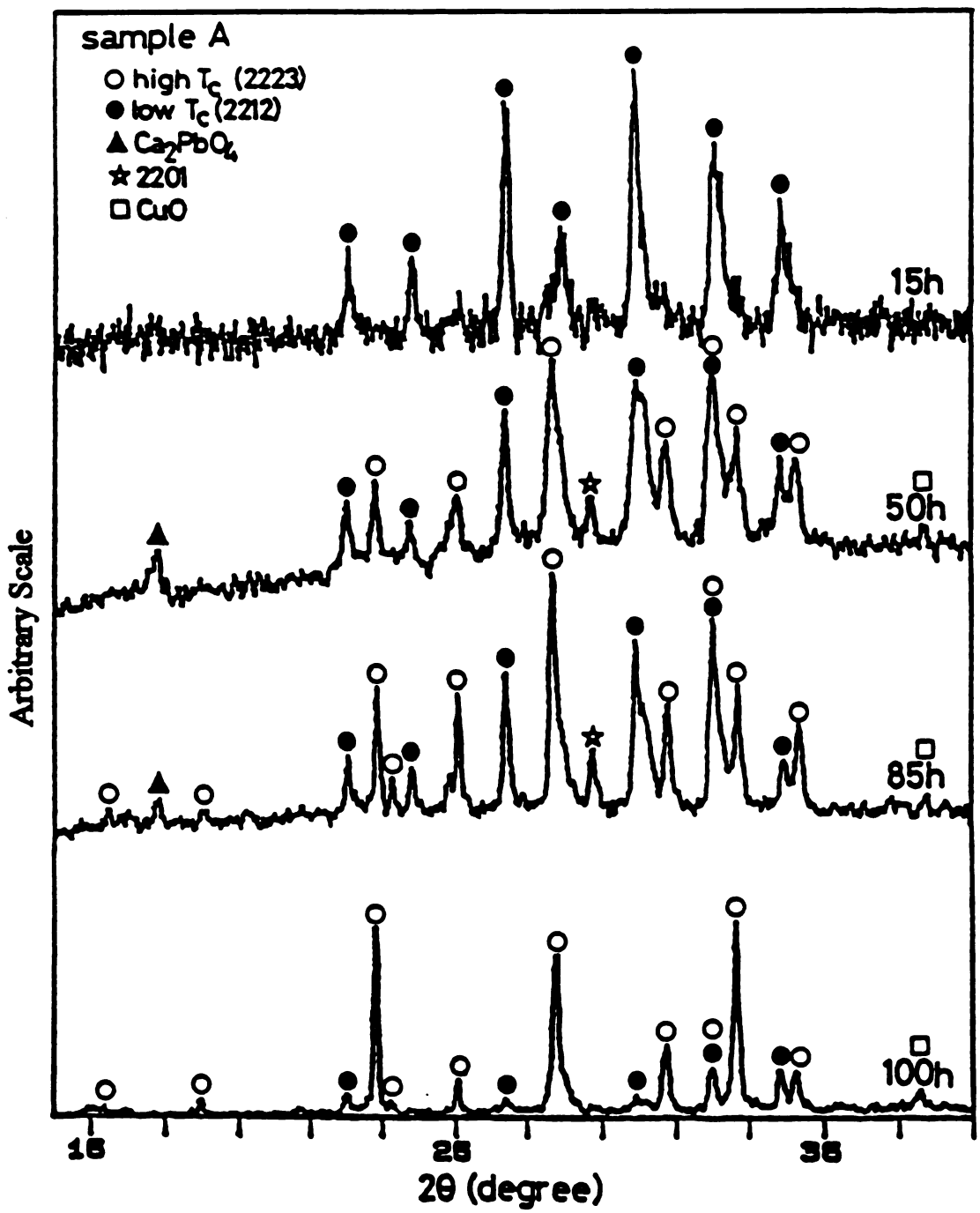

Figure 44. XRD patterns of 90 Watts laser-processed Pb-doped BSCCO sample

A considerable amount of Ca_2CuO_3 was also formed in sample B after prolonged sintering. Due to the complexity of this sample, it is difficult to determine how much Ca_2CuO_3 was present. EDS analysis were performed on fractured surfaces of this sample. The EDS and XRD data support the assumption that Ca was in fact trapped in the form of Ca_2CuO_3 in the sample B*[39]*. Thus, a low volume fraction of high T_c phase and the zero resistance temperature below 77 k were observed for this sample.

Due to the high energy density of the laser beam some weight loss, in the form of particulate ejection, of the starting powder is unavoidable during laser calcination process. Thus, the final compositions of laser calcined and conventionally calcined sample were analyzed by EDS rather than by a weight loss measurement. No significant compositional difference was found through the chemical analysis.

4.2.2 Microstructures and EDS Analysis of Laser Calcined BSCCO

Scanning electron micrographs shown in Figures 45 (a) and (b) indicate a characteristic plate-like grain structure. The 90 Watts laser-processed sample , fig 45 (a), showed well-grown plates 10-30 μm wide and about 1 μm thick. The plate size of laser processed sample was about 2-3 times as large as the conventionally processed one. Scanning electron micrograph of 50 Watts laser-processed sample shows plate-like grains and some not very well defined phase, Figure 46. Figure 47 shows EDS spectra collected from areas of the samples shown in Figure 45 and 46.

Figure 45. Scanning electron micrographs of (a) 90 Watts laser-processed sample, sample A, and (b) conventionally processed sample, sample C

Figure 46. Scanning electron micrograph of a 50 Watts laser-processed sample

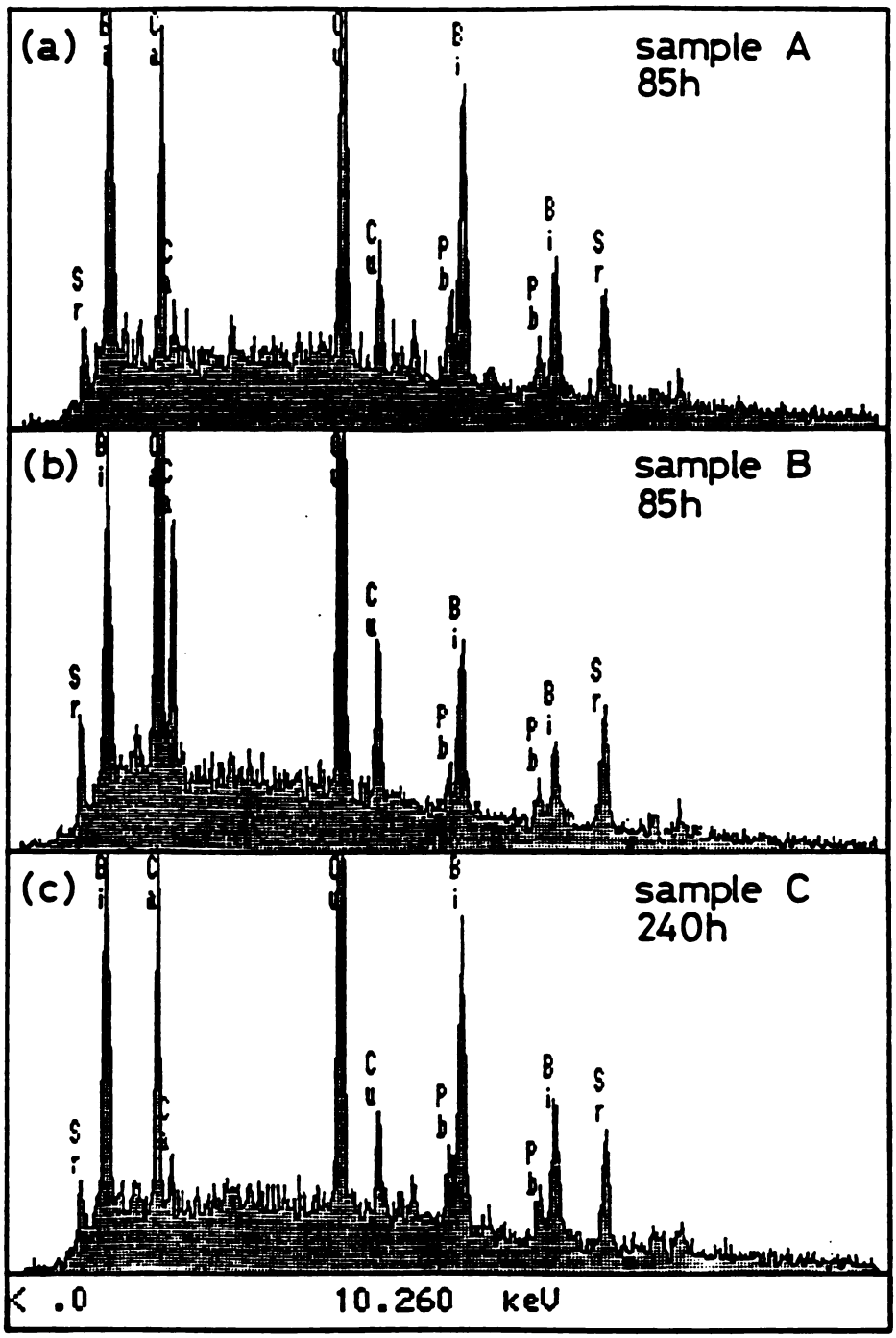

Figure 47. EDS spectrums collected from areas of the samples shown in Figure 45 and 46

4.2.3 Resistance and Susceptibility Measurements of Laser Calcined BSCCO

The measurements made on the resistance and the magnetic susceptibility of laser and conventionally processed samples are plotted as a function of temperature in Figure 48 (a) and (b). All these samples show superconducting onset temperature of about 110 K. The zero resistance temperature of 90 Watts laser-processed sample, after 100 hours sintering, is about 98 K.

The second inflections of the ac susceptibility curve were observed for sample A, sintered for 100 hours, and sample C, sintered for 240 hours. The second inflection in these two samples is likely due to Josephson-like weak coupling between the high T_c grains*[105]*. A sharp drop in magnetic susceptibility for sample A, sintered for only 85 hours, can therefore be attributed to the absence of Josephson-like weak coupling. Although the laser and conventionally processed samples show similar onset transition temperatures and overall trends, the results showed that depending on the processing conditions the laser processed samples can have a significantly large resistance transition width.

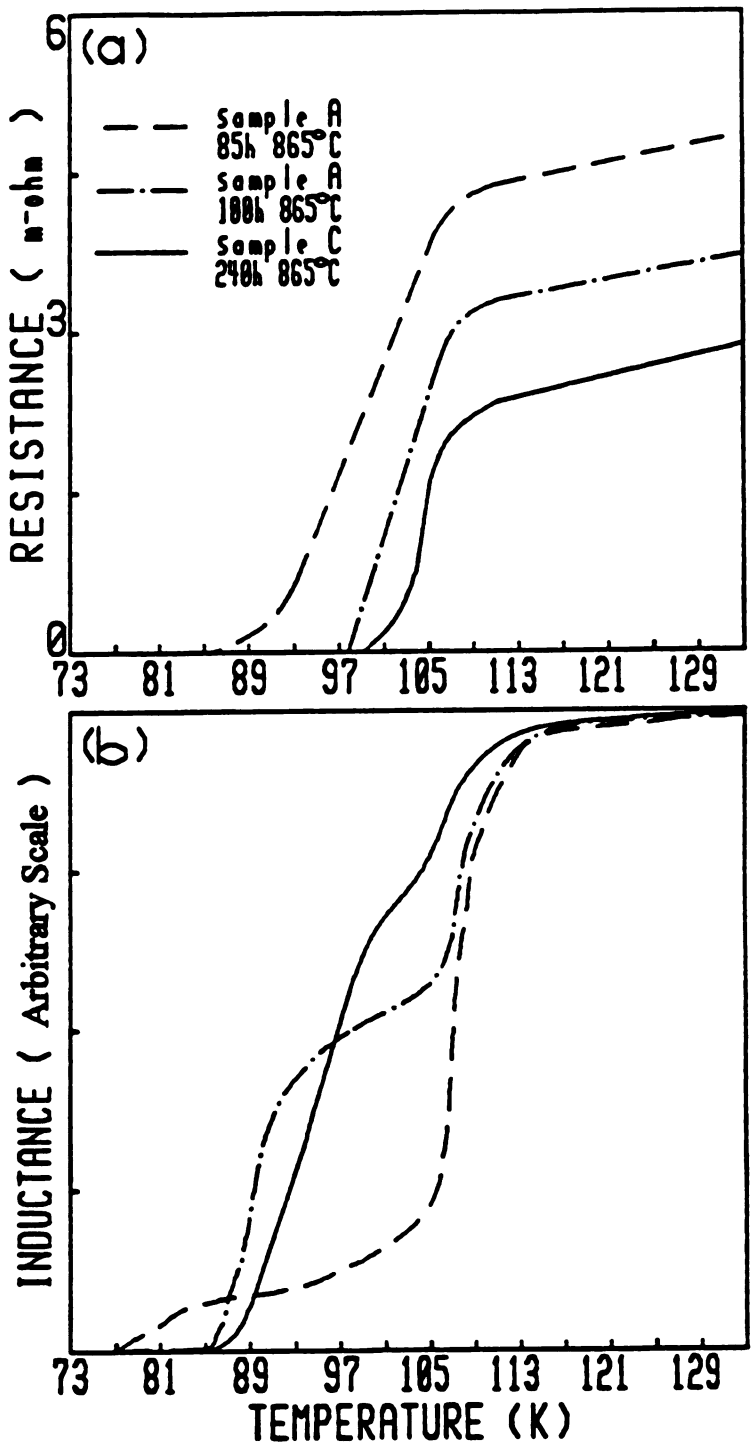

Figure 48. (a) Resistance vs. temperature curves and (b) Magnetic susceptibility vs. temperature curves of conventionally processed and 90 Watts laser-processed samples

4.3 Millisecond Pulsed Laser Vapor Deposition

4.3.1 Problems with Millisecond PLD

4.3.1.1 Target Overheating Problem and Peak Power Density limitation

The greatest problem with the millisecond pulse deposition is overheating of the target due to high pulse energy density input required to create a reasonable peak power density on the order of a million W/cm^2 for deposition.

This is due to approximately five orders of magnitude longer pulse-width of the millisecond laser pulse. Hundreds of Joule/cm^2 pulse energy density is required to achieve a peak power density close to a million Watt/cm^2, which is still much lower than the peak power density produced by a nanosecond laser pulse at typically a few J/cm^2 energy density.

With a rotating target, overheating and severe local melting are major problems. A very high pulse energy is required to obtain the required peak power density because of the large, 15 mm^2 elliptical, spot size necessary to cover the entire width of the ring to prevent uneven erosion of the target.

To avoid formation of excessive liquid phase, and severe segregation with a rotating ring-target, pulse energy and pulse energy density are limited to 6 Joules and 60 J/cm^2. However, the maximum peak power density is restricted below 0.02 MW/cm^2 with a 2.2 ms pulse-width.

4.3.1.2 Oxygen Depletion

As mentioned before oxygen stoichiometry is very critical in obtaining a good YBCO superconductor, and the equilibrium oxygen content decreases at elevated temperatures. Oxygen depletion on the deposited film is expected due to a combination of high laser-induced plasma-temperature and a low oxygen pressure. Moreover, this problem is expected to be aggravated by the high deposition rate of ms-PLD process.

4.3.2 Pressure Dependence of Laser Induced Plume

It is found that the shape of the plume, thus the angular distribution of the vapor species, is strongly dependent on the pressure in the deposition chamber, Figure 49. The difference is even more evident by comparing laser induced plumes in vacuum and in one atmosphere air, Figure 50. The angular dependence of various species and dependence of their spatial distribution on the chamber pressure and other parameters can be studied using a spatially resolved emission spectrometer.

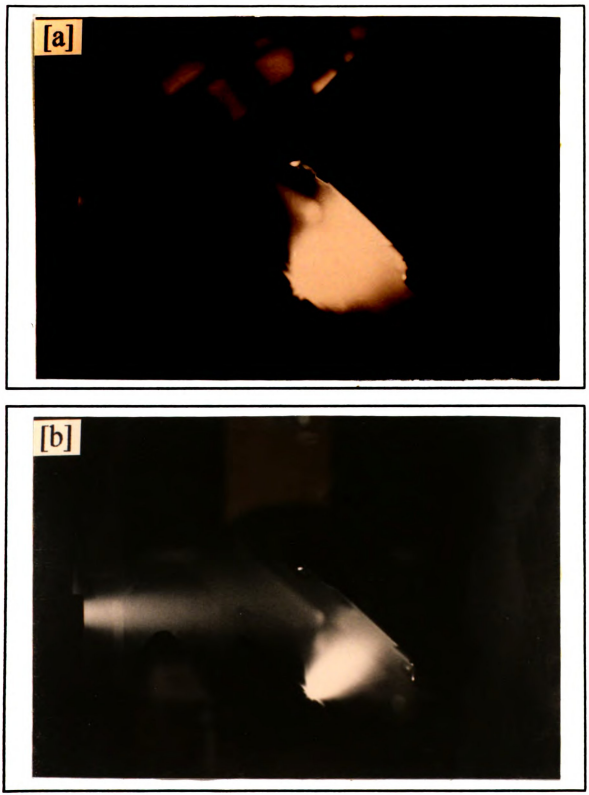

Figure 49. Oxygen ion-beam, and laser induced plume with 250 μs pulse-length and 40 J/cm^2 pulse-energy density at oxygen pressure of (a) 100 mtorr and (b) 300 mtorr

Figure 50. Laser induced plume with 250 μs pulse-length and 40 J/cm^2 pulse-energy density in one atmosphere air

4.3.3

4.3.

ma

use

be

of

0.1

pu

su

pu

4

c

c

n

c

p

4.3.3 Ion-Beam Assisted Millisecond PLD

4.3.3.1 Effect of X-Y Target Manipulator

To ease the overheating problem and peak power limitation, a x-y target manipulator was used to obtain a zigzag scanning pattern instead of a more commonly used rotating target configuration. This allows the whole area of a rectangular target to be scanned with a much smaller laser spot size.

As a result, much higher peak power density can be obtained with a combination of much shorter pulse and much smaller pulse-energy. Peak power density as high as 0.16 MW/cm^2 was obtained with a 1 mm^2 spot size, 0.4 J pulse energy and 250 μm pulse-width.

Even with pulse-energy density as high as 0.16 MW/cm^2, a relatively flat target surface can be maintained. This is due to the fact that a small laser spot and low pulse-energy allow more cooling time on each location of the target surface .

4.3.3.2 Effect of Oxygen Ion Gun

A very large difference was found between films deposited under identical conditions except with or without an oxygen ion-beam.

When deposited without an oxygen ion-beam, Figure 51 (a), only a very light coating of a light brown color is deposited on the substrate which is about 0.5 cm recessed in the heater. The brown color of the film indicates oxygen deficiency. The light coating may be explained by the position of the substrate which is located outside the plume, Figure 49 (a).

Under the same conditions, except with the oxygen ion-beam turned on, a uniform black coating is obtained on the substrate, Figure 51 (b). This observation indicates that oxygen ion beam not only helps to replenish oxygen but also helps to drive vapor species onto the substrate.

4.3.3.3 Spatial variation of film composition

An uniform coating of YBCO, with large area coverage more than 1" diameter, has been successfully deposited on fused silica substrates by ion-beam assisted laser vapor deposition, Figure 52. Typical energy dispersive spectra of YBCO film and YBCO target are shown in Figure 53. Results of quantitative analysis using EDS are summarized in Table 6. Compared to the stoichiometric composition, as-deposited film is slightly high in barium content and low in yttrium and copper contents. However, an increase in yttrium and a further decrease in copper contents are observed after the post annealing treatment.

Table 6. Typical compositions of YBCO films produced by IBPLD process

sample conditions	yttrium atomic %	barium atomic %	copper atomic %
as deposited on silver substrate	14.6	37.1	48.3
850 °C 60 min. annealed on silver substrate	18.8	36.6	44.6
850 °C 120 min. annealed on Ag-coated (001) YSZ	18.4	34.1	45.8
850 °C 60 min. annealed on Ag-coated alumina substrate	21.2	34.1	44.7

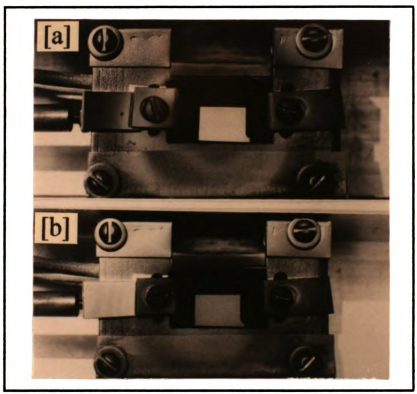

Figure 51. Silver substrates in substrate heater after laser vapor deposition with 0.25 ms laser pulses, 40 J/cm^2 pulse energy density and 100 mtorr of O_2 deposited (a) without ion-beam and (b) with ion-beam

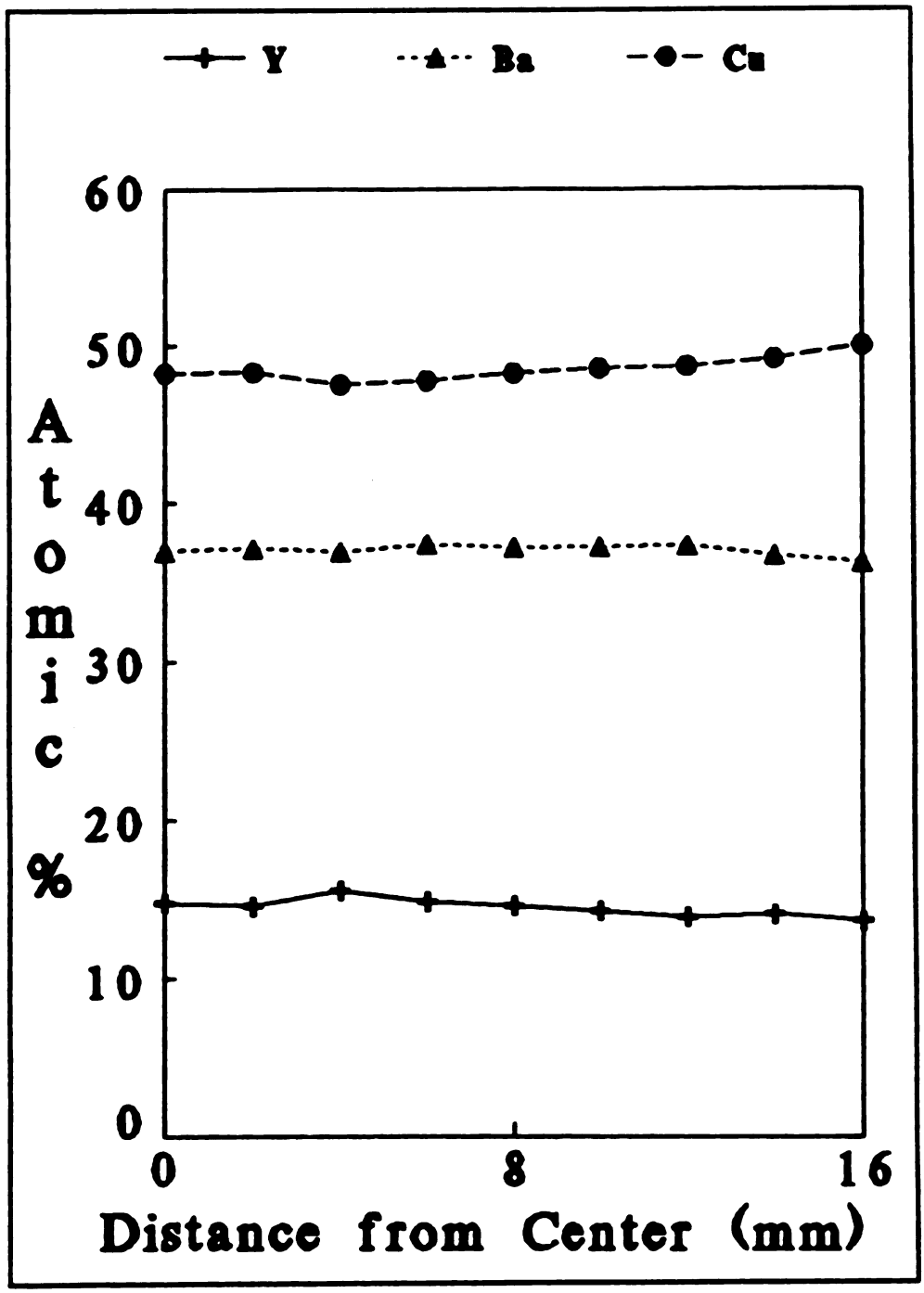

Figure 52. Chemical composition distribution of as deposited IBPLD YBCO film on fused silica substrate (quantitative EDS analysis)

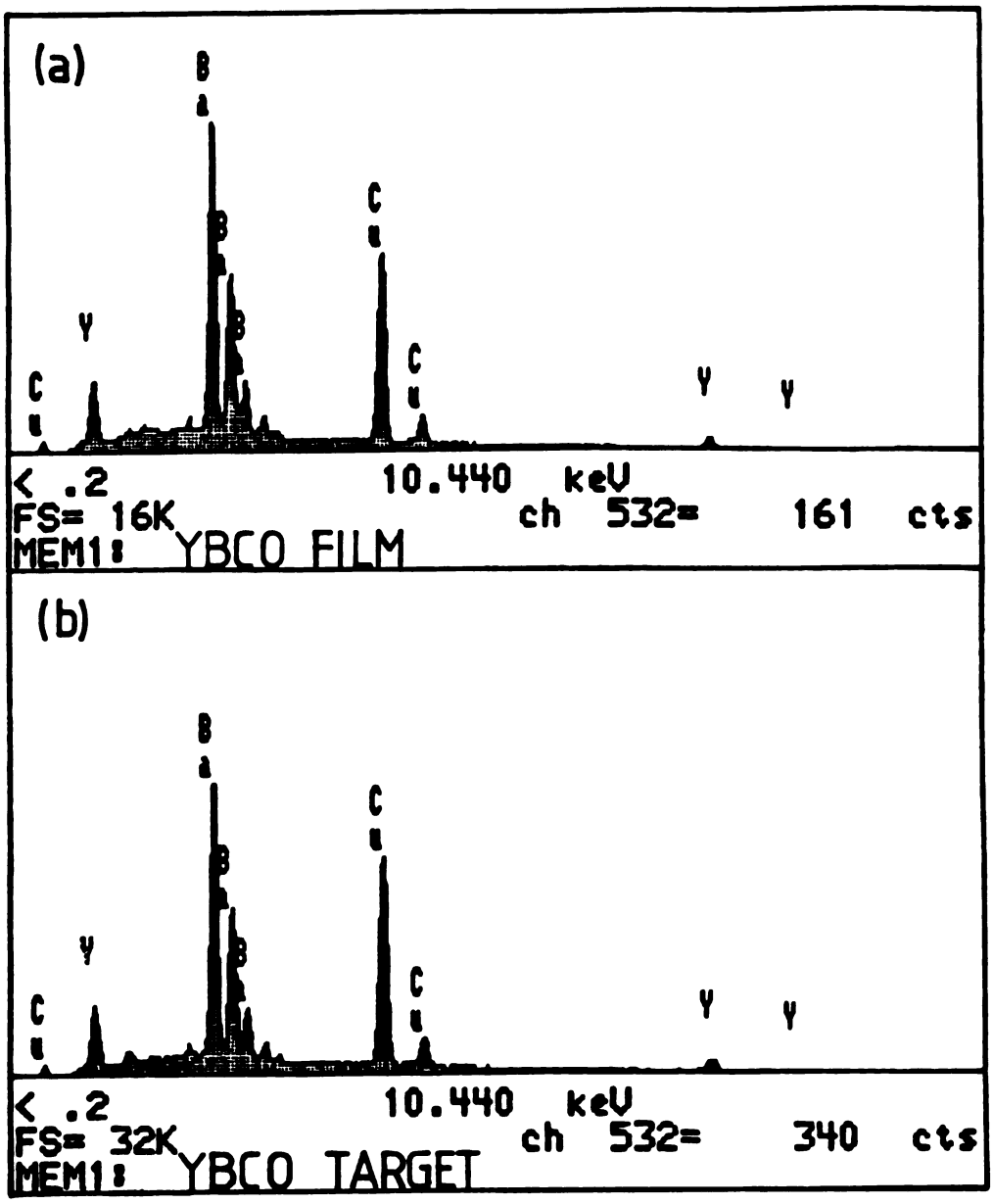

Figure 53. Typical EDS spectrums from (a) a IBPLD YBCO film and (b) a YBCO target

4.3.3.4

summ

diffra

broad

BaO a

Ta

1-2.

the

and

ind

4.3.3.4 X-ray Diffraction Analysis of IBPLD Films

Data on XRD study of as-deposited and annealed films on silver substrate are summarized in Figure 54. Due to a high deposition rate of the IBPLD process, x-ray diffraction patterns of as-deposited films only show peaks from the substrate plus a few broad peaks around 30° of 2θ angle which are attributed to various compounds of Y_2O_3, BaO and CuO as well as Y_2BaCuO_5, also known as 2-1-1 phase*[106]*, Table 7.

Table 7. List of possible compounds which might produce a strong diffraction peak near 30° of 2θ for Cu Kα radiation

COMPOUND	2-theta	I	HKL	2-theta	I	HKL	2-theta	I	HKL
$2BaO.Y_2O_3$	30.4	x	103	28.8	7	110	41.14	4	200
$3BaO.2Y_2O_3$	29.28	x	110	30.09	9	112	42.6	4	207
$4BaO.Y_2O_3$	30.09	x	—	29.09	9	—	41.6	5	—
BaO.CuO	29.33	x	600	30.15	5	611	40.05	3	741
$BaO.Y_2O_3$	29.68	x	320	29.48	6	40	31.05	6	121
$2CuO.Y_2O_3$	31.32	x	211	33.2	9	204	33.51	5	13
$2Y_2O_3.3ZrO_2$	29.7	x	211	29.42	4	3	34.35	3	122
$BaO.ZrO_2$	30.14	x	110	43.14	4	200	53.52	4	211
$2BaO.ZrO_2$	29.18	x	103	29.83	9	110	43.33	3	200
$3BaO.2ZrO_2$	30.16	x	110	29.58	9	105	43.22	6	200
Y_2BaCuO_5	29.88	x	—	30.51	7	—	53.52	4	211

Three strongest powder diffraction lines from Cu Kα line radiation
column "I": x for strongest line (100%); others x 10%

Just half an hour of post annealing at 850 °C converts majority of the film to the 1-2-3 phase which is believed to be influenced by microscopic chemical homogeneity of the film. Further annealing results in further decrease of the non-superconducting phases, and development of a higher degree of c-axis preferential orientation which is clearly indicated by the increasing ratio between 002 peak near 15° and 103/110 peak near 33°.

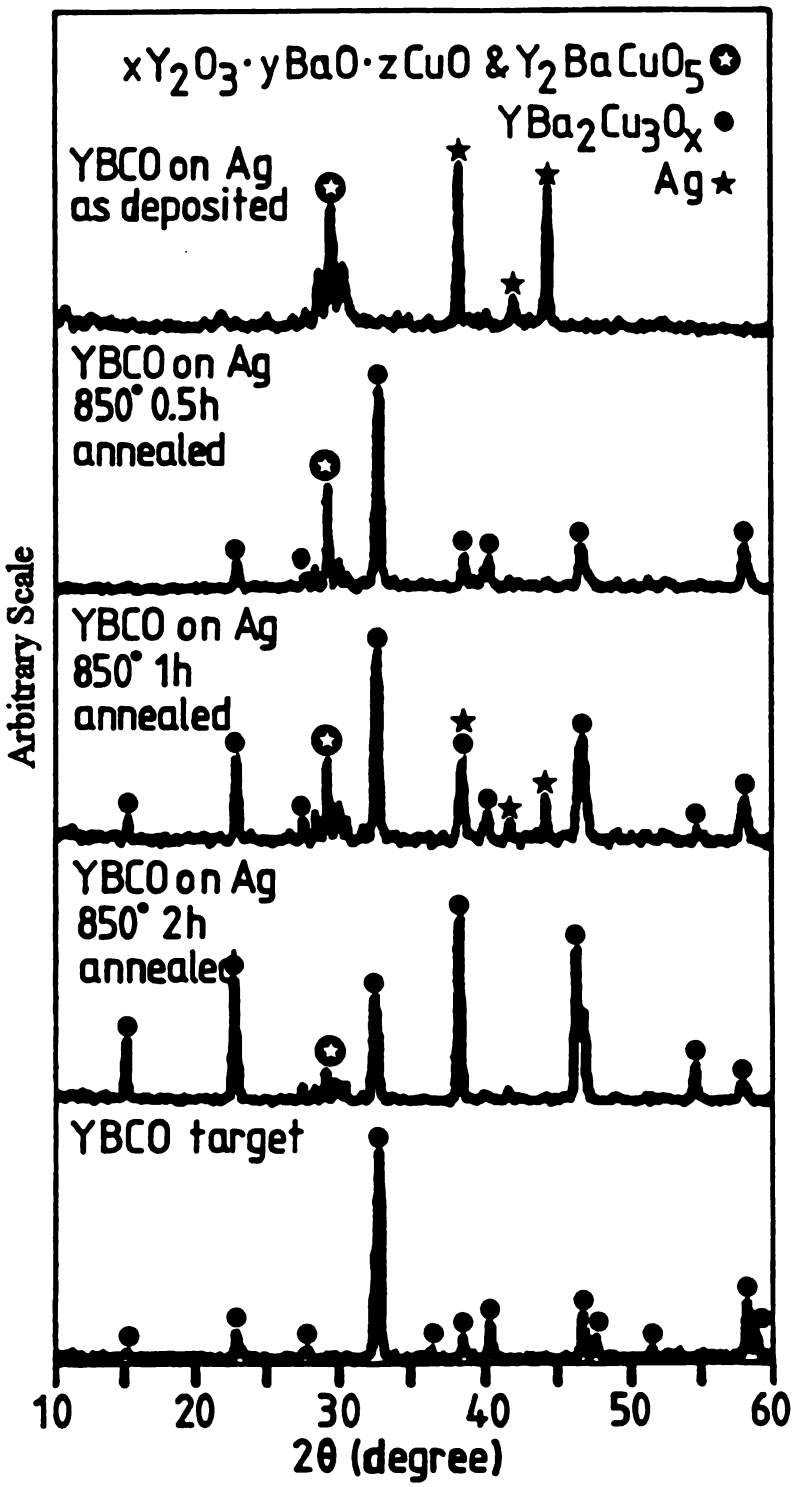

Figure 54. XRD patterns of YBCO films deposited on silver substrates

As-deposited films on (001)YSZ and (001)YSZ with a 0.2 mm silver buffer layer show similar results as those for the films on silver substrate. However, after post annealing, a strong film/substrate reaction was observed on films deposited on (001)YSZ, which is indicated by an additional peak of $xBaOyZrO_2$ near 43°, Figure 55. It is found that 0.2 mm of silver buffer layer effectively minimizes degradation caused by film/substrate reaction of (001)YSZ substrate, Figure 55.

4.3.3.5 Microstructure of IBPLD Films

Typical microstructure of YBCO as deposited film on (001) YSZ, produced by ion-beam laser vapor deposition process with 0.25ms laser pulse and 40 J/cm^2 energy density is shown in Figure 56. A similar microstructure was also observed for the as-deposited on silver; however, a quite different microstructure was found for the as deposited film on (001) YSZ with silver buffer layer, Figure 57. Figure 58 shows microstructure of YBCO films deposited on silver, after high temperature annealing.

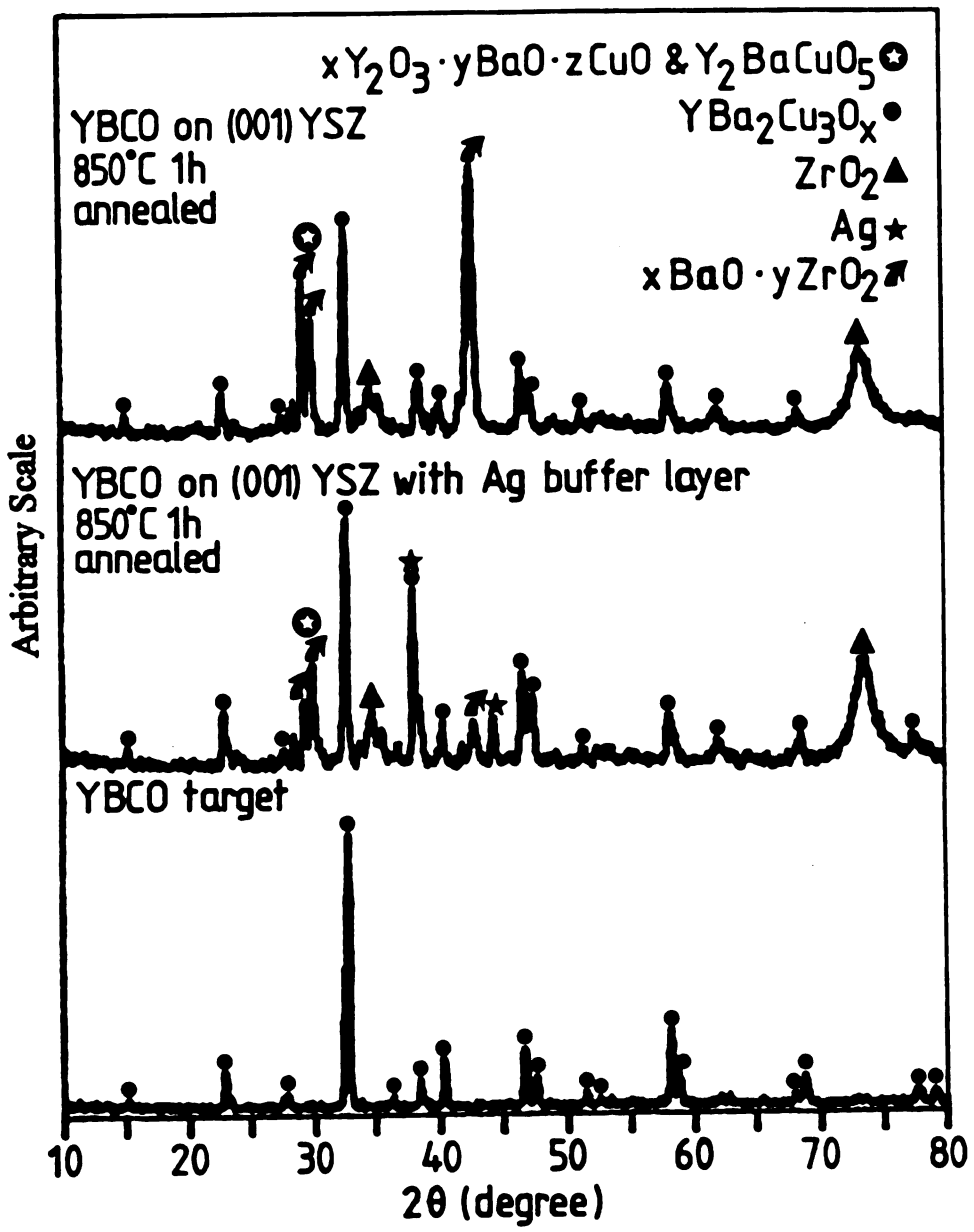

Figure 55. XRD patterns of YBCO films deposited on a (001) YSZ substrate and a (001) YSZ substrate with an Ag buffer layer

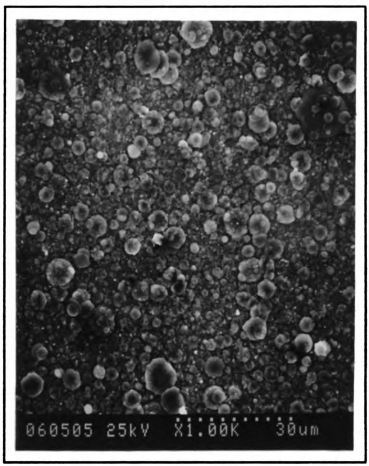

Figure 56. Scanning electron micrograph of an as-deposited IBPLD film on (001) YSZ (0.25 ms laser pulse with 40 J/cm^2 pulse-energy density)

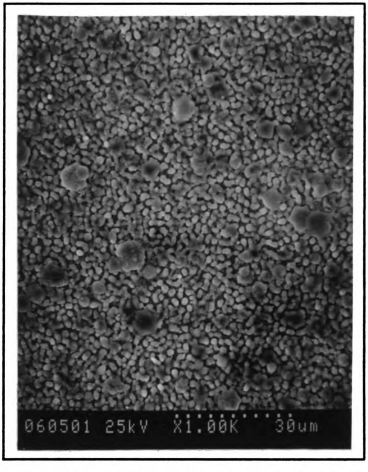

Figure 57. Scanning electron micrograph of an as-deposited IBPLD film on (001) YSZ with silver buffer layer (0.25 ms laser pulse with 40 J/cm^2 pulse-energy density)

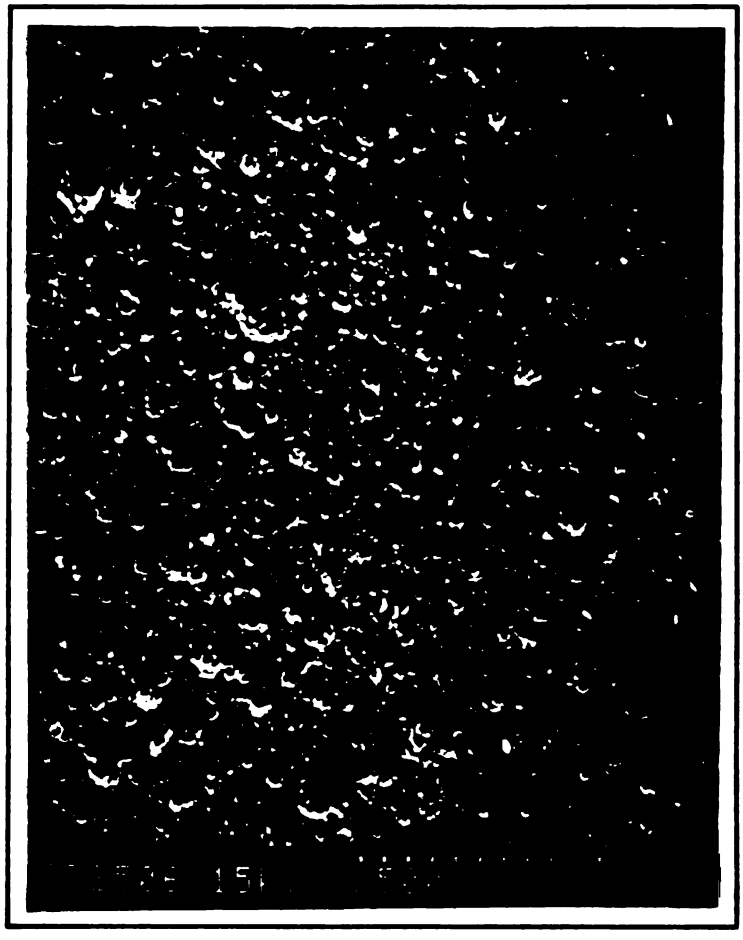

Figure 58. Scanning electron micrograph of a 850 °C, 1 hour, annealed IBPLD film on silver (0.25 ms laser pulse with 40 J/cm^2 pulse-energy density)

4.3.4 VTE/ms-PLD Multi-Layer Ag/Ag-Doped YBCO Tapes

4.3.4.1 Effect of Ag Addition to YBCO Target

In IBPLD process, a zigzag scanning pattern of the target with a x-y target manipulator reduces target overheating problem and produces YBCO films with correct compositions. However, for a prolong deposition without frequent re-surfacing, the pulse energy density is restricted to about 60 J/cm^2 which limits the deposition rate below 10 nm/s.

The target overheating and severe melting problems were completely resolved by the combination of silver doped target and zigzag target scanning pattern. This improvement is believed to be caused by higher densities, higher thermal conductivities and better mechanical strengths of the silver doped YBCO targets.

The density of silver doped YBCO target increased from about 77% theoretical density, for the pure YBCO target, to about 84% theoretical density, assuming the rule of mixture, for both 15 wt% and 23 wt% Ag-doped YBCO.

The flexural strengths of YBCO and 15% Ag-doped YBCO targets, determined by four-point bending, are 12.38 ± 2.39 and 30.51 ± 0.75 MPa, respectively. Both the strength and the scattering of strength data are greatly improved by the silver addition.

As a result, continuous deposition rate as high as 50 nm/s was attained with only 15% silver addition.

Picture of both YBCO and 23% silver doped YBCO targets after ms-PLD processes, with a moderate pulse energy density, shows clear improvement in resistance to surface roughening by silver doping, Figure 59. The deposition parameters used were 2 pps pulse-rate, 1 mm/s scan-rate, 1 mm feed per-scan, and 60 J/cm^2 pulse energy density.

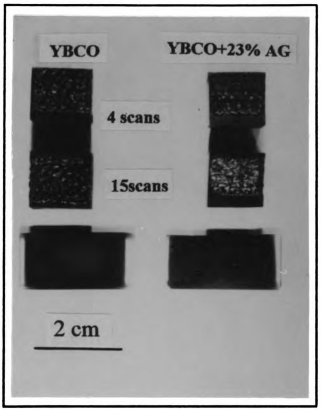

Figure 59. YBCO and 23% Ag-doped YBCO targets after 4 or 15 laser scans

Figure 60 shows scanning electron micrographs of target surfaces after four laser scans under same conditions. YBCO target shows severe cavitation and cracking while 23 wt% silver doped YBCO appears to be flat and smooth.

Cross section micrographs of the same YBCO target, Figure 61 (b), shows an almost delaminated resolidified layer of approximately 30 μm thickness. On the other hand, the 23 wt% silver doped target only shows a very thin and continuous resolidified layer, Figure 61(a). These differences are even more evident after fifteen laser scans under the same conditions, Figure 62.

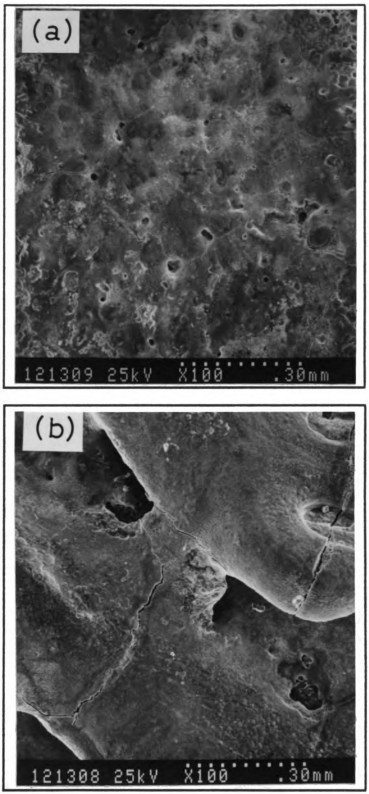

Figure 60. SEM micrographs taken from surfaces of (a) 23% Ag-doped YBCO target and (b) YBCO target after four laser scans

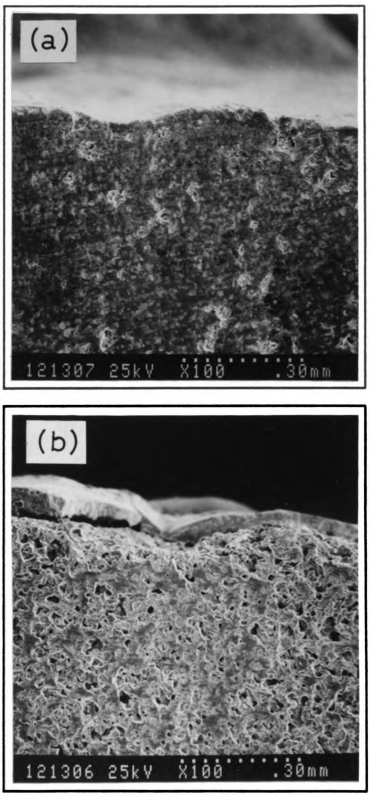

Figure 61. Cross section SEM micrographs of (a) 23% Ag-doped YBCO and (b) YBCO targets after four laser scans

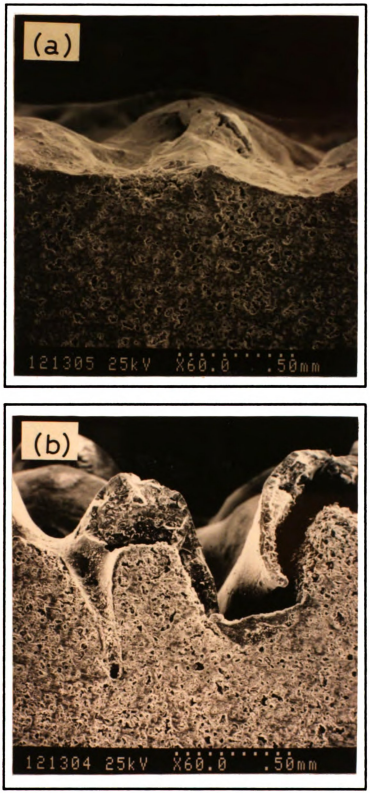

Figure 62. Cross section SEM micrographs of (a) 23% Ag-doped YBCO and (b) YBCO targets after fifteen laser scans

Similar improvement in the resistance to high power laser pulses is also found with only 15wt% of silver addition to YBCO target. Due to the superior properties of silver doped YBCO targets, 15% silver doped YBCO targets were used for deposition process.

4.3.4.2 Adhesion between Ag Layer and Ag-Doped YBCO Layer

Figure 63 shows a target after 35 minutes of continuous deposition process and two Ag/Ag-doped YBCO multi-layered thick tapes with approximately 8 microns of Ag-doped YBCO top layers. One of the films has been bent to show good adhesion between the Ag-doped YBCO layer and the silver, no delamination were observed.

The as-deposited Ag-doped YBCO layers appear to be smooth and dense with good adhesion that can be seen from SEM micrographs taken from surface of an as-deposited film, Figure 64 (a), and fractured cross section of a silver doped YBCO/Ag film, Figure 64 (b).

Figure 65 shows a typical optical microstructure of an annealed 15 wt% Ag-doped YBCO film after polishing. The film appears to be very dense, and most of the silver content forms uniformly distributed micron size particles.

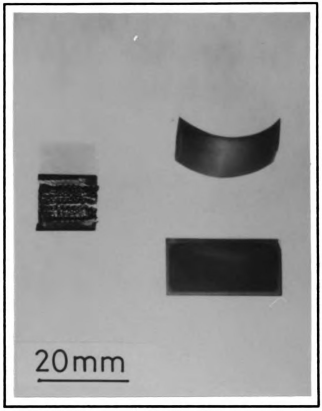

Figure 63. A 15 wt% Ag-doped target after 35 minutes of laser irradiation, and two Ag/Ag-doped YBCO multi-layered thick tapes with approximate 8 microns of Ag-doped YBCO top layers

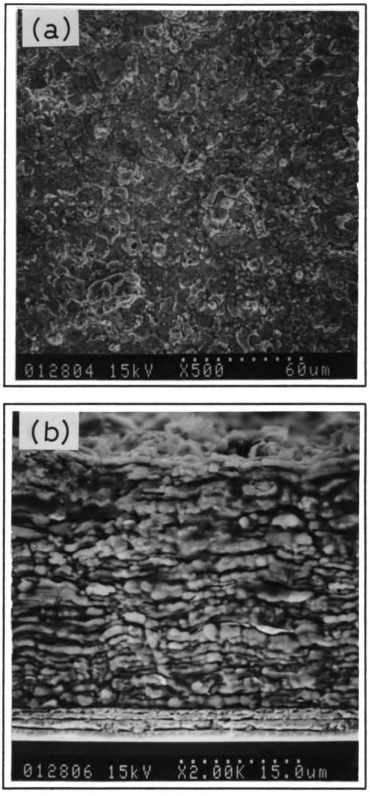

Figure 64. SEM micrographs from (a) surface of an as deposited film, and (b) fractured cross section of an Ag-doped YBCO/Ag film

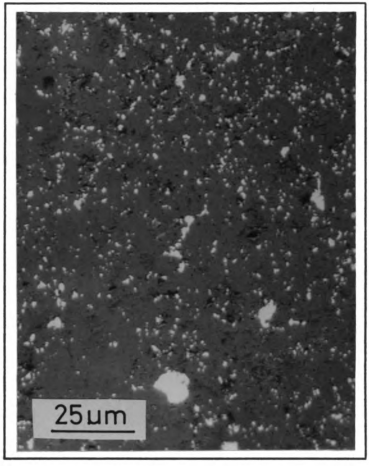

Figure 65. Typical optical microstructure of an annealed, 15 wt% Ag-doped YBCO film

4.3.4.3 Effect of Peak Power Density on the Composition of Ag-Doped YBCO Layers

EDS data collected from Ag-doped YBCO layers, deposited under different conditions, are shown in Figure 66 along with an EDS spectrum from a silver doped target for comparison. Peak powder density is the most important laser parameter in ms-PLD process. Samples produced with the same pulse energy density but different pulse duration, hence different peak power density, have quite different compositions. Samples deposited at peak power density of about 0.9 MW/cm^2 have compositions very close to that of the target. On the other hand, samples with lower peak powder densities, e.g. about 0.2 MW/cm^2, show yttrium and copper depletion.

4.3.4.4 X-ray Diffraction Analysis of Ag-Doped YBCO Layers

Typical data on XRD study of as-deposited and annealed Ag-doped YBCO layers are summarized in Figure 67. The XRD pattern of as deposited Ag-doped YBCO layers show very broad silver peaks and a very broad peaks around 30° of 2-θ similar to as-deposited IBPLD films. The as-deposited layers are more amorphous than as-deposited IBPLD films due to much lower substrate temperature and the absence of high energy oxygen ion-beam.

Just 20 minutes of post processing annealing at 855 °C, converts majority of the layer to 1-2-3 phase. This is believed to be caused by microscopic chemical homogeneity of layers. Further annealing at 905 °C for 30 minutes results in a decrease of the non-superconducting phases. Higher degree of c-axis preferential orientation, indicated by the increasing intensity of the 002 peak near 15°, is obtained by an additional 30 minutes annealing at 905 °C; however the undesirable second phase also develops during prolong annealing.

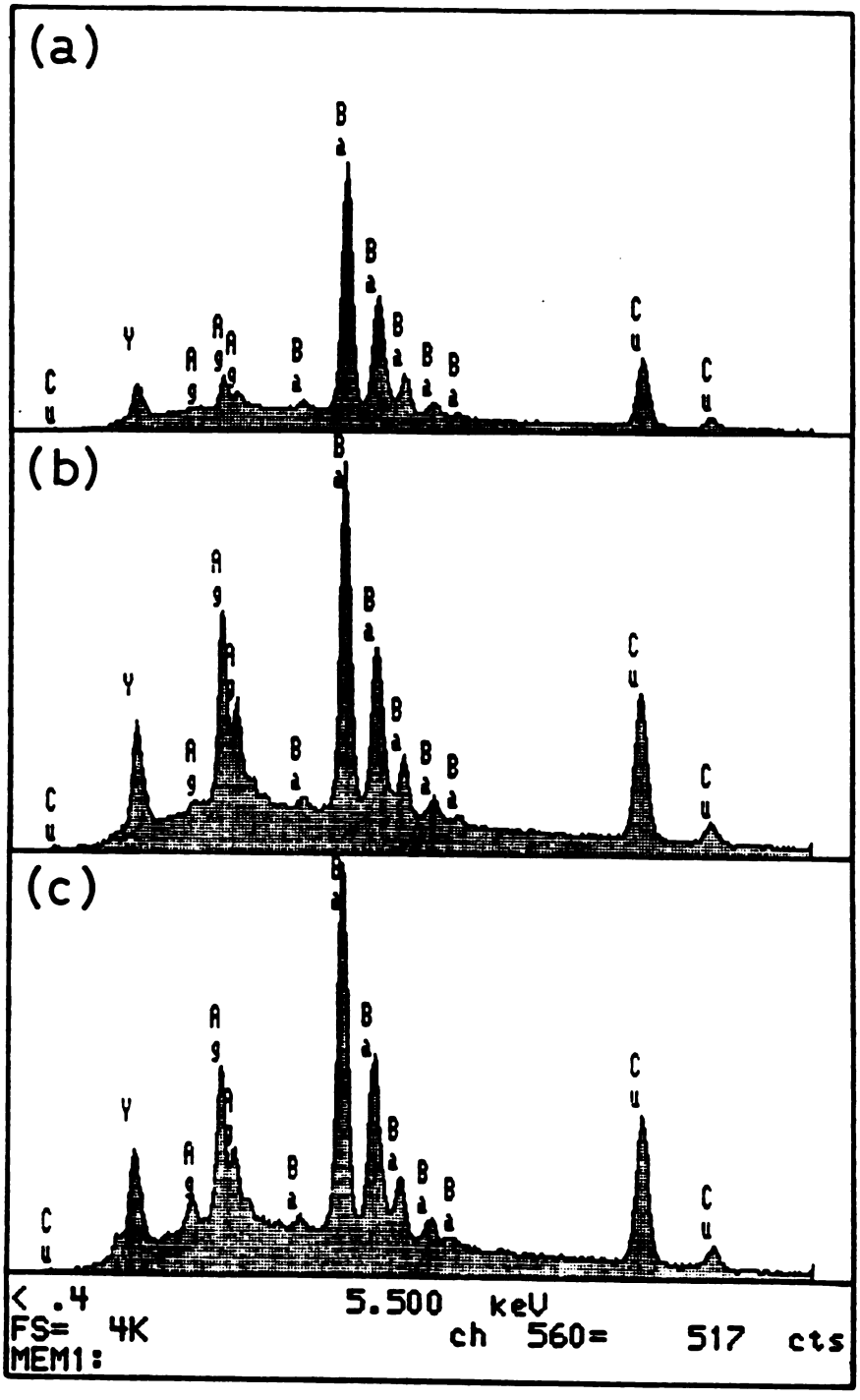

Figure 66. EDS spectra from (a) 15% Ag-doped YBCO layer deposited with 2.5 ms laser pulses, 270 J/cm^2 energy density and about 0.2 MW/cm^2 peak power density, (b) 15% Ag-doped YBCO layer deposited with 0.6 ms laser pulses, 270 J/cm^2 energy density and about 0.9 MW/cm^2 peak power density, and (c) 15% Ag-doped YBCO target

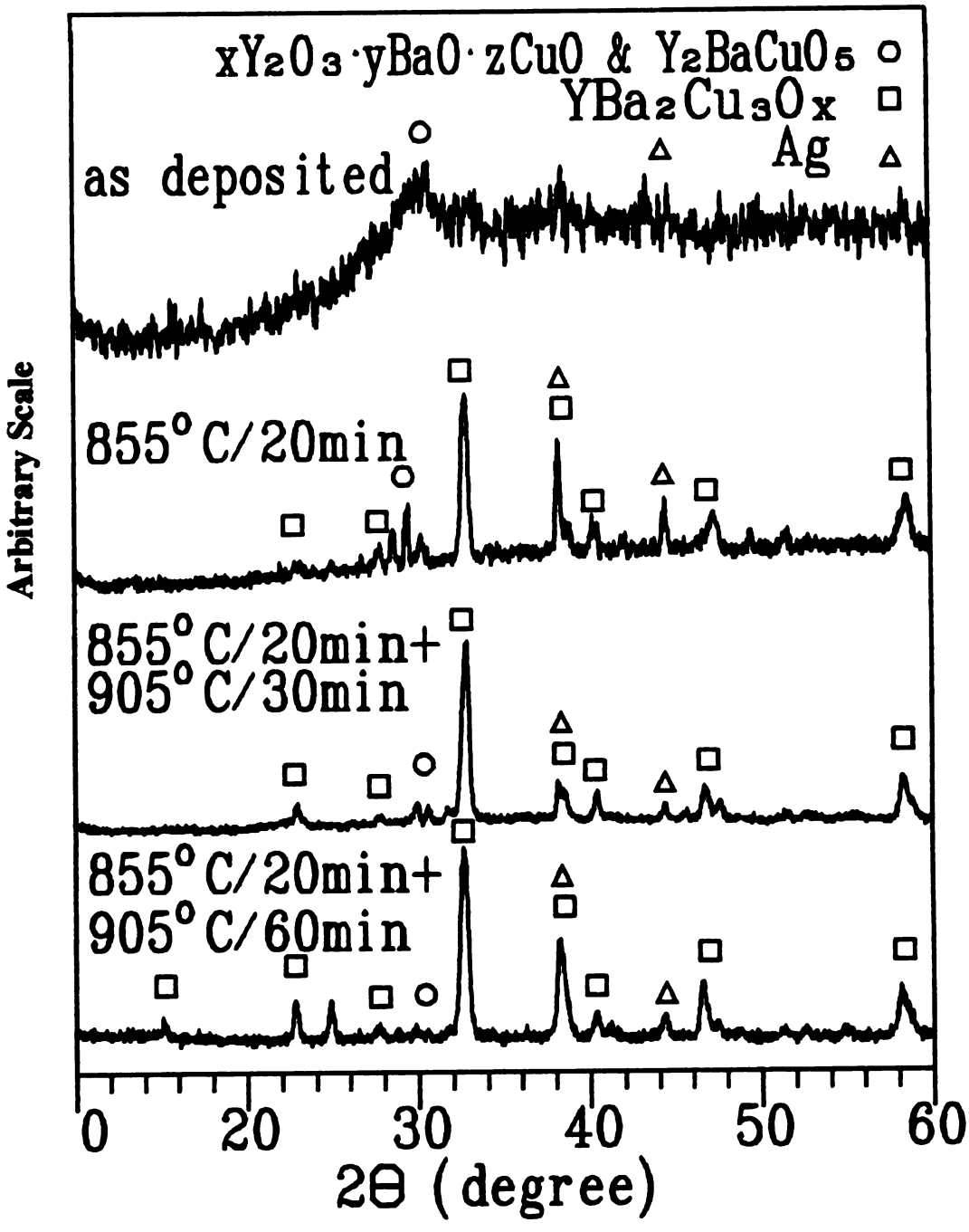

Figure 67. Typical x-ray diffraction patterns taken from as-deposited and annealed 15% Ag-doped YBCO layers

4.3.4.5 Critical Temperature of Ag/Ag-doped YBCO Tapes

Critical temperature (T_c) of the annealed tapes was measured using a standard four-probe technique with an auto-balance bridge. Figure 68 is a typical resistant-temperature curve of Ag/Ag-doped YBCO tapes annealed at 855 °C for 20 minutes and 905 °C for 30 minutes respectively. A metallic behavior (positive temperature coefficient of resistivity) is observed in the normal state followed by a broad transition, and a T_c of about 77 K.

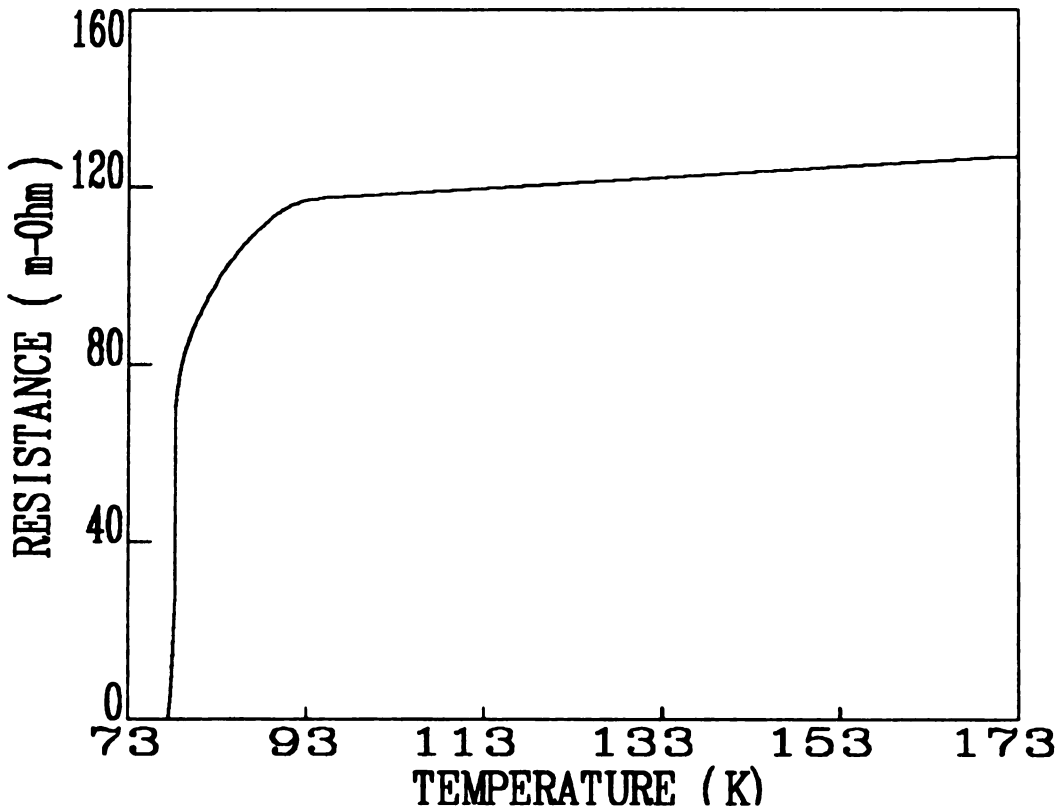

Figure 68. Typical resistant-temperature curve of an annealed Ag/Ag-doped YBCO tape

5. SUMMARY

5.1 Factors Which Affect Processing of Bulk YBCO Superconductors

The preparation of bulk YBCO superconductors, through conventional solid-state processes, has been systematically studied. Careful wet grinding and firm hand packing were found to greatly accelerate the calcination and formation of the YBCO compound. Furthermore, impurity less than 0.1% in the starting materials can significantly retard the formation of the YBCO compound.

High green density is important in obtaining high quality bulk superconductors. High green density can be obtained using a well crystallized YBCO powder with a shiny black appearance.

5.2 Laser Calcination of Pb-Doped BSCCO

The problem associated with sluggish kinetics of formation of 2223 high T_c phase in Pb-doped Bi-Sr-Ca-Cu-O system was investigated.

A laser calcination process for Pb-doped Bi-Sr-Ca-Cu-O (BSCCO) material was established that reduces total processing time of obtaining a near-single phase high T_c material to about 100 hours. The high T_c phase was found to form via a different kinetic path in laser calcined sample compared with the conventionally processed sample.

The onset critical temperature of the laser calcined sample was found to be about 110 K. However, the zero resistance temperature was about 98 K.

5.3 Ion-Beam Assisted Millisecond PLD

An ion beam assisted millisecond pulsed laser vapor deposition process was developed to fabricate $YBa_2Cu_3O_x$ (YBCO) high T_c superconductor films.

Target overheating problem is greatly reduced by using a zigzag scanning pattern of the target with a x-y target manipulator. With the x-y target manipulator, peak power density up to 0.16 MW/cm^2 can be attained to deposit YBCO film with a composition close to the target composition. Large uniform YBCO film was successfully deposited on fused silica substrate.

High energy oxygen ion beam used in this process is found not only to replenish oxygen, but also to help propagating vapor species onto the substrate.

As-deposited films are composed of various compounds of Y_2O_3, BaO and CuO as well as Y_2BaCuO_5. Due to microscopic chemical homogeneity of films, films with majority of 1-2-3 phase are formed by just half an hour of post annealing at 850 °C.

The silver buffer layer is found to effectively minimize degradation caused by film/substrate reaction of (001)YSZ substrates during post annealing.

5.4 VTE/ms-PLD Ag/Ag-Doped YBCO Tapes

A new process, combining ms-PLD and vacuum thermal evaporation (VTE) techniques, was developed to produce a multi-layer Ag doped YBCO/Ag thick film.

The target overheating and severe melting problems were completely resolved by the combination of silver doped target and a zigzag target scanning pattern. This improvement is believed to be caused by higher densities, higher thermal conductivities and better mechanical strengths of the silver doped YBCO targets.

As a result, continuous deposition rate as high as 50 nm/s was attained with only 15% silver addition. Ag doped YBCO layer and the silver shows good adhesion, no delamination were observed even after bending.

Peak power density is found to be the most important laser parameter in ms-PLD process. Samples produced with high peak power density have compositions very close to that of the target. On the other hand, samples produced with lower peak powder densities show yttrium and copper depletion.

The ms-PLD processed Ag-doped YBCO tapes show a metallic temperature dependence of resistance in the normal state and a broad transition to a T_c of about 77 K.

APPENDIX

APPENDIX

Addendum to the review of Selected Theories of Superconductivity

List of Symbols

H	magnetic field strength	E_F	Fermi energy
B	magnetic flux density	v_F	velocity of electrons at E_F
A	magnetic potential field	F_s	superconducting state free energy density
j	current density	F_n	normal state free energy density
T	temperature	Θ	Debye temperature
T_C	critical temperature	ω_D	Debye frequency
e	charge of an electron	U	electron-phonon interaction matrix elements
m	mass of an electron	E_g	superconducting energy gap
C	speed of light in vacuum	λ	penetration depth
k_B	Boltzmann's constant	λ_L	London penetration depth
h	Planck's constant	ξ	coherence length
$\hbar$	$h / 2\pi$	ξ_0	intrinsic coherence length
e'	charge of superconducting charge carrier	κ	Ginzburg-Landau parameter ($\kappa = \lambda/\xi$)
m'	mass of superconducting charge carrier	Φ	total magnetic flux
n	conduction electron density	Φ_0	fluxoid
n_s	superconducting electron density	H_C	thermodynamic critical field
n'_s	density of superconducting charge carrier	H_{C1}	lower critical field
N_F	normal state electron density at the Fermi energy	H_{C2}	upper critical field

A.1 Two-Fluid Model:

A.1.1 Free Energy in Superconducting State

Let n = N/V be the density of all conduction electrons, where N and V are the total number of conduction electrons and volume of the sample. n_s and n_n denotes the superconducting and normal-state electron densities, respectively. The two fluid model assumes a free energy of the conduction electrons in superconducting-state as

$$\boxed{F_s(x,T) = x^{1/2} f_n(T) + (1-x) f_s(T)} \; [56],$$

where $x = n_n/n$ is the fraction of normal state electrons.
Free energy of normal state electrons is set to be

$$f_n(T) = -\gamma T^2/2$$

in order to get a linear electron specific heat of normal -state, i.e.

$$c_{en} = -T\frac{\partial^2 f_n(T)}{\partial T^2} = \gamma T.$$

Free energy of superconducting electrons is set to be equal to the superconducting condensation energy -β, i.e. $f_s(T) = -\beta$. Since x = 0 at 0 K, i.e. all electrons are in condensed state, $F_s(0,0) = -\beta$

A.1.2 Temperature Dependence of Superconducting Electron Density

The equilibrium fraction of normal-state and superconducting electron at temperature T can be obtained by setting $(\partial F/\partial x)_T = 0$.

$$\left(\frac{\partial F_s}{\partial x}\right)_T = \frac{1}{2}\left(-\frac{\gamma T^2}{2}\right)x^{-1/2} + (-1)(-\beta) = -\frac{\gamma T^2}{4}x^{-1/2} + \beta = 0$$

$x_{equil} = \frac{\gamma^2 T^4}{16\beta^2} \equiv \left(\frac{T}{T_c}\right)^4$, where $T_c{}^2 = 4\beta/\gamma$. Therefore,

$\boxed{n_s/n = 1 - (T/T_c)^4}$; therefore, $n_s(T_c) = 0$ and $n_s(0) = n$.

A.1.3 Temperature Dependence of Thermodynamic Critical Field

The parameters β and γ can be derived using the property that the free energy difference between normal and superconducting states is equal to the magnetic energy at the thermodynamic critical field, i.e.

$$F_n - F_s = \frac{H_c^2}{8\pi} \text{ and } F_n = f_n = -\gamma T^2/2$$

$$\begin{aligned} F_n - F_s &= f_n - \left\{x^{1/2} f_n + (1-x) f_s\right\} \\ &= \left\{1 - (T/T_c)^2\right\}\left(-\gamma T^2/2\right) - \left\{1 - (T/T_c)^4\right\}(-\beta) \\ &= \beta\left\{-\frac{\gamma}{2\beta}\left(T^2 - T^4/T_c^2\right) + 1 - (T/T_c)^4\right\} \\ &= \beta\left\{-\left(2/T_c^2\right)\left(T^2 - T^4/T_c^2\right) + 1 - (T/T_c)^4\right\} \\ &= \beta\left\{1 - (T/T_c)^2\right\}^2 = \frac{H_c^2}{8\pi} \end{aligned}$$

$$\boxed{H_c(T) = (8\pi\beta)^{1/2}\left\{1 - (T/T_c)^2\right\} = H_c(0)\left\{1 - (T/T_c)^2\right\}};$$

therefore, $\boxed{\beta = \left(\frac{H_c^2}{8\pi}\right)_{T=0} = \frac{H_c^2(0)}{8\pi}}$.

A.1.4 Electron Specific Heat

Consider the Helmholtz free energy, F(V,T) = E - TS, the following relations are true for any reversible process:

$dF = -PdV - SdT$; $(\partial F/\partial T)_V = -S$;

$dS = dQ_R/T$; $C_v = (dQ/dT)_V = (dE/dT)_V$;

$(C_v dT/T)_V = (dQ/T)_V = dS$. Therefore,

$$\boxed{c_v = T(dS/dT) = T\frac{d}{dT}(-\partial F/\partial T)_V = -T\left(\partial^2 F/\partial T^2\right)_V}$$

The electron specific heat in normal and superconducting states, C_{en} and C_{es}, can be obtained by $-T\left(\partial^2 F_n/\partial T^2\right)$ and $-T\left(\partial^2 F_s/\partial T^2\right)$, respectively.

$$c_{en} = -T\frac{\partial^2 F_n}{\partial T^2} = -T\frac{\partial}{\partial T}\left[\frac{\partial}{\partial T}\left(\frac{-\gamma T^2}{2}\right)\right] = -T\frac{\partial}{\partial T}(-\gamma T) = \gamma T$$

$$F_s = x^{1/2} f_n(T) + (1-x) f_s(T) = \left(\frac{T}{T_c}\right)^2\left(\frac{-\gamma T^2}{2}\right) + \left\{1-\left(\frac{T}{T_c}\right)\right\}^4(-\beta)$$

$$= \left(-\frac{\gamma}{2T_c^2} + \frac{\beta}{T_c^4}\right)T^4 - \beta = \left\{-\frac{\gamma}{2T_c^2} + \frac{\beta}{(4\beta/\gamma)T_c^2}\right\}T^4 - \beta = -\frac{\gamma}{4T_c^2}T^4 - \beta$$

$$\boxed{c_{es} = -T\frac{\partial^2 F_s}{\partial T^2} = 3\gamma T_c\left(\frac{T}{T_c}\right)^3}$$

$$(c_{es}/c_{en})_{T_c} = \left\{3\gamma T_c(T_c/T_c)^3\right\}/(\gamma T_c) = 3$$

A.2 London Equation

The London equation is an important phenomenological theory based on the two fluid model to try to understand the Meissner effect. Recall the result of the two fluid model, the density of superconducting electrons is

$$\frac{n_s(T)}{n} = 1 - (T/T_c)^4, \quad n_s(T_c) = 0, \text{ and } n_s(0) = n \ .$$

The current due to the superconducting electrons is $\mathbf{j} = -ev_s n_s$ where $\mathbf{v_s}$ is the velocity of superconducting electrons which can be obtained from Newton's law

$\mathbf{F} = m(dv/dt) = -e\mathbf{E}$. Thus,

$$\frac{\partial \mathbf{j}}{\partial t} = -en_s\frac{\partial \mathbf{v}}{\partial t} = \left[\frac{e^2 n_s}{m}\right]\mathbf{E}$$

substituting $\mathbf{E}$ above into Maxwell's equation, $\nabla\times\mathbf{E} = -\frac{1}{C}(\partial\mathbf{B}/\partial t)$, yields

$$\frac{\partial}{\partial t}\left(\frac{mC}{e^2 n_s}\nabla\times\mathbf{j} + \mathbf{B}\right) = 0 \ \textit{[56]}.$$

The Londons showed that the Meissner effect can be account for by restricting the solutions to those satisfying

$\boxed{\mathbf{B} = -\frac{mC}{e^2 n_s}\nabla\times\mathbf{j}}$, which is called the London equation*[55,56]*.

A.2.1 London Penetration Depth

Another form of the London equation can be obtained by applying Maxwell's equations, $\nabla\times\mathbf{B} = (4\pi/C)\mathbf{j}$ and $\nabla\cdot\mathbf{B} = 0$, and the vector identity, $\nabla \times (\nabla \times \mathbf{B}) = \nabla(\nabla\cdot\mathbf{B}) - \nabla^2\mathbf{B}$ to the above equation that yields*[55,56]*

$$\mathbf{B} = \frac{mC}{e^2 n_s}\nabla \times \left(\frac{C}{4\pi}\nabla \times \mathbf{B}\right) = -\frac{mC^2}{4\pi n_s e^2}\nabla^2 \mathbf{B} \text{ or } \boxed{\nabla^2 \mathbf{B} = \mathbf{B} / \lambda_L^2},$$

where λ_L is the London penetration depth defined as

$$\boxed{\lambda_L^2 \equiv mC^2 / 4\pi n_s e^2}.$$

Yet, the other form of the London equation is obtained by taking curl of both sides of the first form of London equation and applying the physical boundary $\nabla \bullet \mathbf{j} = 0$, that yields*[56]*

$$\nabla \times \mathbf{B} = \left(\frac{4\pi}{C}\right)\mathbf{j} = -\frac{mC}{e^2 n_s}\nabla \times \nabla \times \mathbf{j} = -\frac{mC}{e^2 n_s}\left[\nabla(\nabla \cdot \mathbf{j}) - \nabla^2 \mathbf{j}\right] \text{ or}$$

$$\boxed{\nabla^2 \mathbf{j} = \mathbf{j} / \lambda_L^2}.$$

A.2.2 Exponential Decay of the Magnetic Field **B** and Supercurrent Density **j**

$\nabla^2 \mathbf{B} = \mathbf{B} / \lambda_L^2$ and $\nabla^2 \mathbf{j} = \mathbf{j} / \lambda_L^2$ indicate exponential decay of the magnetic field and supercurrent from the free surface into a superconductor with a characteristic length equal to the London penetration depth λ_L.

For example, let the free surface of the superconductor to be perpendicular to the x axis with positive x in the superconductor, and let the applied magnetic field parallel to positive z direction and the supercurrent in the positive y direction. Solutions for the magnetic field and supercurrent density are*[56]*

$\boxed{B_Z = B_Z(0)\exp(-x/\lambda_L)}$ and $\boxed{j_y = j_y(0)\exp(-x/\lambda_L)}$, respectively.

A.2.3 Temperature Dependence of the London Penetration Depth

Temperature dependence of the London penetration depth can be obtained by adopting the temperature dependence of (n_s/n) from the two-fluid model*[56]*.

$$\lambda_L(T) = \left(mC^2/4\pi n_s e^2\right)^{1/2} = \left\{\left(mC^2/4\pi ne^2\right)/\left[1-(T/T_c)^4\right]\right\}^{1/2}$$

$$\boxed{\lambda_L(T) = \lambda_L(0)\left[1-(T/T_c)^4\right]^{-1/2}}$$

A.2.4 Magnetic Potential Field A and London Rigidity

The London equation can also be written in terms of a vector potential **A**, which will be used in discussing Ginzburg-Landau theory, such that $\mathbf{B} = \nabla\times\mathbf{A}$. The first form of London equation can be rewrite in terms of λ_L as

$$\nabla\times\mathbf{j} = -\frac{e^2 n_s}{mC}\mathbf{B} = -\frac{C}{4\pi\lambda_L^2}\mathbf{B} = -\frac{C}{4\pi\lambda_L^2}\nabla\times\mathbf{A} \quad \text{or} \quad \boxed{\mathbf{j} = -\frac{C}{4\pi\lambda_L^2}\mathbf{A}}.$$

Since $\mathbf{j} \propto \mathbf{A}$, we have $\nabla\cdot\mathbf{A} = 0$ and $\mathbf{A}_n = 0$, where $\mathbf{A}_n$ is component of **A** perpendicular to external surface, in order to satisfying physical boundary condition $\nabla\cdot\mathbf{j} = 0$ and $\mathbf{j}_n = 0$.

This equation can also be obtained in a more intuitive way by considering the canonical momentum $\mathbf{P} = m\mathbf{v} + (-e\mathbf{A})/C$. London proposed a quantum mechanical theory that if the ground state wave function is unchanged by the application of the magnetic field, i.e. $\Psi = \Psi_0$ so-called London rigidity, the net moment **P** should be zero. The London equation for the supercurrent density follows automatically*[56,58]*.

$$\mathbf{j}_s = -n_s e\mathbf{v}_s = -\frac{n_s e}{m}\left(\mathbf{P} + \frac{e\mathbf{A}}{C}\right)_0 = -\frac{n_s e^2}{mC}\mathbf{A} = -\frac{C}{4\pi\lambda_L^2}\mathbf{A}$$

$\lambda_L(0) = \left(mC^2/4\pi ne^2\right)^{1/2}$ or in the SI units

$$\lambda_L(0) = \left(\varepsilon_0 mC^2/ ne^2\right)^{1/2}$$

$$= \frac{\left(10^7/4\pi C^2\right)\left(\text{Coul.}^2/\text{N}\cdot\text{m}^2\right)\cdot 9.110\times10^{-31}(\text{kg})\cdot C^2\left(\text{m}^2/5^2\right)}{n\left(\text{m}^{-3}\right)\cdot\left(1.602\times10^{-19}\right)^2\left(\text{Coul.}^2\right)}$$

$$= n^{-1/2}\cdot 5.315\times10^6(\text{m}) = n^{-1/2}\cdot 5.315\times10^{15}(\text{nm})$$

For metallic elements the conducting electron concentration, n, is in the order of $10^{28} \sim 10^{29}\ \text{m}^{-3}$ *[55]*. The corresponding λ_L in the order of $10^1 \sim 10^2$ nm. Experimentally measured penetration depth in elemental superconductors tend to be larger than the calculated $\lambda_L(0)$ *[56]*.

For superconductor thin films in magnetic fields parallel to the film, the magnetic field will penetrate the whole film resulted in incomplete Meissner effect if the thickness of film is much small than the penetration depth. Very high critical field, H_C, is expected in this situation because the induced field is much less than the applied magnetic field, and the free energy expression,

$F_n - F_s = \frac{H_c^2}{8\pi} = \frac{B_a^2}{8\pi}$, no longer holds.

A.3 Ginzburg - Landau Theory (G.L. theory)

A.3.1 Ginzburg-Landau Order-Parameter

Ginzburg and Landau (1950) proposed a phenomenology theory of superconducting state in terms of a spatial varied order parameter $\Psi(r)$ which vanishes at a second-order phase transition temperature*[55,56,58]*. $\Psi(r)$ is related to local superconducting charge carrier density, n_s' .

$$\boxed{\Psi^*(r)\Psi(r) = |\Psi(r)|^2 = n_s'(r)}$$

A.3.2 Ginzburg - landau Free Energy

In the absence of magnetic field and spatial variation of order-parameter, the difference in free energy density is expressed in typical Landau form*[55]*.

$$F_s - F_n = -\alpha|\Psi|^2 + \frac{1}{2}\beta|\Psi|^4 = -\alpha n_s' + \frac{1}{2}\beta n_s'^2$$

Parameters α and β have properties that $\beta > 0$ for any second-order phase transition, $\alpha > 0$ for temperature below T_C and $\alpha < 0$ for temperature above T_C . This energy density difference exhibits a stable minimum at $\Psi = 0$ for $T > T_C$, i.e. the normal state. In the superconducting state, i.e. $T < T_C$, a double well potential appears with minima at $\Psi = \pm \Psi_0$*[56]*. Ψ_0, the ground state order parameter, where Ψ_0^2 defined as the $|\Psi|^2$ value in the interior of the sample without spatial variation of Ψ and magnetic field, can be obtained by setting $\partial(F_s - F_n)/\partial n_s' = 0$ *[56]*.

$$\boxed{\Psi_0^2 \equiv (n_s')_{\partial(F_s - F_n)/\partial n_s' = 0} = \alpha/\beta}$$

The equilibrium difference in free energy density can also be expressed in terms of the thermodynamic critical field H_c.

$$F_s - F_n = -\alpha(\alpha/\beta) + \tfrac{1}{2}\beta(\alpha/\beta)^2 = -\alpha^2/(2\beta) = -H_c^2/(8\pi)$$

An expression of the thermodynamic critical H_c in terms of α and β is obtained.

$$\boxed{Hc = \left(4\pi\alpha^2/\beta\right)^{1/2}}$$

Taking into account the spatial variation of Ψ and magnetic field yields*[55,56,58]*

$$\boxed{F_s(r) = F_n - \alpha|\Psi|^2 + \tfrac{1}{2}\beta|\Psi|^4 + \frac{1}{2m'}\left|\left(-i\hbar\nabla - \frac{e'A}{C}\right)\Psi\right|^2 - \int_0^{Ba} M\cdot dBa},$$

where m' and e' are mass and charge of the charge carrier. $(1/2m')|(-i\hbar\nabla - e'A/C)\Psi|^2$ term represents energy increase caused by spatial variation of Ψ, arising from kinetic momentum $-i\hbar\nabla$ and field momentum $-e'A/C$. The trailing term is the energy increase due to magnetic flux expulsion, i.e. Meissner effect, where $B_a = H$ is the applied field. Using the relation $B = H + 4\pi M$ and $B = 0$, due to complete Meissner effect, yields

$$-\int_0^{Ba} M\cdot dB_a = -\int_0^{Ba} -\frac{B_a}{4\pi}\cdot dBa = \frac{B_a^2}{8\pi} = \frac{H^2}{8\pi} \quad .$$

A.3.3 Ginzburg - Landau Equation

Minimizing F_s with respect to the order-parameter Ψ^* yields

$$\frac{\partial F_s}{\partial \Psi^*} = \frac{\partial}{\partial \Psi^*}\left\{F_n - \alpha\Psi\Psi^* + \frac{1}{2}\beta\Psi^2\Psi^{*2} + \frac{1}{2m'}\left(\left(-i\hbar\nabla - \frac{e'}{C}\mathbf{A}\right)\Psi \cdot \left(i\hbar\nabla - \frac{e'}{C}\mathbf{A}\right)\Psi^*\right) + \frac{H^2}{8\pi}\right\}$$

$$= -\alpha\Psi + \beta\Psi^2\Psi^* + \frac{1}{2m'}\left\{\left(-i\hbar\nabla - \frac{e'}{C}\mathbf{A}\right)\Psi \cdot \left(i\hbar\nabla - \frac{e'}{C}\mathbf{A}\right)\right\} = 0$$

$$\boxed{\left(-\alpha + \beta|\Psi|^2 + \frac{1}{2m'}\left|-i\hbar\nabla - \frac{e'}{C}\mathbf{A}\right|^2\right)\Psi = 0}$$

This is called the Ginzburg - Landau equation that resembles a schrödinger equation for Ψ with an energy eigenvalue α*[55,56]*.

A.3.4 Equivalence of London Equation and Penetration Depth

Minimizing F_s with respect to the potential **A** yields

$$\frac{\partial F_s}{\partial \mathbf{A}} = \frac{1}{2m'}\frac{\partial}{\partial \mathbf{A}}\left\{\left(-i\hbar\nabla\Psi - \frac{e'}{C}\mathbf{A}\Psi\right)\left(i\hbar\nabla\Psi^* - \frac{e'}{C}\mathbf{A}\Psi^*\right)\right\} + \frac{1}{8\pi}\frac{\partial H^2}{\partial \mathbf{A}}$$

$$= \frac{1}{2m'}\frac{\partial}{\partial \mathbf{A}}\left\{\hbar^2\nabla\Psi\nabla\Psi^* + \frac{i\hbar e'}{C}(\Psi^*\nabla\Psi - \Psi\nabla\Psi^*)\mathbf{A} + \left(\frac{e'}{C}\right)^2\Psi^*\Psi\mathbf{A}^2\right\} + \frac{1}{8\pi}\frac{\partial(\nabla\times\mathbf{A})}{\partial \mathbf{A}}$$

$$= \boxed{\frac{ie'\hbar}{2m'C}(\Psi^*\nabla\Psi - \Psi\nabla\Psi^*) + \frac{e'^2}{m'C^2}\Psi^*\Psi\mathbf{A} + \frac{1}{4\pi}\nabla\times(\nabla\times\mathbf{A}) = 0}.$$

This is another form of the Ginzburg-Landau equation. Combining this result with Maxwell's equation $\mathbf{j} = (C/4\pi)\nabla \times \mathbf{H}$, yields

$$\mathbf{j}_s(\mathbf{r}) = -\frac{ie'\hbar}{2m'}(\Psi^*\nabla\Psi - \Psi\nabla\Psi^*) - \frac{e'^2}{m'C}\Psi^*\Psi\mathbf{A}$$

This equation can be reformulated by using the expression $\Psi = \Psi_0 e^{i\theta(r)}$ from the BCS theory where Ψ_0 and θ are magnitude and phase of Ψ, respectively.

$$\mathbf{j}_s(r) = -\frac{ie'\hbar}{2m'}\left\{\Psi_0 e^{-i\theta}\nabla\left(\Psi_0 e^{i\theta}\right) - \Psi_0 e^{-i\theta}\nabla\left(\Psi_0 e^{-i\theta}\right)\right\} - \frac{e'^2}{m'C}|\Psi|^2\mathbf{A}$$

$$\mathbf{j}_s(r) = \frac{e'}{m'}|\Psi|^2\left(\hbar\nabla\theta - \frac{e'}{C}\mathbf{A}\right) = e'|\Psi|^2\mathbf{v}_s$$

In the London gauge θ is constant*[56]*, yields

$$\boxed{\mathbf{j}_s = -\frac{e'^2}{m'C}|\Psi|^2\mathbf{A} = -\frac{e'^2}{m'C}\Psi_0^2\mathbf{A}}\ .$$

This is in the same form as the London equation

$$\mathbf{j} = -\left\{C/\left(4\pi\lambda_L^2\right)\right\}\mathbf{A}\ .$$

A penetration depth λ similar to the London penetration depth can be defined*[55,56]*.

$$\boxed{\lambda = \left(\frac{m'C^2}{4\pi e'^2\Psi_0^2}\right)^{1/2} = \left(\frac{m'C^2\beta}{4\pi e'^2\alpha}\right)^{1/2}}$$

α and β can be expressed in terms of λ and H_C using this equation and $H_c = \left(4\pi\alpha^2/\beta\right)^{1/2}$.

$$\alpha = \frac{H_c^2}{4\pi\Psi_0^2} = \frac{e'^2}{m'C^2}H_c^2\lambda^2$$

$$\beta = \frac{\alpha}{\Psi_0^2} = \frac{H_c^2}{4\pi\Psi_0^4} = \frac{4\pi e'^4}{m'^2C^4}H_c^2\lambda^4$$

Using temperature dependencies from two-fluid model, i.e. $t = T/T_c$, $\Psi_0^2 \propto n_s/n \propto (1 - t^4)$ and $H_c \propto (1 - t)^2$, temperature dependencies of λ^2, α and β are obtained*[56]*.

$$\lambda^2 \propto \left(1 - t^4\right)^{-1} \approx (1 - t)^{-1}$$

$$\alpha \propto \left(1 - t^2\right) / \left(1 - t^4\right) \approx t - 1$$

$$\beta \propto \left(1 - t^2\right) / \left(1 - t^4\right)^2 \approx 1$$

A.3.5 Coherence Length

Consider the Ginzburg - Landau equation in one-dimension and in the absence of field, i.e. $\mathbf{A} = 0$.

$$-\frac{\hbar}{2m'}\frac{d^2\Psi}{dx^2} = \left(\alpha - \beta|\Psi|^2\right)\Psi$$

For temperature near T_c, i.e. $|\Psi|^2$ is small, the nonlinear term $\beta|\Psi|^2$ can be neglected.

$$\boxed{-\frac{\hbar}{2m'}\frac{d^2\Psi}{dx^2} = \alpha\Psi}$$

This equation has a wavelike solution $\boxed{\Psi(x) = \Psi_0 \exp(-ix/\xi)}$ where $\boxed{\xi \equiv \left[\hbar^2/(2m'\alpha)\right]^{1/2}}$ is the coherence length*[55,56]*.

An interesting special solution of the one-dimensional Ginzburg-Landau equation considering the nonlinear term $\beta|\Psi|^2$ can be expressed in terms of ξ defined above*[55]*.

$$\Psi(x) = (\alpha/\beta)^{1/2} \tanh\left\{x/\left(\sqrt{2}\,\xi\right)\right\}$$

This solution can be verified by direct substitution back to the original equation. Knowing $\frac{d}{dx}\tanh x = \operatorname{sech}^2 x$, $\frac{d}{dx}\sec x = -\operatorname{sech} x \cdot \tanh x$ and $\tanh^2 x + \operatorname{sech}^2 x = 1$.

$$-\frac{\hbar^2}{2m'}\frac{d^2}{dx^2}\left\{(\alpha/\beta)^{1/2}\tanh\left(\frac{x}{\sqrt{2}\,\xi}\right)\right\} = -\left(\frac{\alpha}{\beta}\right)^{1/2}\left(\frac{\hbar^2}{2m'}\right)\left\{\frac{d}{dx}\,\mathrm{sech}^2\left(\frac{x}{\sqrt{2}\,\xi}\right)\right\}\left(\frac{m\alpha}{\hbar^2}\right)^{1/2}$$

$$= -(\alpha/\beta)^{1/2}\left(\frac{\hbar^2}{2m}\right)\left(\frac{m\alpha}{\hbar^2}\right)\left\{-2\,\mathrm{sech}\left(\frac{x}{\sqrt{2}\,\xi}\right)^2\tanh\left(\frac{x}{\sqrt{2}\,\xi}\right)\right\} = \alpha\left\{\mathrm{sech}^2\left(\frac{x}{\sqrt{2}\,\xi}\right)\right\}\Psi(x)$$

$$= \alpha\left\{1 - \tanh^2\left(x/\sqrt{2}\,\xi\right)\right\}\Psi(x) = \alpha\Psi(x) - \beta|\Psi|^2\Psi(x)$$

Deep inside the superconductor, i.e. large x, $\Psi = \Psi_0 = (\alpha/\beta)^{1/2}$. The characteristic length ξ marks the extent of coherence of the superconducting wave-function into the normal region.

The dimensionless ratio between the two characteristic lengths λ and ξ, called Ginzburg - Landau parameter, defined as $\kappa \equiv \lambda / \xi$, is an important parameter in the theory of superconductivity.

$$\boxed{\kappa \equiv \frac{\lambda}{\xi} = \frac{m'C}{e'\hbar}\left(\frac{\beta}{2\pi}\right)^{1/2}}$$

A.3.6 Upper Critical Field and Type II Superconductor

Let the interface of the superconductor parallel to Y-Z plane and the magnetic field **B** parallel to Z axis, i.e. $\mathbf{B} = B_z\mathbf{k}$; therefore, the supercurrent and the potential field **A** will be in the Y direction, i.e. $\mathbf{A} = A_y\mathbf{j}$.

$$\mathbf{B} = B_z k = \nabla \times \mathbf{A} = \left(\frac{\partial A_z}{\partial y} - \frac{\partial A_y}{\partial z}\right)\mathbf{i} + \left(\frac{\partial A_x}{\partial z} - \frac{\partial A_z}{\partial x}\right)\mathbf{j} + \left(\frac{\partial A_y}{\partial x} - \frac{\partial A_x}{\partial y}\right)\mathbf{k}$$

$$B_z = \partial A_y/\partial x \quad \text{or} \quad xB_z = A_y \quad \text{or} \quad xB = A$$

At field near the upper critical field H_{c2} , because $|\Psi|^2$ is small, the Ginzburg - Landau equation can be linearized.

$$\frac{1}{2m'}\left(-i\hbar\nabla - \frac{e'}{C}\mathbf{A}\right)^2\Psi = \alpha\Psi$$

$$= \frac{1}{2m'}\left(-\hbar^2\nabla^2 + 2\frac{i\hbar e'}{C}\nabla\cdot\mathbf{A} + \left(\frac{e'}{C}\mathbf{A}\right)^2\right)\Psi$$

$$= \frac{1}{2m'}\left\{-\hbar^2\left(\frac{\partial^2}{\partial x^2} + \frac{\partial^2}{\partial y^2} + \frac{\partial^2}{\partial z^2}\right) + \frac{2i\hbar e'}{C}\left(\frac{\partial A_x}{\partial x} + \frac{\partial A_y}{\partial y} + \frac{\partial A_z}{\partial z}\right) + \left(\frac{e'B}{C}x\right)^2\right\}\Psi$$

$$= \frac{-\hbar^2}{2m'}\left(\frac{\partial^2}{\partial x^2} + \frac{\partial^2}{\partial z^2}\right)\Psi + \frac{1}{2m'}\left\{\left(i\hbar\frac{\partial}{\partial y}\right)^2 + \frac{2i\hbar e'}{C}Bx\frac{\partial}{\partial y} + \left(\frac{e'B}{C}x\right)^2\right\}\Psi$$

$$\boxed{-\frac{\hbar^2}{2m'}\left(\frac{\partial^2}{\partial x^2} + \frac{\partial^2}{\partial z^2}\right)\Psi + \frac{1}{2m'}\left(i\hbar\frac{\partial}{\partial y} + \frac{e'B}{C}x\right)^2\Psi = \alpha\Psi}$$

This is of the same form as the schrödinger equation of a free particle in a magnetic field*[55]*. We should look for a solution in the form $\Psi = \Phi(x)\exp\left\{i\left(k_y y + k_z z\right)\right\}$. Substituting this back to the equation yields*[55]*

$$\frac{1}{2m'}\left\{-\hbar^2\frac{d^2}{dx^2}+\left(\frac{e'B}{C}x-\hbar k_y\right)^2\right\}\Phi=\left(\alpha-\frac{\hbar^2k_z^2}{2m'}\right)\Phi$$

$$\left\{-\frac{\hbar^2}{2m'}\left(\frac{\partial^2}{\partial x^2}+\frac{\partial^2}{\partial z^2}\right)+\frac{1}{2m'}\left[\left(i\hbar\frac{\partial}{\partial y}\right)^2+\frac{2i\hbar e'}{C}Bx\frac{\partial}{\partial y}+\left(\frac{e'}{C}Bx\right)^2\right]\right\}\Phi(x)e^{i\left(k_yy+k_zz\right)}$$

$$=-\frac{\hbar^2}{2m'}\left\{e^{i\left(k_yy+k_zz\right)}\frac{d^2}{dx^2}\Phi+k_z^2e^{i\left(k_yy+k_zz\right)}\Phi\right\}$$

$$+\frac{1}{2m'}\left\{\hbar^2k_y^2e^{i\left(k_yy+k_zz\right)}\Phi-\frac{2\hbar e'}{C}k_yBxe^{i\left(k_yy+k_zz\right)}\Phi+\left(\frac{e'}{C}Bx\right)^2e^{i\left(k_yy+k_zz\right)}\Phi\right\}$$

$$=e^{i\left(k_yy+k_zz\right)}\frac{1}{2m'}\left\{-\hbar^2\frac{d^2}{dx^2}+\hbar^2k_z^2+\left(\frac{e'B}{C}x-\hbar k_y\right)^2\right\}\Phi\ .$$

By shifting the origin from $x = 0$ to $x = x_0 = -\hbar k_yC/(e'B)$, the x coordinate becomes $X = x - x_0$. Substituting to the above equation yields*[55]*

$$-\frac{\hbar^2}{2m'}\frac{d^2}{dX^2}\Phi+\frac{1}{2m'}\left(\frac{e'B}{C}\right)^2X^2\Phi=\left(\alpha-\frac{\hbar^2k_z^2}{2m'}\right)\Phi\ .$$

This equation is in the form of the schrödinger equation for the magnitude part, u(x), of an linear harmonic oscillator*[107]*.

$$-\frac{\hbar^2}{2m}\frac{d}{dx}u+\frac{1}{2}kx^2u=Eu$$

Under the boundary condition $u\rightarrow 0$ as $x\rightarrow\infty$, the energy eigenvalue E can only be in the form $E_n = (n+1/2)h\nu = (n + 1/2)\hbar\omega$, where $\omega = (k/m)^{1/2}$ is the angular frequency of the oscillator and n is any non-negative integer.

$$E_n=\alpha-\frac{\hbar^2k_z^2}{2m'}=\left(n+\frac{1}{2}\right)\hbar\left(\frac{e'B}{m'C}\right)$$

The maximum magnetic $B_{max} = H_{c2}$ is corresponding to n = 0*[55]*. Because the supercurrent and **A** is in the Y direction, k_z is zero.

$$H_{c2} = B_{max} = 2\alpha m'C/(e'\hbar)$$

This can be related to the thermodynamic critical field $H_c = \left(4\pi\alpha^2/\beta\right)^{1/2}$ by using the Ginzburg - Landau parameter $\kappa = \frac{m'C}{e'\hbar}\left(\frac{\beta}{2\pi}\right)^{1/2}$.

$$H_{c2} = \sqrt{2}\,\kappa H_c$$

At onset of vortex state, i.e. $H \gtrsim H_{c1}$, the cross-section area of a vortex is in the order of $\pi\lambda^2$ because the magnetic field decays exponentially to zero over a distance in the order of penetration depth λ*[55]*.

$$H_{c1} \approx H \approx \Phi_0/\left(\pi\lambda^2\right)$$

Similar express for H_{c2} can be obtained in terms of the coherence length ξ *[55]*.

$$H_{c2} = \frac{2\alpha m'C}{e'\hbar} = \left(\frac{2\pi\hbar C}{e'}\right)\left(2\pi\frac{\hbar^2}{2m'\alpha}\right)^{-1} = \Phi_0/\left(2\pi\xi^2\right)$$

Actual expression for H_{c1} can be derived by considering the crossover point $\kappa = 1/\sqrt{2}$ between type I and type II superconductor, at which H_c, H_{c1} and H_{c2} should be equal.

$$H_{c2} = \frac{\Phi_0}{2\pi\xi^2} = \frac{\Phi_0}{2\pi\left(\xi^2/\lambda^2\right)\lambda^2} = \frac{\Phi_0}{2\pi\kappa^2\lambda^2} = \frac{\Phi_0}{4\pi\lambda^2} = H_{c1}$$

$$H_{c1} = \Phi_0/\left(4\pi\lambda^2\right)$$

Relation between H_{c1} and H_{c2} with the thermodynamic critical field H_c can be obtained.

$$\boxed{H_{c2} = \Phi_0/\left(2\pi\xi^2\right) = \sqrt{2}\,\kappa H_c}$$

$$\boxed{H_{c1} = \Phi_0/\left(4\pi\lambda^2\right) = \frac{\Phi_0}{2\times 2\pi\xi^2\kappa^2} = \frac{H_{c2}}{2\kappa^2} = \frac{H_c}{\left(\sqrt{2}\,\kappa\right)}}$$

$H_{c1}\cdot H_{c2} = H_c^2$ and $H_{c1}/H_{c2} = 1/\left(2\kappa^2\right)$

For many type II superconductors, $H_{c2} >> H_c$ or $\kappa >> 1/\sqrt{2}$, so H_{c1} is very small.

REFERENCES

REFERENCES

1. R. Beyers et al., "Crystallography and Microstructure of Tl-Ca-Ba-Cu-O Superconducting Oxides," Appl. Phys. Lett., **53 (5)** (1988) 432-434.

2. W. Y. Lee et al., "Low-temperature Formation of Epitaxial $Tl_2Ca_2Ba_2Cu_3O_{10}$ Thin Films in Reduced O_2 Pressure," Appl. Phys. Lett., **60 (6)** (1992) 774-774.

3. R. K. Singh and J. Narayan, "The Pulsed-Laser Deposition of Superconducting Thin Films," JOM, **no. 3** (1991) 13-20.

4. D. Dijkkamp and T. Venkatesan, "Preparation of Y-Ba-Cu Oxide Superconductor Thin Films Using Pulsed Laser Evaporation from High T_c Bulk Materials," Appl. Phys. Lett. **51 (8)** (1987) 619-621.

5. X. D. Wu et al, "Epitaxial Ordering of Oxide Superconductor Thin Films on (100)$SrTiO_3$ Prepared by Pulsed Laser Evaporation," Appl. Phys. Lett. **51 (11)** (1987) 861-863.

6. X. D. Wu, A. Inam, T. Venkatesan et al., "Low-temperature Preparation of High T_C Superconducting Thin Films," Appl. Phys. Lett. **52 (9)** (1988) 754-756.

7. S. Miura and T. Yoshitake, "Structure and Superconducting Properties of $Y_1Ba_2Cu_3O_{7-d}$ Films Prepared by Transversely Excited Atmospheric Pressure CO_2 Pulsed Laser Evaporation," Appl. Phys. Lett. **52 (12)** (1988) 1008-1010.

8. H. S. Kwok, P. Mattocks, L. Shi, X. W. Wang, S. Witanachchi, Q. Y. Ying, J. P. Zheng, and D. T. Shaw, "Laser Evaporation Deposition of Superconducting and Dielectric Thin Films," Appl. Phys. Lett. **52 (21)** (1988) 1825-1827.

9. Osamu Eryu, Kouichi Murakami, Koki Takita, Kohzoh Masuda, Hiromoto Uwe, Hiroshi Kudo, and Tsunetaro Sakudo, " Y-Ba-Cu Oxide Films Formed with Pulsed-Laser Induced Fragments," Jpn. J. Appl. Phys. **27 (4)** (1988) L628-L631.

10. S. Witanachchi, H. S. Kwok, X. W. Wang, and D. T. Shaw, "Deposition of Superconducting Y-Ba-Cu-O Films at 400 °C without Post-annealing" Appl. Phys. Lett. **53 (3)** (1988) 234-236.

11. C. C. Chang, X. D. Wu, A. Inam, D. M. Hwang, T. Venkatesan, P. Barboux, and J. M. Tarascon, "Smooth High T_C $Y_1Ba_2Cu_3O_X$ Films by Laser Deposition at 650 °C," Appl. Phys. Lett. **53 (6)** (1988) 517-519.

12. B. Roas, L. Schultz, and G. Endres, "Epitaxial Growth of $YBa_2Cu_3O_{7-X}$ Thin Films by a Laser Evaporation Process," Appl. Phys. Lett. **53 (16)** (1988) 1557-1559.

13. G. Koren, A. Gupta, and R. J. Baseman, "Role of Atomic Oxygen in Low-temperature Growth of $YBa_2Cu_3O_{x-d}$ Thin Films by Laser Ablation Deposition," Appl. Phys. Lett. **54 (19)** (1989) 1920-1922.

14. R. K. Singh, J. Narayan, A. K. Singh, and J. Krishnaswamy, "In situ Processing of Epitaxial Y-Ba-Cu-O High T_C Superconducting Films on (100)$SrTiO_3$ and (100)YS-ZrO_2 Substrates at 500-650 °C," Appl. Phys. Lett. **54 (22)** (1989) 2271-2273.

15. M. Balooch, D. R. Olander, and R. E. Russo, "Y-Ba-Cu-O Superconducting Films Produced by Long-pulsed Laser Vaporization," Appl. Phys. Lett. **55 (2)** (1989) 197-199.

16. G. Koren, A. Gupta, R. J. Baseman, M. I. Lutwyche, and R. B. Laibowitz, "Laser Wavelength Dependent Properties of $YBa_2Cu_3O_{x-d}$ Thin Films Deposited by Laser Ablation," Appl. Phys. Lett. **55 (23)** (1989) 2450-2452.

17. B. H. Moeckly, S. E. Russek, D. K. Lathrop, R. A. Buhrman, Jian Li, and J. W. Mayer, "Growth of $YBa_2Cu_3O_7$ Thin Films on MgO: The Effect of Substrate Preparation," Appl. Phys. Lett. **57 (16)** (1990) 1687-1689.

18. J. P. Zheng, S. Y. Dong, and H. S. Kwok, "Texturing of Epitaxial in situ Y-Ba-Cu-O Thin Films on Crystalline Substrates," Appl. Phys. Lett. **58 (5)** (1991) 540-542.

19. R. K. Singh and D. Bhattacharya, "Improvement in the Properties of High T_c Films Fabricated in situ by Laser Ablation of $YBa_2Cu_3O_7$-Ag Targets," Appl. Phys. Lett. **60 (2)** (1992) 255-257.

20. Y. Iijima, N. Tanabe, O. Kohno, and Y. Ikeno, "In-plane Aligned $YBa_2Cu_3O_{7-x}$ Thin Films Deposited On Polycrystalline Metallic Substrates," Appl. Phys. Lett. **60 (6)** (1992) 769-771.

21. D. K. Fork and K. Nashimoto, "Epitaxial $YBa_2Cu_3O_{7-d}$ on GaAs(001) Using Buffer Layers," Appl. Phys. Lett. **60 (13)** (1992) 1621-1623.

22. J. A. Alarco,G. Brorsson, Z. G. Ivanov, P.-A, Nilsson, and E. Olsson, "Effect of Substrate Temperature on The Microstructure of $YBa_2Cu_3O_{7-d}$ Films Grown on (001)Y-ZrO_2 Substrates," Appl. Phys. Lett. **61 (6)** (1992) 723-725.

23. S. Komuro, Y. Aoyagi, T. Morikawa and S. Namba, "Preparation of High-T_C Superconducting Films by Q-switched YAG Laser Sputtering," Jpn. J. Appl. Phys. **27 (1)** (1988) L34-L36.

24. Arun Inam and X. D. Wu, "Pulsed Laser Etching of High T_C Superconducting Films," Appl. Phys. Lett. **51 (14)** (1987) 1112-1114.

25. J. Mannhart, M. Scheuermann, C. C. Tsuei, M. M. Oprysko, C. C. Chi, C. P. Umbach, R. H. Koch and C. Miller, "Micropatterning of High T_C Films with an Excimer Laser," Appl. Phys. Lett. **52 (15)** (1988) 1271-1273.

26. R. G. Humphreys, J. S. Satchell, N. G. Chew, and J. A. Edwards, "Narrow Tracks in $YBa_2Cu_3O_7$ Thin Films Defined by Laser Ablation," Appl. Phys. Lett. **54 (1)** (1989) 75-77.

27. Arunava Gupta and Gad Koren, "Direct Laser Writing of Superconducting Patterns of $Y_1Ba_2Cu_3O_{7-d}$," Appl. Phys. Lett. **52 (8)** (1988) 665-666.

28. B. W. Hussey and A. Gupta, "Laser-assisted Etch of $YBa_2Cu_3O_{7-d}$," Appl. Phys. Lett. **54 (13)** (1989) 1272-1274.

29. G. E. Jang, K. Mukherjee, P. A. A. Khan and M. Tayal, "Manufacturing of High Temperature Superconductor by Using A Nd:Yag Laser," Laser Materials Processing III (Warrendale, PA: The Minerals, Metals & Materials Society, 1988), 159-169.

30. C. W. Chen, P. A. A. Khan and K. Mukherjee, "Laser Fabrication of Pb Doped Bi-Sr-Ca-Cu-O Superconductor," J. Mat'ls Sci. **27** (1992) 3221-3224.

31. M. Levinson, S. S. P. Shah, and D. Y. Wang, "Laser Zone-melted Bi-Sr-Ca-Cu-O Thick Films," Appl. Phys. Lett. **55 (16)** (1989) 1683-1685.

32. Naoaki Aizaki, Koichi Terashima, Jun-ichi Fujita and Sinji Matsui, "$YBa_2Cu_3O_Y$ Superconducting Thin Film Obtained by Laser Annealing," Jpn. J. Appl. Phys. **27 (2)** (1988) L231-233.

33. P. Haldar, J. G. Hoehn, Jr., and J. A. Rice, "Enhancement in Critical Current Density of Bi-Pb-Sr-Ca-Cu-O Tapes by Thermomechanical Processing: Cold Rolling versus Uniaxial Pressing," Appl. Phys. Lett., **60 (4)** (1992) 495-497.

34. S. Jin, G. W. Kammlott, T. H. Tiefel and S. K. Chen, "Formation of Layered Microstructure in the Y-Ba-Cu-O and Bi-Sr-Ca-Cu-O Superconductors," Physica C **198** (1992) 333-340.

35. J. M. Tarascon, W. R. McKinnon, P. Barboux, D. M. Hwang, B. G. Bagley, L. H. Greene, G. Hull, Y. LePage, N. Stoffel, and M. Giroud, "Preparation, Structure, and Properties of the Superconducting Compound Series $Bi_2Sr_2Ca_{n-1}Cu_nO_y$ with n = 1, 2, and 3," Phys. Rev. **38 (13)** (1988) 8885-8892.

36. H. Maeda, Y. Tanaka, M. Fukutomi, and T. Asano, "A New High-T_C Oxide Superconductor without a Rare Earth Element," J. Appl. Phys. **27 (2)** (1988) L209-L210.

37. D. Shi, M. S. Boley, J. G. Chen, M. Xu, K. Vandervoort, Y. X. Liao, A. Zangvil, J. Akujieze, and C. Segre, "Origin of Enhanced Growth of the 110 K Superconducting Phase by Pb Doping in the Bi-Sr-Ca-Cu-O System," Appl. Phys. Lett. **55 (7)** (1989) 699-701.

38. Y. Yamada and S. Murase, "Pb Introduction to the High-T_C Superconductor Bi-Sr-Ca-Cu-O," Jpn. J. Appl. Phys. **27 (6)** (1988) L996-L998.

39. M. Takano, J. Takada, K. Oda, H. Kitaguchi, Y. Miura, Y.Ikeda, Y. Tomii, and H. mazaki, "High-T_c Phase Promoted and Stabilized in the Bi, Pb-Sr-Ca-Cu-O System," Jpn. J. Appl. Phys. **27 (6)** (1988) L1041-L1043.

40. M. Mizuno, H. Endo, J. Tsuchiya, N. Kijima, A. Sumiyama, and Y. Oguri, "Superconductivity of $Bi_2Sr_2Ca_2Cu_3Pb_XO_Y$ (x=0.2, 0.4, 0.6)," Jpn. J. Appl. Phys. **27 (7)** (1988) L1225-L1227.

41. S. A. Sunshine, T. Siegrist, L. F. Schneemeyer, D. W. Murphy, R. J. Cava, B. Batlogg, R. B. van Dover, R. M. Fleming, S. H. Glarum, S. Nakahara, R. Farrow, J. J. Krajewski, S. M. Zahurak, J. V. Waszczak, J. H. Marshall, P. March, L. W. Rupp, Jr. ,and W. F. Feck, "Structure and Physical properties of Single Crystals of the 84-K Superconductor $Bi_{2.2}Sr_2Ca_{0.8}Cu_2O_{8+d}$" Phys Rev. B38 (1988) 893.

42. T. Venkatesan, X. D. Wu, A. Inam, and J. B. Wachtman, "Observation of Two Distinct Components During Pulsed Laser Deposition of High T_C Superconducting Films," Appl. Phys. Lett. 52 (14) (1988) 1193-1195.

43. P. E. Dyer, R. D. Greenough, A. Issa, and P. H. Key, "Spectroscopic and Ion Probe Measurements of KrF Laser Ablated Y-Ba-Cu-O Bulk Samples," Appl. Phys. Lett. 53 (6) (1988) 534-536.

44. T. Venkatesan et al., "Nature of The Pulsed Laser Process for The Deposition of High T_C Superconducting Thin Films," Appl. Phys. Lett. 53 (15) (1988) 1431-1433.

45. J. P. Zheng, Z. Q. Huang, D. T. Shaw, and S. Kwok, "Generation of High-energy Atomic Beam in Laser-Superconducting Target Interactions," Appl. Phys. Lett. 54 (3) (1989) 280-282.

46. J. P. Zheng, Q. Y. Ying, S. Witanachchi, Z. Q. Huang, D. T. Shaw, and S. Kwok, "Role of The Oxygen Atomic Beam in Low-temperature Growth of Superconducting Films by Laser Deposition," Appl. Phys. Lett. 54 (10) (1989) 954-956.

47. C. W. Chen and K. Mukherjee, "Review of Progress in Pulsed Laser Deposition and Using Nd:YAG Laser in Processing of High T_C Superconductors," Proceeding of Beam Processing of Advanced Materials International Conference (Warrendale, PA: The Minerals, Metals & Materials Society, 1992) 301-321.

48. Shin-ya Aoki, Taichi Yamaguchi, Yasuhiro Iijima, Akira Kagawa, Osamu Kohno, Shigeo Nagaya and Toshio Inoue, "High J_C Y-Ba-Cu-O Thin Film on Metal Substrates Prepared by Chemical Vapor Deposition," Jpn. J. Appl. Phys. 31 part 2 (5A) (1992) L547-L549.

49. Naotaka Minami, Nobuyuki Koura and Hiromasa Shoji, "Preparation of $YBa_2Cu_3O_{7-d}$ Superconductor Coating on Austenitic Steel by Electrophoretic Deposition Method - Study on Buffering Layers," Jpn. J. Appl. Phys. 31 part 2 (6B) (1992) 1784-L786.

50. P. N. Peters, R. C. Sisk and E. W. Urban, "Observation of Enhanced Properties in Samples of Silver Oxide Doped $YBa_2Cu_3O_X$," Appl. Phys. Lett. 52 (1990) 2066-2067.

51. D. Lee and K. Salama, "Enhancements in Current Density and Mechanical Properties of Y-Ba-Cu-O / Ag Composites," Jpn. J. Appl. Phys. 29 (1990) L2017-L2019.

52. G. Kozlowski, I. Maartense, R. spyker, R. leese and C. E. Oberly, "Critical Current Density Enhancement in $YBa_2Cu_3O_{7-X}$-silver Composit Superconductor," Physica C 173 (1991) 195-200.

53. Sungho Jin, "Processing Techniques for Bulk High-T_C Superconductors," JOM March (1991) 7-12.

54. C. J. Gorter, "Some Remarks on Superconductivity of the Second Kind," Rev. Mod. Phys. **36 (1)** (1964) 27-31.

55. Charles Kittle, Introduction to Solid State Physics, 6th edition, (SINGAPORE: John Wiley & Sons, Inc., 1986) 133, 319-354, 631-636.

56. Gerald Burns, High-Temperature Superconductivity, An Introduction, (San Diego, CA: Academic Press, Inc., 1992) 8-53.

57. J. Bardee, L. N. Cooper, and J. R. Schrieffer, "Microscopic Theory of Superconductivity," Phys. Rev., **106** (1957) 162-163; "Theory of Superconductivity," **108** (1957) 1175-1204.

58. J. R. Schrieffer, "The Pairing Theory - Its Physical Basis and Its Consequences", Physics of High-Temperature Superconductors, edited by S. Maekawa and M. Sato, (Berlin Heidelberg, Germany: Spring-Verlag, 1992) 3-17.

59. W. G. V. Rosser, An Introduction to Statistical Physics, (Chichester, England: Ellis Horwood Limited, 1982) 274-278.

60. J. G. Bednorz and K. A. Muller, "Possible High T_C Superconductivity in the Ba-La-Cu-O System," Z Phys. **B64** (1986) 189-193.

61. A. W. Sleight, J. L. Gillson and P. E. Bierstedt, "High-Temperature Superconductivity in the $BaPb_{1-X}Bi_XO_3$ System," Sol. State Comm. **17** (1975) 27-28.

62. L. F. Mattheiss, E. M. Gyorgy and D. W. Johson, Jr., "Superconductivity above 20 K in the Ba-K-Bi-O System," Phys. Rev. **B37** (1988) 3745-3746.

63. R. J. Cava, B. Batlogg, J. J. Krajewski, R. Farrow, L. W. Rupp Jr. , A. E. White, K. Short, W. F. Peck and T. Kometani, "Superconductivity near 30 K without Copper: the $Ba_{0.6}K_{0.4}BiO_3$ Perovskite," Nature **332** (1988) 814-816.

64. R. Beyers, G. Lim, E. M. Engler, R. J. Savoy, T. M. Shaw, T. R. Dinger, W. J. Gallagher and R. L. Sandstrom, "Crystallography and Microstructure of $Y_1Ba_2Cu_3O_{9-X}$, a perovskite-based Superconducting Oxide," Appl. Phys. Lett. **50 (26)** (1987) 1918-1920.

65. Xiaoping Jiang, Huafeng Yu, Ze Zhang, Naiping Zhu, Hongbo Qi, Guoyue Shu, Yunchuan Tian, Dexing Pang, Xiaobiao Zeng and Zhongjin Yang, "Effect of Crystal Structure on Superconductivity of Y-Ba-Cu-O System Compounds," Appl. Phys. Lett. **51 (8)** (1987) 625-627.

66. Xiaobiao Zeng, Xiaoping Jiang, Hongbo Qi, Dexing Pang, Naiping Zhu and Ze Zhang, "Relationship between Superconductivity and Lattice Distortion in Y-Ba-Cu-O Compounds," Appl. Phys. Lett. **51 (9)** (1987) 692-693.

67. Shigemitsu Nakanishi, Mineo Kogachi, Hiroyuki Sasakura, Nobuo Fukuoka, Shinnosuke Minamigawa, Kiyotaka Nakahigashi and Akira Yanase, "The Orthorhombic to Tetragonal Transition Under Controlled Oxygen Content in High-T_C Superconductor $YBa_2Cu_3O_Y$," Jpn. J. Appl. Phys. **27 (3)** (1988) L329-332.

68. W. Lo, Tong B. Tang and Chaorui Li, "Thermodynamic Studies of the Orthorhombic-tetragonal Transition in $Ba_2YCu_3O_{7-d}$," Appl. Phys. Lett. **53 (26)** (1988) 2710-2712.

69. J. C. Phillips, "Physics of High-T_C Superconductors", (San Diego, CA: Academic Press, Inc, 1989) 85-86.

70. S. Lapinskas, A. Resengren and E. E. Tornau, "Oxygen Ordering and Superconducting Temperature of $YBa_2Cu_3O_{6+X}$", Physica C **199** (1992) 91-94.

71. D. W. Face et al., "Preparation of Superconducting Thin Films of Bismuth Calcium Copper Oxides by Reactive Sputtering," Appl. Phys. Lett. **53 (3)** (1988) 246-248.

72. R. L. Sandstrom, W. J. Gallagher, T. R. Dinger, R. H. Koch, R. B. Laibowitz, A. W. Kleinsasser, R. J. Gambino, B. Bumble, and M. F. Chishoim, "Reliable Single-target Sputtering Process for High-temperature Superconducting Films and Devices," Appl. Phys. Lett. **53 (5)** (1988) 444-446.

73. A. Hohlder, D. Guggi, H. Neeb, and C. Heiden, "Fully Textured Growth of $Y_1Ba_2Cu_3O_{7-d}$ Films by Sputtering on $LiNbO_3$ Substrates," Appl. Phys. Lett. **54 (11)** (1989) 1066-1067.

74. Ian D. Raistrick, M. Hawley, J. G. Beery, F. H. Garzon, and R. J. Houlton, "Microstructure and Growth Mechanism of Thin Sputtered Films of $YBa_2Cu_3O_7$ on MgO Substrates," Appl. Phys. Lett. **59 (24)** (1991) 3177-3179.

75. B. Oh et al., "Critical Current Densities and Transport in Superconducting $YBa_2Cu_3O_{7-d}$ Films Made by Electron Beam Coevaporation," Appl. Phys. Lett. **51 (11)** (1987) 852-854.

76. X. K. Wang, K. C. Sheng, S. J. Lee, Y. H. Shen, S. N. Song, D. X. Li, R. P. H. Chang, and J. B. Ketterson, "Oriented Thin Films of YBaCu(F)O with high T_C and J_C Prepared by Electron Beam Multilayer Evaporation," Appl. Phys. Lett. **54 (16)** (1989) 1573-1575.

77. N. G. Chew, S. W. Goodyear, J. A. Edwards, J. S. Satchell, S. E. Blenkinsop, and R. G. Humphreys, "Effect of Small Changes in Composition on the Electrical and Structural Properties of $YBa_2Cu_3O_7$ Thin Films," Appl. Phys. Lett. 57 (19) (1990) 2016-2018.

78. P. Berberich, J. Tate, W. Dietsche and H. Kinder, "Low-temperature Preparation of Superconducting $YBa_2Cu_3O_{7-d}$ Films on Si, MgO, and $SrTiO_3$ by Thermal Coevaporation," Appl. Phys. Lett. **53 (10)** (1988) 925-926.

79. M. Ece and R. W. Vook, "Y-Ba-Cu-O Thin Films Prepared by Flash Evaporation," Appl. Phys. Lett. **54 (26)** (1989) 2722-2724.

80. Yukio Yasuda, Yasuo Koide, Shigeaki Zaima, and Naoki Sano, "Y-Ba-Cu-O Superconducting Thin Films Prepared by Plasma-assisted Flash Evaporation," Appl. Phys. Lett. **55 (3)** (1989) 307-309.

81. A. D. Berry, D. K. Gaskill, R. T. Holm, E. J. Cukauskas, R. Kaplan, and R. L. Henry, "Formation of High T_C Superconducting Films by Organometallic Chemical Vapor Deposition," Appl. Phys. Lett. **52 (20)** (1988) 1743-1745.

82. Rointan F. Bunshah, ed., Deposition Technologies for Films and Coatings: Developments and Applications (Park Ridge, NJ: Noyes Publications, 1982), 3-9.

83. O. Auciello, A. R. Krauss, J. Santiago-Aviles, A. F. Schreiner, and D. M. Gruen, "Surface Compositional and Topographical Changes resulting from Excimer Laser Impacting on $YBa_2Cu_3O_7$ Single Phase Superconductors," Appl. Phys. Lett. **52 (3)** (1988) 239-241.

84. Osamu Eryu, k. Murakami, K. Masuda, K. Shihoyama, and T. Mochizuki, "Strong Wavelength Dependence of Laser Ablation Fragments of Superconductor $YBa_2Cu_3O_y$," Jpn. J. Appl. Phys. **31 (2A)** (1992) L86-L88.

85. M. Gurvitch and A. T. Fiory, "Preparation and Substrate Reaction of Superconducting Y-Ba-Cu-O Films," Appl. Phys. Lett. **51 (13)** (1987) 1027-1029.

86. M. Aslam, R. E. Soltis, E. M. Logothetis, R. Ager, M. Mikkor, W. Win, J. T. Chen and L. E. Wenger, "Rapid Thermal Annealing Of YBaCuO Films on Si and SiO_2 Substrates," Appl. Phys. Lett. **53 (2)** (1988) 153-155.

87. M. J. Cima, J. S. Schneider, and S. C. Peterson, "Reaction of $Ba_2YCu_3O_{6.9}$ Films with Yttria-stabilized Zirconia Substrates," Appl. Phys. Lett. **53 (8)** (1988) 710-712.

88. S. I. Shah, "Annealing Studies of $YBa_2Cu_3O_{7-x}$ Thin Films," Appl. Phys. Lett. **53 (7)** (1988) 612-614.

89. A. Zherikhin, V. Bagratashvili, V. Burimov, E. Sobol, G. Shubnii and A. Sviridov, "The Action of Powerful Laser Radiation on 1-2-3 Superconducting Thin Films and Bulk Materials," Physica C **198** (1992) 341-348.

90. Shigeru Otsubo, T. Minamikawa, Y. Yonezawa, A. Morimoto, and T. Shimizu, "Thermal Analysis of Target Surface in the Ba-Y-Cu-O Film Preparation by Laser Ablation Method," Jpn. J. Appl. Phys. **29 (1)** (1990) L73-L76.

91. Rajiv K. Singh, D. Bhattacharya, and J. Narayan, "Control of Surface Particle Density in Pulsed Laser Deposition of Superconducting $YBa_2Cu_3O_7$ and Diamondlike Carbon Thin Films," Appl. Phys. Lett. **61 (4)** (1992) 483-485.

92. W. Eidelloth, R. L. Sandstrom and M. M. Plechaty, "Polishing of Highly Oriented $YBa_2Cu_3O_{7-d}$ Thin Films," Physica C **197** (1992) 389-393.

93. M. Young, Optics and Lasers, 3rd edition, (Berlin, Germany: Springer-Verlag, 1986) 145-171.

94. Allan Lytel and Lawrence Buckmaster, abc's of Lasers and Masers, (New York, NY: Howard W. Sams & Co., Inc.; The Bobbs-Merrill Co., Inc., 1972) 7-20.

95. Jeff Hecht, "Neodymium Lasers Prove Versatile Over Three Decades," Laser Focus World, **28 (4)** (1992) 77-94.

96. Daniel W. Trainor, "Military Excimer-Laser Technology Seeks Real-World Uses," Laser Focus World, **29 (6)** (1993) 143-149.

97. Jeff Hecht, "Excimer Laser Produce Powerful Ultraviolet Pulses," Laser Focus World, **28 (6)** (1992) 63-72.

98. Marc Stehle, "Will Kilowatt Excimer Lasers Become Future Industrial Tools," Laser Focus World, **29 (6)** (1993) 135-139.

99. M. F. Yan, R. L. Barns, H. M. O'Bryan, Jr., P. K. Gallagher, R. C. Sherwood, and S. Jin, "Water Interaction with the Superconducting $YBa_2Cu_3O_7$ Phase," Appl. Phys. Lett. **51 (7)** (1987) 532-534.

100. R. L. Barns and R. A. Laudise, "Stability of Superconducting $YBa_2Cu_3O_7$ in the Presence of Water," Appl. Phys. Lett. **51 (17)** (1987) 1373-1375.

101. Takuya Hashimoto, Kazuo Fueki, Akira Kishi, Tadahiko Azumi and Hideomi Koinuma, "Thermal Expansion Coefficients of High-T_C Superconductors," Jpn. J. Appl. Phys. **27 (2)** (1988) L214-L216.

102. T. Uzumaki, K. Yamanaka, N. Kamehara, and K. Niwa, "The Effect of Ca_2PbO_4 Addition on Superconductivity in a Bi-Sr- Cu-O System," Jpn. J. Appl. Phys. **28 (1)** (1989) L75-L77.

103. H. Endo, J. Tsuchiya, N. Kijima, A. Sumiyama, M. Mizuno, and Y. Oguri, "Thermal Stability of the High-T_c Superconductor in the Bi-Sr-Ca-Cu-O System," Jpn. J. Appl. Phys. **27 (10)** (1988) L1906-L1909.

104. N. Kijima, H. Endo, J. Tsuchiya, A. Sumiyama, M. Mizuno, and Y. Oguri, "Reaction Mechanism of Forming the High-T_c Superconductor in the Pb-Bi-Sr-Ca-Cu-O System," Jpn. J. Appl. Phys. **27 (10)** (1988) L1852-L1855.

105. A. Sumiyama, H. Endo, J. Tsuchiya, N. Kijima, M. Mizuno, and Y. Oguri, "A. C. Susceptibility of the Superconducting Bi-(Pb)-Sr-Ca-Cu-O System," Jpn. J. Appl. Phys. **28 (3)** (1989) L373-L376.

106. Powder Diffraction File (Philadelphia, PA: American Society for Testing and Materials, 1988).

107. William Band, Introduction to Mathematical Physics, (Princeton, NJ: D. Van Nostrand Co., Inc.) 294-295.